

ISSN 1607-8829

Journal of

THERMOELECTRICITY

International Journal

- General problems
- Theory
- Materials research
- Technology
- Design
- Metrology and standardization
- Reliability
- Thermoelectric products
- News
- Discussion

2013

3

Institute of Thermoelectricity, Academy of Sciences and Ministry of Education and Science of Ukraine

Journal of THERMOELECTRICITY

International Research

Founded in December, 1993

published 6 times a year

No. 3

2013

Editorial Board

Editor-in-Chief LUKYAN I. ANATYCHUK

Petro I. Baransky

Bogdan I. Stadnyk

Lyudmyla N. Vikhor

Vilius Ya. Mikhailovsky

Ivan V. Gutsul

Elena I. Rogacheva

Stepan V. Melnychuk

Andrey A. Snarskii

International Editorial Board

Lukyan I. Anatychuk, *Ukraine*

A.I. Casian, *Moldova*

Steponas P. Ašmontas, *Lithuania*

Takenobu Kajikawa, *Japan*

Jean-Claude Tedenac, *France*

T. Tritt, *USA*

H.J. Goldsmid, *Australia*

Sergiy O. Filin, *Poland*

L.P. Bulat, *Russia*

M.I. Fiodorov, *Russia*

L. Chen, *China*

D. Sharp, *USA*

T. Caillat, *USA*

Yuri Gurevich, *Mexico*

Yuri Grin, *Germany*

Founders - National Academy of Sciences, Ukraine
Institute of Thermoelectricity of National Academy of Sciences and Ministry
of Education and Science of Ukraine

Certificate of state registration № KB 15496-4068 ПР

Editorial office manager D. Taschuk

Editors:

L. Vikhor, L. Kosyachenko, A. Farion, V. Kramar, V. Katerynchuk

Published by decision of Scientific Board of Institute of Thermoelectricity
of National Academy of Sciences and Ministry of Education and Science of Ukraine

Address of editorial office:

Ukraine, 58002, Chernivtsi, General Post Office, P.O. Box 86.

Phone: +(380-3722) 7 58 60.

Fax: +(380-3722) 4 19 17.

E-mail: jt@inst.cv.ua

[http:// www.jt.cv.ua](http://www.jt.cv.ua)

Signed for publication 25.06.13. Format 70×108/16. Offset paper №1. Offset printing.
Printer's sheet 11.1. Publisher's signature 9.2. Circulation 400 copies. Order 6.

Printed by "Bukrek" publishers,
10, Radischev Street, 58000, Chernivtsi, Ukraine.

Copyright © Institute of Thermoelectricity, Academy of Sciences
and Ministry of Education and Science, Ukraine, 2013

CONTENTS

Theory

- P.V. Gorsky, V.P. Mikhachenko* Effect of thermoelectric material anisotropy
on the electric conductivity and lattice thermal conductivity
of its contacting particles 5

Material Research

- A.I. Casian, I.I. Sanduleac* Organic thermoelectric materials: new opportunities * 11
E.M. Godzhayev, S.Sh. Kakhramanov, K.J. Gulmamedov, A.Yu. Gamzayeva
Surface nanoparticles in $A^{V_2}B^{VI_3}$ 21
N.V. Morozova, I.V. Korobeynikov, K.V. Kurochka, V.V. Shchennikov
High-pressure investigations of materials suffering abrupt jumps
of the Seebeck effect * 30
*I.A. Drabkin, V.B. Osvenski, Yu.N. Parkhomenko, A.I. Sorokin,
G.I. Pivovarov, L.P. Bulat* Anisotropy of thermoelectric properties
of *p*-type nanostructured material based on $(Bi, Sb)_2Te_3$ * 35
I.V. Matsukevich, A.I. Klyndyuk Synthesis and thermoelectric properties
of $Ca_3Co_{3.85}M_{0.15}O_{9+\delta}$ ($M = V - Zn$) solid solutions prepared
by citrate gel method 47

Design

- M.A. Korzhuev, T.E. Svechnikova* Thermodynamic restrictions for the net power
of automotive thermoelectric generators and prospects of their use in transport * 54
*V.R. Bilinsky-Slotylo, L.N. Vikhor, V.Ya. Mykhailovsky, R.N. Mochernyuk,
A.F. Semizorov* Efficiency improvement of generator modules based
on *CoSb* through use of segmented and multi-stage structures 71

Reliability

- A.A. Nazarenko* Reliability enhancement of thermoelectric coolers
using polymer vacuum coatings * 77
A.V. Simkin, A.V. Biryukov, N.I. Repnikov., O.N. Ivanov Reliability test
of generator thermopiles made with the use of arc plasma spraying method * 86

News

- XV International forum on thermoelectricity 95

* – publication of the lectures presented at the XV International Forum on Thermoelectricity
in Tallinn, May 20 – 24, 2013.

P.V. Gorsky, V.P. Mikhachenko



P.V. Gorsky

Institute of Thermoelectricity
NAS and MES of Ukraine, 1, Nauky Str.,
Chernivtsi, 58029, Ukraine



V.P. Mikhachenko

**EFFECT OF THERMOELECTRIC
MATERIAL ANISOTROPY ON THE
ELECTRIC CONDUCTIVITY AND
LATTICE THERMAL CONDUCTIVITY
OF ITS CONTACTING PARTICLES**

In the framework of a six-ellipsoid Drabble-Wolfe model in the approximation of anisotropic relaxation time depending solely on full energy of current carriers, the electric conductivity was calculated for a physical model – two half-spheres contacting in a circle with regard to electron scattering on the contact boundaries as applied to Bi_2Te_3 . It is shown that the value of effective electric conductivity of this material in the temperature range of 300 K and higher can be maintained if contact radius exceeds 10.4 of mean free path of electron (hole), i.e. is at least 0.4 μm . This result coincides with that obtained in the isotropic approximation. The reason for this coincidence is a dependence of relaxation time tensor components on full energy of current carriers. The same result is obtained for the radius of contact on which boundaries due to phonon scattering the lattice thermal conductivity of Bi_2Te_3 is reduced by 30 – 40 % as compared to a single crystal. As long as such contacts can arise between particles of radius 40 – 80 μm , it accounts for retention and even some increase of thermoelectric figure of merit when passing from a single crystal to extruded material.

Key words: thermoelectric material, extrusion, figure of merit, electric conductivity, Drabble-Wolfe model, relaxation time, lattice thermal conductivity, contact, boundaries, phonons, scattering, normal processes, Umklapp processes.

Introduction

Bismuth telluride Bi_2Te_3 is a thermoelectric material most commonly used for the manufacture of working members of various thermoelectric instruments and devices [1]. It is characterized by well-expressed electric conductivity and thermal conductivity anisotropy. Taking into account that this crystal possesses $R3m$ group symmetry and cleavage planes along which it easily splits, its thermal conductivity and electric conductivity tensors have two independent components each. In particular, in the absence of a magnetic field, electric conductivity tensor has component σ_{11} in cleavage planes and component σ_{33} in a direction normal to them. The ratio σ_{11}/σ_{33} is 2.7 for p -type material and 4 ÷ 6 for n -type material. Bi_2Te_3 is intermediate in the electric conductivity value between high-resistance semiconductors traditionally used in radio electronics and computer technique, such as germanium and silicon, and semimetals, such as bismuth. The band spectrum of this crystal is anisotropic and described by a six-ellipsoid Drabble-Wolfe model [1].

Due to conductivity anisotropy, thermoelectric modules of solid single crystals Bi_2Te_3 are made so that temperature gradient and electric current are parallel to cleavage planes, where conductivity

value is higher than in the direction perpendicular to them. Alongside with single crystals, extruded materials that may consist of particles with oriented or random cleavage planes are used for the manufacture of thermoelectric modules. With a random arrangement of cleavage planes, the electric conductivity of material in conformity with the Odelevsky formula will make $\sigma = \sqrt{\sigma_{11}\sigma_{33}}$, i.e. will be lower than the largest value. Further electric conductivity reduction can be due to current carrier scattering on the boundaries of small contacts between particles. These factors should have resulted in thermoelectric figure of merit reduction. However, in real practice this reduction is not observed. Hence, a mechanism must exist which assures electric conductivity retention and lattice thermal conductivity reduction at charge carrier and phonon scattering on the boundaries of contacts between the particles. Without a detailed account of electric conductivity anisotropy this mechanism was considered in [2, 3]. Our purpose in this paper is to analyze this mechanism with regard to real anisotropy of band spectrum of charge carrier and electric conductivity, as well as thermal conductivity of Bi_2Te_3 .

Consideration of the problem of electrons (holes) anisotropic scattering on contact boundaries in the approximation of power dependence of relaxation time on energy

Consider this problem within the framework of a model of two half-spheres of radius R ($r \ll R$) contacting in a circle of radius r . This model can approximate the shape-forming element of extruded thermoelectric material structure [4]. For this purpose, using the results given in [1], we first write general formulae for single crystal electric conductivity components σ_{11} and σ_{33} . To accomplish this, we predetermine relaxation time tensor components in the approximation of constant mean free paths in the directions of principal axes of ellipsoids by means of full energy of current carriers. These components are:

$$\tau_{1,2,3} = \frac{l_{1,2,3}\sqrt{m^*}}{\sqrt{2\varepsilon}}. \quad (1)$$

In this formula, l_1 , l_2 , l_3 are charge carrier mean free paths in respective directions, m^* is density-of-state effective mass, ε is full energy of charge carriers. Such an approach corresponds to “nearly isotropic scattering” whose anisotropy is taken into account by means of different lengths l_1 , l_2 , l_3 . Substitution of density-of-state effective mass into formula (1) unambiguously follows from the model assumption of relaxation time tensor components dependence on full energy of charge carriers.

With this relaxation time tensor, according to [1], components of electric conductivity tensor for nondegenerate charge carrier gas are equal to:

$$\sigma_{11} = \frac{4e^2 n_0 \sqrt{m_1 m_2 m_3}}{m_2 \sqrt{\pi m^*} (k_B T)^{1/2}} \left(l_2 + \frac{m_2}{m_1} l_1 \cos^2 \vartheta + \frac{m_2}{m_3} l_3 \sin^2 \vartheta \right). \quad (2)$$

$$\sigma_{33} = \frac{8e^2 n_0 \sqrt{m_1 m_2 m_3}}{m_2 \sqrt{\pi m^*} (k_B T)^{1/2}} \left(\frac{m_2}{m_1} l_1 \sin^2 \vartheta + \frac{m_2}{m_3} l_3 \cos^2 \vartheta \right). \quad (3)$$

In these formulae, m_1 , m_2 , m_3 are effective masses of charge carriers along the principal axes of ellipsoid, ϑ is the smallest rotation angle of ellipsoid up to coincidence of its long axis with crystal trigonal axis, k_B is the Boltzmann constant, T is absolute temperature, n_0 is charge carrier concentration, the rest of designations are generally accepted or explained above.

In the temperature region relevant for thermoelectric applications scattering mainly occurs on the deformation potential of acoustic phonons. In this region, $l_1, l_2, l_3 \propto T^{-1}$, so finally we get the known dependence $\sigma \propto T^{3/2}$, which in reality is somewhat distorted by the temperature dependence of respective effective masses.

Thus, formulae (2) and (3) fully determine electric conductivity tensor of Bi_2Te_3 single crystal in the absence of a magnetic field. Account in these formulae of scattering on contact boundaries presents no special problems. However, of crystal parameters in these formulae only all the effective masses and angle ϑ are known with certainty, for they are parameters of band structure which is reliably studied through measurement of de Haas-van-Alphen and de Haas-Shubnikov effects. As to mean free paths l_1, l_2, l_3 , they depend on acoustic phonon deformation potential tensor components. The band structure determines only the bulk component of this tensor [5], whereas in crystal with well-expressed cleavage planes the shear and bend components are also essential. So, it is worthwhile to write formulae (2) and (3) in such a form in which unknown parameters could be determined, for instance, from the data on electron and hole mobility.

Passing from the electric conductivity tensor to charge carrier mobility tensor, we write its components as follows:

$$b_{11,33} = \frac{eL_{11,33}\sqrt{2}}{\sqrt{\pi m^* k_B T}}. \quad (4)$$

In these formulae, in conformity with (2) and (3), charge carrier mean free paths determined by known mobility values are equal to:

$$L_{11} = \frac{4\sqrt{m_1 m_3}}{\sqrt{2m^* m_2}} \left(l_2 + \frac{m_2}{m_1} l_1 \cos^2 \vartheta + \frac{m_2}{m_3} l_3 \sin^2 \vartheta \right). \quad (5)$$

$$L_{33} = \frac{8\sqrt{m_1 m_3}}{\sqrt{2m^* m_2}} \left(\frac{m_2}{m_1} l_1 \sin^2 \vartheta + \frac{m_2}{m_3} l_3 \cos^2 \vartheta \right). \quad (6)$$

Let us now discuss charge carrier scattering on contact boundaries. Using the summation rule of inverse mean free paths, we find the ratio between mobilities \tilde{b}_{11} and \tilde{b}_{33} determined with regard to scattering on contact boundaries and mobilities determined by formula (4):

$$\tilde{b}_{11,33} / b_{11,33} = \frac{1}{\pi} \int_0^{2\pi} \int_0^1 \frac{k_{11,33} \sqrt{z^2 + 1 + 2z \cos \varphi}}{1 + k_{11,33} \sqrt{z^2 + 1 + 2z \cos \varphi}} z d\varphi dz. \quad (7)$$

In these formulae, $k_{11} = r/L_{11}$, $k_{33} = r/L_{33}$. Double integrals in them are due to averaging the expression for mobility over phonon mean free paths inside a circle where half-spheres are contacting. From formula (7) it follows that to maintain the mobilities in the form-shaping structural element at a level of 90 % of their values in a single crystal, coefficients k_{11} and k_{33} must be at least 10.4. At $T = 300$ K for electrons substituting to (6) $b_{11} = 1200 \text{ cm}^2/\text{C}\cdot\text{s}$, $b_{11}/b_{33} = 5$, $m^* = 0.45 m_0$ [1], we obtain $L_{11} = 38.7 \text{ nm}$, $L_{33} = 7.7 \text{ nm}$, whence $r = 400 \text{ nm}$. Similarly for holes, substituting $b_{11} = 510 \text{ cm}^2/\text{V}\cdot\text{s}$, $b_{11}/b_{33} = 2.7$, $m^* = 0.69 m_0$ we obtain $L_{11} = 20.4 \text{ nm}$, $L_{33} = 7.6 \text{ nm}$, whence $r = 212 \text{ nm}$. So, finally $r = 400 \text{ nm}$. Contacts of such dimensions can appear between particles of diameter $40 \div 80 \mu\text{m}$.

Let us next consider the possibility of lattice thermal conductivity reduction with phonon scattering on the boundaries of said contact between half-spheres. Comparison of thermal conductivity

and electric conductivity anisotropy figures for Bi_2Te_3 shows that for maintenance of thermoelectric figure of merit of extruded material at a level typical of a single crystal, the lattice thermal conductivity due to phonon scattering on the boundaries of said contact in conformity with the Odelevsky formula must be reduced by 30–40 % as compared to a single crystal. Consider this opportunity with regard to the following physical circumstances. First, in the region relevant for thermoelectric applications the final lattice thermal conductivity of thermoelectric material in question is largely caused by Umklapp processes at phonon-phonon scattering due to anharmonic component of lattice vibrations, on the one hand, and discrete periodic crystal structure, on the other hand. Second, normal processes, i.e. processes with retention of total pulse of phonon subsystem, making no direct contribution to final lattice thermal conductivity, modify all other scattering processes, including scattering on the boundaries, due to frequency redistribution of scattering probabilities [6, 7]. Thus, in the region relevant for thermoelectric applications, in conformity with the purpose of this paper, in the calculation of lattice thermal conductivity one should take into account three kinds of scattering processes: Umklapp processes, normal processes and scattering on contact boundaries.

Consider first lattice thermal conductivity of Bi_2Te_3 without regard to phonon scattering on contact boundaries. Following [6] and normalizing phonon relaxation time for the time of normal processes, components of lattice thermal conductivity tensor $\chi_{\parallel, \perp}$ of this material will be written as:

$$\chi_{\parallel, \perp} = \frac{3\hbar\rho v_{\parallel, \perp}^4}{32\gamma^2 k_B T_D^2 \theta^3 \pi} \int_0^1 \frac{x^4 \exp(x/\theta)}{\left[\exp(x/\theta) - 1\right]^2} \left(\frac{1}{Q_{\parallel, \perp}(x)} + \frac{2}{Q_{\perp, \perp}(x)} \right) dx. \quad (8)$$

In this formula, indexes \parallel and \perp refer to respective values in the direction parallel and perpendicular to layers (cleavage planes), ρ is crystal density, v is sound velocity in it, γ is the Gruneisen parameter, T_D is the Debye temperature, $\theta = T/T_D$, $Q_{\parallel, \perp}(x)$ and $Q_{\perp, \perp}(x)$ is frequency polynomials determined by mechanisms of scattering longitudinal and transverse phonons, respectively, and having in this case the form:

$$Q_{\parallel, \perp}(x) = x^4 + \mu_{\parallel, \perp} x, \quad (9)$$

$$Q_{\perp, \perp} = (\mu_{\parallel, \perp} + 3.125\theta^3)x. \quad (10)$$

As regards thermal conductivity dependence on material density, we note that formula (8) in this respect is true for a simple cubic lattice with one atom in a unit cell. The actual Bi_2Te_3 lattice is not of that kind, but we have to replace it by such, provided the real material density is maintained. Coefficient μ was approximately calculated for a simple cubic lattice by Leibfried and Shleemann [6], but, according to experimental data given in [6], even for materials with such a lattice it is not universal. So, we will “derive” coefficients μ_{\parallel} from the real values of Bi_2Te_3 thermal conductivity tensor components [1], with the requirement that the latter coincide with the theoretical values (10) with regard to (11) and (12). At $\chi_{\perp} = 0.58 \text{ W/m}\cdot\text{K}$, $\chi_{\parallel} = 1.45 \text{ W/m}\cdot\text{K}$, $\rho = 7859 \text{ kg/m}^3$, $\gamma = 1.5$, $v_{\parallel} = 2952 \text{ m/s}$, $v_{\perp} = 1867 \text{ m/s}$, $T_D = 155 \text{ K}$ and $T = 300 \text{ K}$ we obtain $\mu_{\parallel} = 0.022$, $\mu_{\perp} = 2.177 \cdot 10^{-3}$.

Let us now turn to calculation of material lattice thermal conductivity on condition of phonon scattering on contact boundaries. Using summation rule of inverse relaxation times, we obtain the following ratio between material thermal conductivity χ_i^{ef} at scattering on contact boundaries and single crystal thermal conductivity:

$$\frac{\chi_{l||,\perp}^{ef}}{\chi_{l||,\perp}} = \pi^{-1} \int_0^1 \int_0^{2\pi} \frac{zx^4 \exp(x/\theta)}{\left[\exp(x/\theta) - 1\right]^2} \left(\frac{k_{||,\perp}^* \sqrt{z^2 - 2z \cos \varphi + 1}}{1 + k_{||,\perp}^* Q_{l||,\perp}(x) \sqrt{z^2 - 2z \cos \varphi + 1}} + \right. \\ \left. + \frac{2k_{||,\perp}^* \sqrt{z^2 - 2z \cos \varphi + 1}}{1 + k_{||,\perp}^* Q_{l||,\perp}(x) \sqrt{z^2 - 2z \cos \varphi + 1}} \right) d\varphi dz dx \left\{ \int_0^1 \frac{x^4 \exp(x/\theta)}{\left[\exp(x/\theta) - 1\right]^2} \left(\frac{1}{Q_{l||,\perp}(x)} + \frac{2}{Q_{l||,\perp}(x)} \right) dx \right\}^{-1}. \quad (11)$$

In this formula, an additional designation is introduced

$$k_{||,\perp}^* = \frac{r_{||,\perp} \gamma^2}{\rho} \left(\frac{k_B T_D}{\hbar v_{||,\perp}} \right)^4 \left(\frac{k_B T_D}{v_{||,\perp}^2} \right). \quad (12)$$

From formula (11) it follows that for lattice thermal conductivity reduction by 30–40 % due to phonon scattering on contact boundaries, $k_{||}^*$ should make $69.6 \div 167.7$, and $k_{\perp} - 1008 \div 2691$. Therefore, contact radius should make $0.4 \div 1.1 \mu\text{m}$. In its lowest value this result coincides with the minimum contact radius necessary for maintenance of electric conductivity of shape-forming element of extruded material structure at a level of 90 % of single crystal electric conductivity. Thus, when passing from a single crystal to extruded material, its thermoelectric figure of merit should not drop, and with size optimization of shape-forming element of material structure this figure of merit can even increase.

Conclusions and recommendations

1. In the drift approximation with regard to charge carrier scattering on acoustic phonons and the boundaries of contact between material particles, as well as a real anisotropy of band spectrum and electric conductivity of material it is shown that when passing from a single crystal to extruded material, the electric conductivity of shape-forming element of material structure is maintained at a level not less than 90 % of its value in a single crystal, if contact radius between half-spheres is at least 10.4 of electron (hole) mean free path.
2. As applied to Bi_2Te_3 at a temperature of 300 K it means that contact radius should be at least $0.4 \mu\text{m}$, and such contacts can appear between particles of diameter $40 \div 80 \mu\text{m}$.
3. Retention or little change of thermoelectric figure of merit when passing from a single crystal to extruded material can be attributed to the fact that at phonon scattering on the boundaries of contact between half-spheres of shape-forming element, its thermal conductivity drops, whereas electric conductivity even with regard to charge carrier scattering on contact boundaries is maintained at the previous level.
4. Coincidence of these results with the results obtained in the isotropic approximation is due to the fact that charge carrier relaxation time, though considered anisotropic, depends on their full energy, rather than on each quasi-pulse component separately.
5. The same estimate for contact radius necessary for lattice thermal conductivity reduction due to phonon scattering on its boundaries by 30 to 40 % as compared to a single crystal results if alongside with scattering on the boundaries, one will consider normal processes together with Umklapp processes related to phonon-phonon scattering.

The authors are grateful to academician L. Anatychuk for statement of the problem and important critical remarks.

References

1. B.M. Goltzman, V.A. Kudinov, and I.A. Smirnov, *Semiconductor Thermoelectric Materials Based on Bi₂Te₃* (Moscow: Nauka, 1972), 320 p.
2. P.V. Gorsky, V.P. Mikhachenko, Reduction of Thermoelectric Material Lattice Thermal Conductivity Using Shape-Forming Element Optimization, *J. Thermoelectricity* **1**, 18 – 25 (2013).
3. P.V. Gorsky, V.P. Mikhachenko, On the Electric Conductivity of Contacting Particles of Thermoelectric Material, *J. Thermoelectricity* **2**, 12 – 18 (2013).
4. A. Misnar, *Thermal Conductivity of Solids, Liquids, Gases and Their Compositions* (Moscow: Mir, 1968), 464 p.
5. V.F. Gantmakher, I.B. Levinson, *Current Carrier Scattering in Metals and Semiconductors* (Moscow: Nauka, 1984), 350 p.
6. P.G. Klemens, Lattice Thermal Conductivity. – In: *Solid State Physics. Advances in Research and Applications*. Vol. 7, pp. 1-98 (New York: Academic Press. Inc. Publishers, 1958), 526 p.
7. P.G. Klemens, Influence of Thermal and Phonon Processes on Ultrasonic Decay. – In: *Physical Acoustics. Vol 3. Part B. Lattice Dynamics*. Ed. by W. Meson, pp. 244-284 (Moscow:Mir, 1968), 526 p.

Submitted 01.03.2013.

A.I. Casian, I.I. Sanduleac



A.I. Casian

Technical University of Moldova,
168, Stefan cel Mare Ave.,
MD-2004, Chisinau, Moldova



I.I. Sanduleac

**ORGANIC THERMOELECTRIC
MATERIALS: NEW OPPORTUNITIES**

The aim of the paper is to estimate the opportunities of organic materials for thermoelectric applications. Recently in molecular nanowires of conducting polymers the values of $ZT \sim 15$ were predicted. Still higher values of ZT have been predicted by us. However, these predictions were made in the frame of a strictly one-dimensional physical model. It is absolutely necessary to estimate the contribution of interchain interaction to these predictions. We present the results of thermoelectric properties modeling of tetrathiotetracene-iodide crystals, taking into account the interchain interaction. It is established that in crystals with not very high degree of purity this interaction can be neglected. However, in purer crystals it becomes important. The criteria when this interaction can be neglected, as well as the expected values of electrical conductivity, Seebeck coefficient and thermoelectric power factor limited by interchain interaction are determined.

Key words: thermoelectricity, electric conductivity, Seebeck coefficient, power factor, organic thermoelectric materials, tetrathiotetracene-iodide.

Introduction

Recent years have seen an increased number of publications devoted to investigation of thermoelectric opportunities of different organic materials. These materials have much more diverse and often unusual physical properties. As a rule, they have much lower thermal conductivity than the inorganic materials. It is expected that such materials will have much higher thermoelectric efficiency and will be less expensive in comparison with the known inorganic thermoelectric materials. Thus, exactly organic materials are good candidates for applications in the conversion of even a part of enormous low-grade waste heat into electrical energy.

From year to year the thermoelectric parameters of organic materials are improved. Now the highest measured value of the thermoelectric figure of merit at room temperature is $ZT = 0.57$ and was obtained in phenylacetylene-capped silicon nanoparticles [1]. The samples were prepared as pressed pellets. The measurements have shown very high value of Seebeck coefficient $S = 3228.8 \mu\text{V/K}$, modest electrical conductivity $\sigma = 18.1 \Omega^{-1}\cdot\text{m}^{-1}$, but low thermal conductivity $\kappa = 0.1 \text{ W}\cdot\text{m}^{-1}\cdot\text{K}^{-1}$. This value of ZT is rather close to that of ordinary thermoelectric materials.

Many different organic materials are investigated in order to improve their thermoelectric properties. In [2] it was shown that the iodine-doped pentacene thin films can be potential candidates for good organic thermoelectric materials. In a bilayer structure composed of an intrinsic pentacene layer and an acceptor tetrafluoro-tetracyanoquinodimethane layer the value of the power factor $P = \sigma S^2 \sim 2.0 \mu\text{W/mK}^2$ was measured [3], when layer thickness was optimized. Doped acetylene with very high electrical conductivity of the order of $1.1 \times 10^6 \Omega^{-1}\text{m}^{-1}$, $S = 28 \mu\text{V/K}$ and $\kappa = 0.7 \text{ W}\cdot\text{m}^{-1}\cdot\text{K}^{-1}$ has

demonstrated [4] $ZT = 0.38$ at room temperature. The problem is that this material is not stable, but this problem could be resolved in the future. In poly (3, 4-ethylenedioxothiophene) (PEDOT) the value of $ZT = 0.25$ was measured at room temperature with the parameters [5] $\sigma = 6700 \Omega^{-1} \cdot m^{-1}$, $S = 220 \mu V/K$, power factor $P = \sigma \cdot S^2 = 324 \mu W \cdot m^{-1} \cdot K^{-2}$, $\kappa = 0.37 W \cdot m^{-1} \cdot K^{-1}$, and the polymer is stable. It was also shown [6] that electrochemical doping, unlike chemical doping, allows better control of the oxidation level of polymer via tuning the electrode potential and measurement of the charging current, achieving in such a way improved thermoelectric properties.

The Japan Fujifilm Corp. announced in February 2013 about the development of a thermoelectric material (the site: greenoptimistic.com) using an organic polymer based on PEDOT with $ZT = 0.27$ and even higher. The material was elaborated in cooperation with Japan National Institute of Advanced Industrial Science and Technology. The advantages of this material are the low cost and that the converter module can be manufactured using printed technologies. A mini-review on the progress of poly (3, 4-ethylenedioxothiophene) (PEDOT)-based thermoelectric materials in recent years is presented in [7], where a $ZT \sim 1$ is predicted in this class of materials. In [8] both *n*-type and *p*-type organic thermoelectric materials have been developed with ZT values of 0.1 to 0.2 around 400 K. Thermoelectric module composed of 35 *n-p* couples was made which outputs a power of $2.8 \mu W \cdot cm^{-2}$ (highest for organic thermal devices ever reported) under temperature difference of $\Delta T = 80$ K.

Several works about inorganic-organic TE composites have been reported [9-14]. However, the obtained values of ZT are still very low. Different theoretical models were presented for the description of thermoelectric transport in organic materials [15-18]. In molecular nanowires of conducting polymers the values of $ZT \sim 15$ at room temperature were predicted [18]. It is important that in this paper the charge and energy transport was described in the hopping model which is applied in the case of strong electron-phonon interaction and usually yields smaller conductivity than the band model. It is also predicted that the largest power factor can reach $500 \mu W/cmK^2$ for PEDOT: PSS molecular chain, which is much larger than that for inorganic nanowires.

Still higher values of $ZT \sim 20$ were predicted by us [19-21] in highly conducting quasi-one dimensional (Q1D) charge transfer organic crystals. However, the above predictions were made in the frame of a strictly one dimensional physical model. Even if from the experimental data it is known that the interaction between molecular chains in Q1D crystals is weak, it is absolutely necessary to estimate the contribution of this interaction to the charge and heat transport.

The aim of present paper is to carry out a more detailed modeling of thermoelectric properties of tetrathiotetracene-iodide, TTT_2I_3 Q1D crystals, taking into account the interchain interaction. The results of paper [22] will be also verified in the frame of this more complete physical model. For simplicity the 2D crystal model is applied. It is established that in crystals with a low degree of purity this interaction can be neglected, because impurity scattering already limits carrier mobility. However, in purer crystals which allow higher values of ZT , this interaction becomes important. The criteria when this interaction can be neglected are determined. The expected values of electrical conductivity, the Seebeck coefficient and thermoelectric power factor limited by interchain interaction are also determined.

2. Two-dimensional crystal model for TTT_2I_3

The quasi-one-dimensional organic crystals of tetrathiotetracene-iodide, TTT_2I_3 , are formed of segregate chains or stacks of planar molecules of tetrathiotetracene TTT , and iodine ions. This compound is of mixed-valence: two molecules of TTT give one electron to the iodine chain which is formed from I_3^- ions. Only TTT chains are electrically conductive and the carriers are holes. The

crystals admit nonstoichiometric composition of the form $TTT_2I_{3\pm\delta}$ with the surplus or deficiency of iodine. So as the iodine plays the role of acceptor, the hole concentration depends on the iodine content and may be higher or lower than stoichiometric concentration $n = 1.2 \times 10^{21} \text{ cm}^{-3}$. It is very important because in thermoelectric materials it is usually necessary to optimize carrier concentration in order to achieve maximum efficiency.

The crystals are named quasi-one-dimensional because the carriers are moving mainly along the conducting molecular chains and rarely jump from one chain to another. As a result, the electrical conductivity along the TTT chains is approximately by three orders of magnitude higher than in transversal to chains directions. The transport mechanism along the chains is of band type, whereas in the transversal direction is of hopping type. Due to this fact, earlier [23-25] we neglected the latest mechanism and considered a strictly one-dimensional crystal model. In other words, we neglected the possibility for a carrier to pass from one to another conducting chain. This approximation has permitted us to investigate the thermoelectric properties of these crystals in a simpler physical model. Now we will take into account this possibility, in order to determine how this new interaction will modify the previously estimated values of thermoelectric efficiency.

For simplicity we will consider two-dimensional crystal model. The charge and energy transport are described in the tight binding and nearest neighbors approximations. The energy of hole with the 2D quasi-wave vector \mathbf{k} and projections (k_x, k_y) is of the form

$$\epsilon(\mathbf{k}) = -2w_1[1 - \cos(k_x b)] - 2w_2[1 - \cos(k_y a)]. \quad (1)$$

The energy is measured from the upper margin of the conduction band, w_1 and w_2 are the carrier transfer energies between the nearest molecules along and between the chains, b and a are lattice constants along and in transversal direction to the chains. The axis x is directed along \mathbf{b} , and y is in perpendicular direction. The condition of crystal quasi-one-dimensionality means that $w_2 \ll w_1$. The frequency of longitudinal acoustic phonons is given below

$$\omega_q^2 = \omega_1^2 \sin^2(q_x b / 2) + \omega_2^2 \sin^2(q_y a / 2), \quad (2)$$

where 2D quasi-wave vector \mathbf{q} has the projections (q_x, q_y) , and ω_1 and ω_2 are the limit frequencies in the x and y directions, $\omega_2 \ll \omega_1$.

The two most important hole-phonon interactions considered earlier are completed by taking into account the interchain hopping of carriers. The first interaction is similar to that of deformation potential. The second interaction is similar to that of polaron, but is determined by induced polarization of molecules surrounding the conduction hole. The square of matrix element module of total interaction is of the form

$$|A(\mathbf{k}, \mathbf{q})|^2 = 2\hbar / (NM\omega_q) \{w_1'^2 [\sin(k_x b) - \sin((k_x - q_x)b) + \gamma_1 \sin(q_x b)]^2 + \\ + w_2'^2 [\sin(k_y a) - \sin((k_y - q_y)a) + \gamma_2 \sin(q_y a)]^2\} \quad (3)$$

Here N is the number of molecules in the basic region of the crystal, M is the mass of TTT molecule, w_1' and w_2' are the derivatives with respect to the intermolecular distance of the energies w_1 and w_2 . In Eq. 3, the terms which depend on k_x and k_y describe the first interaction, and the terms which depend only on q_x and q_y describe the second interaction. The parameters γ_1 and γ_2 have the meaning of the ratios of amplitudes of second interaction to the first one along and in transversal direction to the chains

$$\gamma_1 = 2e^2 \alpha_0 / (b^5 w'_1), \quad \gamma_2 = 2e^2 \alpha_0 / (a^5 w'_2) \quad (4)$$

where e is the carrier charge and α_0 is the average polarizability of TTT molecule. Note that so as w_1 and w_2 are positive and exponentially decrease with the increase of intermolecular distance, w'_1 and w'_2 will be negative, and γ_1 and γ_2 will be likewise negative.

Since the conduction band is not very large and the Debye temperature is relatively low, the variation of wave vectors \mathbf{k} and \mathbf{q} should be taken over the entire Brillouin zones for holes and phonons: $-\pi/b \leq k_x \leq \pi/b$, $-\pi/a \leq k_y \leq \pi/a$, $-\pi/b \leq q_x \leq \pi/b$, $-\pi/a \leq q_y \leq \pi/a$.

The impurity scattering of holes is also taken into account. The impurities are considered point like and neutral. In this case the impurity scattering rate is described by the dimensionless parameter D_0 which is proportional to impurity concentration and can be made very small, if the crystal purity is rather high.

3. Charge and energy transport

We will consider that a weak electrical field and temperature gradient are applied along the chains. In this case the kinetic equation for nonequilibrium distribution function can be linearized and it takes the form of the Boltzmann equation. Near room temperature we can neglect in the scattering process of a hole from the state \mathbf{k} to $\mathbf{k} \pm \mathbf{q}$ the phonon energy and the transversal kinetic energy of the hole, because these energies are much less than the kinetic energy of the hole along the chains. Then the kinetic equation is solved analytically and the notion of relaxation time can be introduced as in 1D case. But now the relaxation time is a function of k_x and k_y

$$\tau(k_x, k_y) = \frac{\hbar M v_{s1}^2 w_1 |\sin(k_x b)|}{4b^2 k_0 T w_1'^2 [(1 - \gamma_1 \cos(k_x b))^2 + D_0 + w_2'^2 (1 + \gamma_2^2 + 2 \sin^2(k_y a) - 2\gamma_2 \cos(k_y a)) / (2w_1'^2 \sin^2(k_x b))]} \quad (5)$$

In deriving Eq. 5 the term proportional to $(bv_{s2} / av_{s1})^2$ which comes from the phonon dispersion law and is much less than unity was neglected, where v_{s1} is the sound velocity along the chains and v_{s2} is the sound velocity in the direction perpendicular to chains, k_0 is the Boltzmann constant. Also, in Eq. 5 we have replaced the phonon distribution function N_q by its high temperature limit $N_q \equiv k_0 T / \hbar \omega_q \gg 1$, so as near room temperature T_0 we have $\hbar \omega_q \ll k_0 T_0$. We have also changed the signs of γ_1 and γ_2 . From here and further γ_1 and γ_2 are positive.

If in Eq. 5 the interchain interaction is neglected, i.e. if we put $w_2 = 0$, $w'_2 = 0$, and $\gamma_2 = 0$, the previous results which correspond to 1D model are obtained. It is seen that the relaxation time has a maximum for values of k_x close to those for which the first term in the denominator of (5) is equal to zero. It means that for these values of k_x in the conducting band the two hole-phonon interactions mentioned above strongly compensate each other. In 1D case the height of relaxation time maximum is limited by parameter D_0 , i.e. by the carrier scattering on impurity. Since the improvement of the thermoelectric properties is determined by the height of the relaxation time, it was recommended to increase the crystal purity in order to diminish D_0 and increase the maximum of relaxation time as much as possible. In 2D model the height of maximum is also limited by the interchain interaction. Now we have to determine the values of parameters, when the last interaction becomes more important. In this case the further purification of crystal in order to diminish D_0 will not improve the thermoelectric properties, because the interchain interaction already limits the height of relaxation time.

With the help of (5), the electrical conductivity along TTT chains σ_{xx} , the thermopower (Seebeck coefficient) S_{xx} and the power factor P_{xx} can be expressed through the transport integrals as follows

$$\sigma_{xx} = \sigma_0 R_0, \quad S_{xx} = (k_0 / e) (2w_1 / k_0 T) R_1 / R_0, \quad P_{xx} = \sigma_{xx} S_{xx}^2, \quad (6)$$

where

$$\sigma_0 = (2e^2 M v_{s1}^2 w_1^2 r) / (\pi^2 \hbar abc (k_0 T)^2 w_1'^2), \quad (7)$$

r is the number of chains through the transversal section of the unit cell and R_n are the dimensionless transport integrals

$$R_n = \int_0^2 d\epsilon \int_0^\pi \frac{(\epsilon - \epsilon_F)^n \epsilon (2 - \epsilon) n_{\epsilon,\eta} (1 - n_{\epsilon,\eta}) d\eta}{\gamma_1^2 (\epsilon - \epsilon_0)^2 + D_0 + w_2'^2 (1 + \gamma_2^2 + 2 \sin^2 \eta - 2\gamma_2 \cos \eta) / (2w_1'^2 \epsilon (2 - \epsilon))}. \quad (8)$$

Here, in order to obtain an expression for transport integrals (and also for relaxation time) closer to previous 1D case, we have introduced instead of k_x a new variable $\epsilon = (1 - \cos(k_x b))$, where ϵ has the meaning of dimensionless kinetic energy of a hole along chains measured from the bottom of conduction band in units of $2w$ and $\epsilon_0 = (\gamma_1 - 1)/\gamma_1$ has the meaning of resonance energy (in the same units) which corresponds to relaxation time maximum. Also, instead of k_y a dimensionless projection $\eta = k_y a$ was introduced, and $n_{\epsilon,\eta}$ is the Fermi distribution function in the variables ϵ and η . If in Eq. 8 we put $w_2' = 0$, and $\gamma_2 = 0$, the previous results which correspond to 1D model are obtained.

Thermoelectric properties

Unfortunately, the thermoelectric properties can be investigated only numerically. Expressions (6) – (8) have been calculated for quasi-one-dimensional organic crystals of TTT_2I_3 with different degrees of purity. The crystal parameters are: $M = 6.5 \times 10^5 m_e$ (m_e is the mass of free electron), $a = 18.35 \text{ \AA}$, $b = 4.96 \text{ \AA}$, $c = 18.46 \text{ \AA}$, $v_{s1} = 1.5 \times 10^3 \text{ m/s}$, $w_1 = 0.16 \text{ eV}$, $w_1' = 0.26 \text{ eV\AA}^{-1}$, $r = 4$. The parameters w_2 and w_2' were estimated in Ref. 26, $w_2 = 1.44 \times 10^{-3} \text{ eV}$ and $w_2' = 2.34 \times 10^{-3} \text{ eV\AA}^{-1}$. The value of polarizability α_0 in TTT_2I_3 can be estimated approximately comparing with the known polarizabilities of other molecules of the same type. We have taken $\alpha_0 = 45 \text{ \AA}^3$, to which corresponds $\gamma = 1.7$, as in [22]. For γ_2 it follows that $\gamma_2 = \gamma_1 (a^5 w_1') / (b^5 w_2') = 3.47 \gamma_1$, i.e. $\gamma_2 = 5.9$.

For the parameter D_0 we will choose three values: 0.3 that corresponds to crystals grown by gas phase method [27] with $\sigma \sim 3500 \Omega^{-1} \cdot \text{cm}^{-1}$; 0.1 that corresponds to crystals grown by gas phase method in [28] with $\sigma \sim 10^4 \Omega^{-1} \cdot \text{cm}^{-1}$ and 0.05 which corresponds to purer crystals with somewhat higher $\sigma \sim 1.7 \times 10^4 \Omega^{-1} \text{ cm}^{-1}$.

In Fig. 1 the dependences of electrical conductivity along chains σ_{xx} on the Fermi energy in units of $2w_1$ are presented for these values of D_0 . In stoichiometric crystals of TTT_2I_3 the hole concentration is $n = 1.2 \times 10^{21} \text{ cm}^{-3}$, to which corresponds $\epsilon_F \sim 0.37$. From Fig. 1 it is seen that the values of σ_{xx} calculated in more complete 2D model practically coincide with those calculated in 1D approximation for the entire interval of the Fermi energy variation. This means that for stoichiometric crystals, the more so for those with a lower carrier concentration needed for the improvement of thermoelectric properties, but with the same degree of purity, it is sufficient to apply the simpler 1D approximation.

In Fig. 2 the dependences of thermopower (Seebeck coefficient) S_{xx} on the Fermi energy at room temperature are presented. It is seen that for crystals with considered degree of purity the interchain interaction has even lower effect on thermopower than on σ_{xx} : the curves for 1D and 2D models coincide. This also means that, due to an additional factor $(\epsilon - \epsilon_F)$ in the numerator of integrand in (8), the value of relaxation time maximum has a lower effect on the thermopower than on the electrical conductivity. In Fig. 3 the dependences of the thermoelectric power factor P_{xx} on the

Fermi energy E_F are presented. It is seen that the curves for 1D and 2D models are very close to each other. For $\varepsilon_F = 0.2$ the value of P_{xx} is $\sim 1.4 \times 10^{-2} \text{ W/m}\cdot\text{K}^2$, or 3.5 times higher than in Bi_2Te_3 .

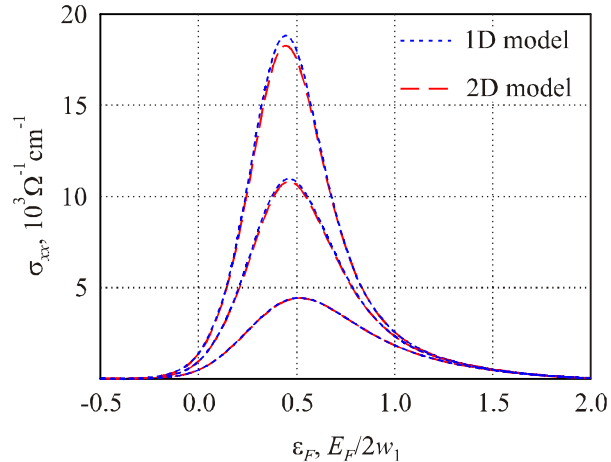


Fig. 1. Electrical conductivity along chains as a function of E_F for $\gamma = 1.7$: lower, middle and upper curves are for $D_0 = 0.3, 0.1$ and 0.05 , respectively.

In order to determine when the interchain interaction becomes important, let's consider still more pure crystals of TTT_2I_3 with lower values of parameter D_0 : 0.04, 0.03 and 0.02. To these values of D_0 and stoichiometric carrier concentration correspond $\sigma_{xx} \sim 2 \times 10^4 \Omega^{-1}\cdot\text{cm}^{-1}$, $2.5 \times 10^4 \Omega^{-1}\cdot\text{cm}^{-1}$ and $3.2 \times 10^4 \Omega^{-1}\cdot\text{cm}^{-1}$, respectively. Crystals of TTT_2I_3 with such a high degree of purity and, respectively, with such a high conductivity have not been synthesized yet, but it is possible in the future.

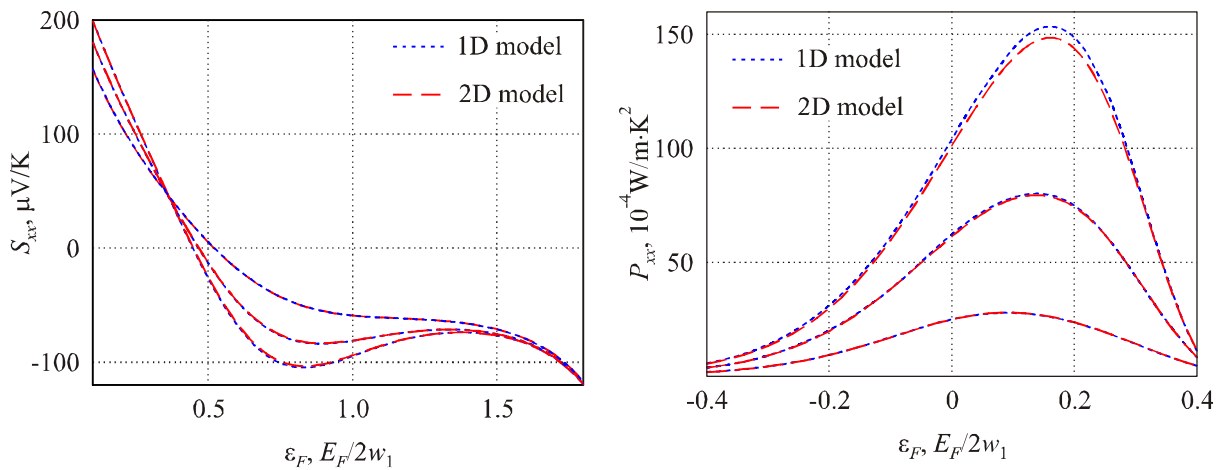


Fig. 2. Thermopower S_{xx} as a function of E_F : lower, middle and upper curves are for $D_0 = 0.05, 0.1$ and 0.3 , respectively.

Fig. 3. Thermoelectric power factor as a function of E_F : lower, middle and upper curves are for $D_0 = 0.3, 0.1$ and 0.05 , respectively.

In Fig. 4 the dependences of electrical conductivity along chains σ_{xx} on the Fermi energy are presented for these lower values of D_0 . It is seen that now the deviations between 2D and 1D models are more significant, especially in the case of the purest crystals with $D_0 = 0.02$, when for stoichiometric crystals the value of conductivity in 2D model is by 10 % lower than in 1D one. But for crystals with ε_F around 0.2, needed in order to increase the power factor, the curves for 2D and 1D models practically coincide.

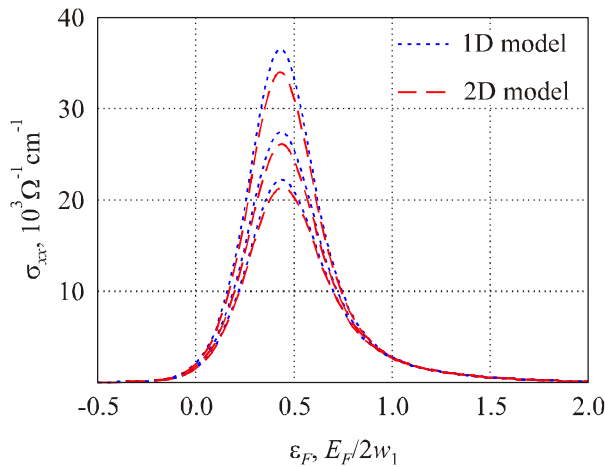


Fig. 4. Electrical conductivity along chains as a function of E_F : lower, middle and upper curves are for $D_0 = 0.04, 0.03$ and 0.02 , respectively.

In Fig. 5 the dependences of thermopower S_{xx} on the Fermi energy are presented. As it was expected, in this case the deviations between 2D and 1D models are still smaller than for σ_{xx} , the dotted and dashed curves practically coincide, especially in the interval of ϵ_F between 0.2 and 0.4. This is an additional confirmation that the height of relaxation time maximum has a lower effect on S_{xx} than on σ_{xx} . In this case for the calculation of thermopower S_{xx} it is sufficient to apply the simpler 1D model.

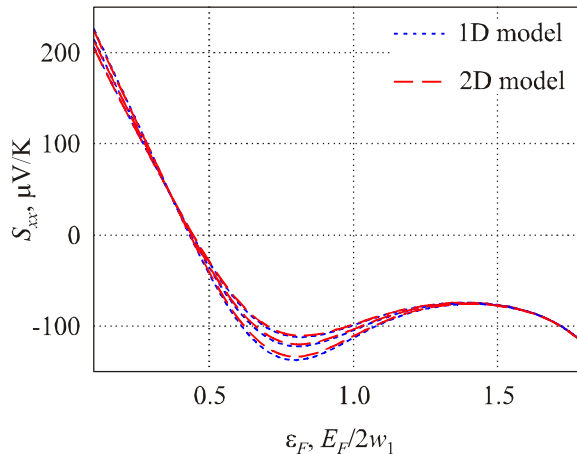


Fig. 5. Thermopower S_{xx} as a function of E_F : lower, middle and upper curves are for $D_0 = 0.02, 0.03$ and 0.04 , respectively.

The dependences of the thermoelectric power factor P_{xx} on the Fermi energy are presented in Fig. 6. Now, the deviations between 2D and 1D models, accumulated from σ_{xx} and S_{xx} , have been increased, but to a little degree. So, even in the purest crystals with $D_0 = 0.02$ the maximum value of P_{xx} is lower in 2D case only by 10 %. Taking into account that the modeling error is also $\sim 10\%$, we can conclude that for all crystals with degrees of purity considered here the simpler 1D physical model is applicable and previously predicted results for the improvement of the thermoelectric properties of TTT_2I_3 crystals are valid. Thus, in earlier synthesized crystals with $\sigma_{xx} \sim 10^4 \Omega^{-1} \cdot \text{cm}^{-1}$ [28] it is expected to obtain after optimization of carrier concentration a value of $P_{xx} \sim 8 \times 10^{-3} \text{ W/m} \cdot \text{K}^2$ (see Fig. 3, the line with $D_0 = 0.1$), or twice higher than in Bi_2Te_3 . In the purest crystals with $\sigma_{xx} \sim 3.2 \times 10^4 \Omega^{-1} \cdot \text{cm}^{-1}$ for stoichiometric compounds, the maximum value of P_{xx} is expected to be $\sim 3.2 \times 10^{-2} \text{ W/m} \cdot \text{K}^2$ (see Fig. 6, the line with

$D_0 = 0.02$), or 8 times higher than in Bi_2Te_3 . To this value of P_{xx} correspond $\sigma_{xx} = 9 \times 10^3 \Omega^{-1} \cdot cm^{-1}$ and $S_{xx} = 190 \mu V/K$. It is very good predicted result. Of course, for crystals with still higher degree of purity the interchain interaction must be taken into account.

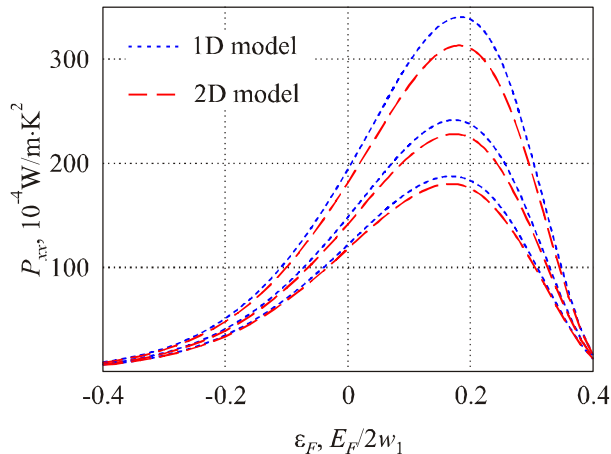


Fig. 6. Thermoelectric power factor as a function of E_F : lower, middle and upper curves are for $D_0 = 0.04, 0.03$ and 0.02 , respectively.

Conclusions

The investigations of new organic materials for thermoelectric applications published in the last two years are analyzed. Organic materials attract the increasing attention of investigators. These materials are expected to have higher efficiency and to be less expensive than the known inorganic ones. The highest measured value of the thermoelectric figure of merit ZT at room temperature is $ZT = 0.57$ and was obtained in phenylacetylene-capped silicon nanoparticles. This value of ZT is rather close to that of ordinary thermoelectric materials. In poly (3, 4-ethylenedioxythiophene) (PEDOT) the value of $ZT = 0.25$ has been measured with the parameters [5] $\sigma = 6700 \Omega^{-1} \cdot m^{-1}$, $S = 220 \mu V/K$, power factor $P = \sigma \cdot S^2 = 324 \mu W \cdot m^{-1} \cdot K^{-2}$, thermal conductivity $\kappa = 0.37 W \cdot m^{-1} \cdot K^{-1}$, and the polymer is stable. $ZT \sim 1$ is predicted in this class of materials [7]. Several works on inorganic-organic TE composites have been reported, however, the obtained values of ZT are still very low. Different theoretical models were also presented. It is interesting that in molecular nanowires of conducting polymers the values of $ZT \sim 15$ at room temperature were predicted [18] in spite of hopping conduction mechanism. Earlier we have predicted in quasi-one-dimensional organic crystals even higher values of ZT at room temperature. However, this and above predictions were made in the frame of a strictly one-dimensional crystal model. In the present paper, we have taken into account the possibility for a carrier to pass from one molecular chain to another in the frame of a two-dimensional physical model. The crystals of tetrathiotetracene-iodide, TTT_2I_3 are considered. It is shown that in crystals with not very high degree of purity this additional interaction can be neglected, because impurity scattering already limits carrier mobility. The predicted parameters in this case are: $\sigma_{xx} = 9 \times 10^3 \Omega^{-1} \cdot cm^{-1}$, $S_{xx} = 190 \mu V/K$ and $P_{xx} = 3.2 \times 10^{-2} W/m \cdot K^2$, or 8 times higher than in Bi_2Te_3 . For TTT_2I_3 it is possible to neglect the interchain interaction and to apply 1D approximation for stoichiometric crystals with electrical conductivity along the chains up to $\sigma_{xx} \sim 4 \times 10^4 \Omega^{-1} \cdot cm^{-1}$ or a little higher. However, in purer crystals with higher values of σ_{xx} , the interchain interaction becomes important.

We acknowledge the support of EU Commission FP7 program under the grant no. 308768.

References

1. S.P. Ashby, J. Garcia-Canadas, G. Min, and Y. Chao, Measurement of Thermoelectric Properties of Phenylacetylene-Capped Silicon Nanoparticles and Their Potential in Fabrication of Thermoelectric Materials, *JEM*, DOI: 10.1007/s11664-012-2297-x (2012).
2. K. Hayashi, T. Shinano, Y. Miyazaki and T. Kajitani, Fabrication of Iodine-Doped Pentacene Thin Films for Organic Thermoelectric Devices, *J. Appl. Phys.* **109**, 023712, 2011.
3. K. Harada, M. Sumino, C. Adachi, S. Tanaka and K. Miyazaki, Improved Thermoelectric Performance of Organic Thin-Film Elements Utilizing a Bilayer Structure of Pentacene and 2, 3, 5, 6-tetrafluoro-7, 7, 8, 8-tetracyanoquinodimethane (F4-TCNQ), *Appl. Phys. Lett.* **96**, 253304, 2010.
4. Y. Xuan, et al., Thermoelectric properties of Conducting Polymers: The Case of Poly (3-hexylthiophene), *Phys. Rev. B* **82**, 115454, 2010.
5. O. Bubnova, et al., Optimization of the Thermoelectric Figure of Merit in the Conducting Polymer Poly (3,4-Ethylenedioxythiophene), *Nature Materials* **10**, 429, 2011. DOI: 10.1038/NMAT3012.
6. O. Bubnova, M. Berggren, and X. Crispin, Tuning the Thermoelectric Properties of Conducting Polymers in an Electrochemical Transistor, *J. Am. Chem. Soc.* **134**, 16456 (2012).
7. R. Yue and L. Xu, Poly (3, 4-ethylenedioxythiophene) as Promising Organic Thermoelectric Materials: A Mini-Review, *Synt. Met.* **162**, 912 (2012).
8. Y. Sun et al., Organic Thermoelectric Materials and Devices Based on *p*- and *n*-type Poly (metal 1, 1, 2, 2-ethenetetrathiolate)s, *Adv. Mater.* **24**, 932 (2012).
9. Y.Y. Wang, K.F. Cai, J.L. Yin, B.J. An, Y. Du, and X. Yao, In Situ Fabrication and Thermoelectric Properties of PbTe-polyaniline Composite Nanostructures, *J. Nanopart Res.* **13**, 533 (2011).
10. W.Q. Ao, L. Wang, J.Q. Li, F. Pan, and C.N. Wu, Synthesis and Characterization of Polythiophene/Bi₂Te₃ Nanocomposite Thermoelectric Material, *J. Electron. Mat.* **40**, 9(2011).
11. N. Toshima, N. Jiravanichanun, and H. Marutani, Organic Thermoelectric Materials Composed of Conducting Polymers and Metal Particles. *J. Electron. Mat.* **41**, 6 (2012).
12. Y. Wang, K. Cai, and X. Yao, Facile Fabrication and Thermoelectric Properties of PbTe-Modified Poly (3, 4-ethylenedioxythiophene) Nanotubes, *ACS Appl. Mater. Interfaces* **3**, 1163 (2011).
13. J. Carrete, N. Mingo, G. Tian, H. Agren, A. Baev, and P.N. Prasad, Thermoelectric Properties of Hybrid Organic-Inorganic Superlattices, *The Journal of Physical Chemistry C*, **116** (20), 10881 (2012).
14. C. Yu, K. Choi, L. Yin, and J.C. Grunlan, Light-Weight Flexible Carbon Nanotube Based Organic Composites with Large Thermoelectric Power Factors, *ACS Nano*, **5** (10), 7885 (2011).
15. G. Kim and K.P. Pipe, Thermoelectric Model to Characterize Carrier Transport in Organic Semiconductors, *Phys. Rev. B* **86**, 085208 (2012).
16. D.S. Dudis, J.D. Ferguson, M. Check, J.E. Schmidt, E.R. Kemp, T. Robbins, J.A. Shumaker, G. Chen, H.A. Seibel, Multidimensional Nanoscopic Approaches to New Thermoelectric Materials, *Proc. SPIE* 76830S (2010).
17. J. Chen, D. Wang, Z. Shuai, First-Principles Predictions of Thermoelectric Figure of Merit for Organic Materials: Deformation Potential Approximation, *J. Chem. Theory Comput.* **8** (9), 3338 (2012).
18. Y. Wang, J. Zhou, and R. Yang, Thermoelectric Properties of Molecular Nanowires, *J. Phys. Chem. C* **115**, 24418 (2011).
19. Casian, Z. Dashevsky, H. Scherrer, V. Dusciac, and R. Dusciac, *Proc. of 22nd Intern. Conf. on Thermoel.*, La Grande-Motte, France (IEEE, Piscataway, NJ, 2004), p. 330-335.A. Casian, in:

- Thermoelectric Handbook, Macro to Nano*, Ed. by D.M. Rowe, CRC Press, 2006, Chap.36.
20. Casian, Prospects of the Thermoelectricity Based on Organic Materials, *J. Thermoelectricity* **3**, 45-50 (2007).
21. A.I. Casian, B.M. Gorelov, and I.V. Dubrovin, State of the Art and Prospects of Thermoelectricity on Organic Materials, *J. Thermoelectricity* **3**, 7-16 (2012).
22. Casian, V. Dusciac and Iu. Coropceanu, Huge Carrier Mobilities Expected in Quasi-One-Dimensional Organic Crystals. *Phys. Rev. B* **66**, 165404 (2002).
23. Casian, V. Dusciac, and V. Nicic, Thermoelectric Opportunities of Quasi-One-Dimensional Organic Crystals of Tetrathiotetracene-Iodide, *J. Thermoelectricity* **2**, 33-39 (2009).
24. Casian, J. Stockholm, V. Dusciac, and V. Nicik, Low-Dimensional Organic Crystal Tetrathiotetracene-Iodide as Thermoelectric Material: Reality and Prospects, *J. Nanoelectronics and Optoelectronics* **4**, 95-100 (2009).
25. Casian, I. Sanduleac, Effect of Interchain Interaction on Electrical Conductivity in Quasi-One-Dimensional Organic Crystals of Tetrathiotetracene-Iodide, *J. Nanoelectronics and Optoelectronics* **7**, 706-711 (2012).
26. I.C. Isset, Magnetic Susceptibility, Electrical Resistivity and Thermoelectric Power Measurements of Bis(tetrahtiotetracene)-Triiodide, *Phys. Rev.* **18**, 439 (1978)
27. Hilti and C.W. Mayer, Electrical Properties of the Organic Metallic Compound bis (Tetrathiotetracene)-Triiodide, $(TTT)_2I_3$, *Helvetica Chimica Acta* **61** (40), 501 (1978).

Submitted 16.05.2013.

E.M. Godzhayev², S.Sh. Kakhramanov¹, K.J. Gulmamedov², A.Yu. Gamzayeva³

¹Scientific-Production Association “Selen” of the NAS of Azerbaijan,
14, F. Agayev Str., Baku, 370143, Azerbaijan;

²Azerbaijan Technical University, 25, Huseyn Javid Ave.,
Baku, AZ1073, Republic Azerbaijan;

³Gyandzha State University, 187, Shah Ismail Xetai,
Gyandzha, AZ2000, Azerbaijan

SURFACE NANOPARTICLES IN $A^V_2B^{VI}_3$

Nanoparticles formed on (0001) $A^V_2B^{VI}_3$ surface are a specific class of nanoobjects affecting the properties of the bulk crystals. Their clustering in $Te^{(I)}\text{-}Te^{(I)}$ space occurs with aggregation of diffusing atoms according to the same mechanisms as in known solid-state structures formed on the free surface of crystals. Analysis of nanofragment structure and morphology conducted on the basis of AFM images and X-ray diffraction images on (0001) $A^V_2B^{VI}_3$ surface has revealed the role of van der Waals gap as a solid-phase nanoreactor during intercalation for $Sb_2Te_3 <Cr>$ and $(Bi_2Te_3\text{-}Bi_2Se_3) <ZnSe>$ solid solution.

Key words: X-ray diffraction image, diluted magnetic semiconductors, fractal clusters, nanoreactors.

Introduction

Looking for ways to improve the thermoelectric figure of merit of substances, apart from fundamental significance is also of applied importance for solving practical tasks of producing low temperatures by thermoelectric methods.

To this day it has been established that diluted magnetic semiconductors based on the elements of III and V or II and IV groups of periodic system pass into ferromagnetic state at low temperatures. Ferromagnetism was quite recently discovered in bismuth telluride with *Fe*, and then in antimony telluride with V at low temperatures. The influence of magnetic impurities on thermoEMF, resistance, magnetism, the Hall effect, the Shubnikov-de Haas effect and other properties of such crystals was discovered [1].

Study of materials with high thermoelectric figure of merit is of particular relevance today. Optimal parameter values are achieved by introducing various doping impurities. In so doing, to achieve high thermoelectric figure of merit, one should study the fundamental physical properties of materials.

As the doping impurities *Cr*, *Zn* can be used. However, to this date the effect of these impurities on the energy spectrum of $(Bi_{1-x}Sb_x)_2Te_3$ mixed crystals is poorly understood, no data is available on the thermoelectric figure of merit of diluted magnetic semiconductors based on antimony telluride and the effect of magnetic impurities on the oscillation properties of such crystals. There is no information on the thermoelectric properties of mixed $(Bi_{1-x}Sb_x)_2Te_3$ crystals doped with chromium. The Fermi surface anisotropy of *p*- $(Bi_{1-x}Sb_x)$ single crystals and Bi_2Te_3 type crystals has not been determined by direct methods.

In this work, three types of samples were investigated.

The first type is mixed single crystals of bismuth and antimony tellurides, both undoped and doped. The second type is single crystals of antimony telluride doped with chromium magnetic impurity. Samples of the third type are single crystals of iron doped single crystals of bismuth telluride and selenide.

In [1], systematic study of the effect of chromium doping on galvanomagnetic, thermoelectric, oscillation and magnetic properties of layered Sb_2Te_3 single crystals was performed in the temperature range of 1.7 – 300 K. The Fermi surface anisotropy was determined by direct measurements of the angular dependences of the Fermi surface extreme sections with the aid of the Shubnikov-de Haas effect of $(Bi_{0.5}Sb_{0.5})_2Te_3$ single crystals.

The totality of data on the influence of doping with gallium, chromium and iron on thermoEMF, galvanomagnetic properties and energy spectrum is necessary for the optimization of devices and instruments based on bismuth and antimony tellurides. The use of investigated impurities *Ga*, *Cr*, *Fe* increases thermoEMF, and magnetic impurities *Cr*, *Fe*, *Ga* can be used for creation of new solid-state devices with magnetic field control. The results of research results can serve the basis for the development of a promising technology of producing materials with assigned properties on the basis of semiconductors of bismuth and antimony telluride types.

In [2], approaches to synthesis of nanocomposites based on zero-, one- and two- dimensional solid-state nanoreactors formed by zeolite cavities or interlayer voids of layered compounds are considered.

Bi_2Te_3 nanowires were obtained in the matrix of porous aluminum oxide [3]. However, in Bi_2Te_3 itself, as a result of crystallization, nanosized particles are formed in the interlayers of superstoichiometric atoms [4], and fractal structures are analyzed in terms of physics of fractal clusters. They are formed during nanoislands growth process with adhesion of solid particles [5-6]. Surface morphology study of (0001) Bi_2Te_3 <impurity> and consideration of interlayer aggregates with observed nanolayer assemblies [6] required to clarify the influence of self-organized nanoparticles based on impurities between $Te^{(1)}\text{-}Te^{(1)} A^V_2B^{VI}_3$ on thermoelectric properties.

This called for new experimental data on studying the surface morphology of (0001) $A^V_2B^{VI}_3$ doped with metals (*Zn*, *Se*, *Cr*).

In the light of the foregoing, the following purpose can be formulated: using *X*-ray diffraction and atomic force microscopy methods, to determine the composition of resulting intercalated interlayer nanofragments, using $Te^{(1)}\text{-}Te^{(1)} A^V_2B^{VI}_3$ space as a nanoreactor.

1. Experiment and results

Bi_2Te_3 compound was prepared by thermal synthesis at 900 – 950 K, which was generally carried out in quartz ampoules where *Bi*, *Te* and impurities were loaded in proper ratio. The synthesized alloys were loaded into graphitized ampoules (diameter 8 mm), alloyed again and then, vertical directional crystallization was used to get single-crystal ingots with temperature gradient $\Delta T = 120$ degrees/cm and crystallization rate 1.4 cm/h. In such crystals, after cleaving along (0001) Bi_2Te_3 plane, the morphology of impurity nanoparticles was studied. Structurally, such samples can be considered as intercalation ones, since one can single out the layers of host array and guest (impurities) in them. Because of a weak chemical bond between $Te^{(1)}\text{-}Te^{(1)}$ a change in morphology of interlayer space with penetration of metal atoms and formation of semiconductor nanoparticles is typical here.

Intercalation of *Zn* and *Cr* atoms was performed at 600 K. For this purpose, thermal technique was used to evaporate metals on purified surface along basis plane (0001) onto sample end face. Later the process of intercalation along (0001) layers was conducted at temperature gradient $\Delta T = 50$ degrees/cm, the evaporated part of the sample serving the hot side. On the samples obtained by this method the as-cleaved (0001) surfaces were investigated and the electron microscopic images and *X*-ray diffraction patterns were analyzed.

1.1. AFM and XRD studies

Electron microscopic images were obtained on NC-AFM atomic force microscope. X-ray diffraction studies were carried out on Philips Panalytical installation (X-ray diffractometer). Preparation of pure surface by cleavage with special tools was done along (0001) basis plane in the air immediately prior to conducting the experiments.

For all doped samples, apart from 3D AFM images of (0001) $A^{V_2}B^{VI_3}$ surface, there were investigated 2D AFM images, the distribution functions of equal-size nanoparticles, the density of distribution of nanofractals on (0001) surface along the height.

Nanoislands of nanosize 5 – 10 nm, assumed to be nanoparticles, were obtained in $Sb_2Te_3<Cr>$, $Bi_2Te_3<Cr>$, $Bi_2Se_3<Se>$ single crystals between $Te^{(1)}$ - $Te^{(1)}$ layers.

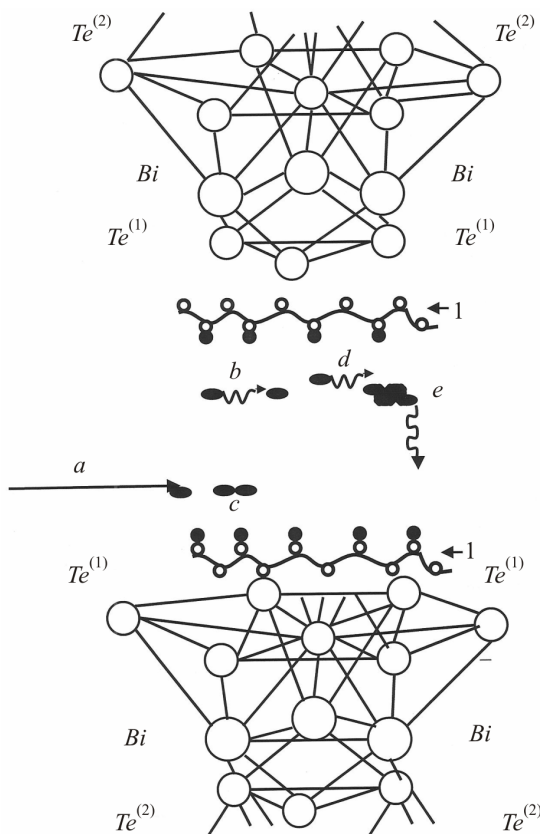


Fig. 1. Schematic of arrangement of bismuth and telluride atoms in Bi_2Te_3 structure, model approximations of nanoparticles between $Te^{(1)}$ - $Te^{(1)}$ at intercalation of easily diffusible impurities into interlayers: a – atom inclusions along (0001) plane; b – formation of a new island; b and d – diffusion of particles; c – aggregation; e – island diffusion; 1 – aggregation of particles between $Te^{(1)}$ - $Te^{(1)}$.

In $A^{V_2}B^{VI_3}$ the guest atoms (ZnSe, Cr) are localized in van der Waals space between telluride quintets. A quintet consists of five simple layers. Atoms of individual layer are identical and form a plane hexagonal lattice. Atoms of each subsequent layer are arranged above the centres of triangles formed by the atoms of previous layer. $Te^{(1)}$ atoms have as the nearest neighbours six Bi atoms, three from each adjacent layer. On the one side $Te^{(1)}$ is bound with three Bi atoms, and on the other side – with three $Te^{(1)}$ atoms, i.e. in the lattice there are two essentially different places for Te atoms [4]. Fig. 1 shows a schematic of atoms arrangement in Bi_2Te_3 crystal lattice, the ways of diffusion (marked by arrow (a)) and aggregation of particles between telluride quintets (b, e, c) leading to formation of nanolayers (1). The distance between the quintets is relatively large, i.e. $Te^{(1)}$ - $Te^{(1)}$ bond is very weak.

The most probable places for accumulation and nucleation of nanoparticles based on Zn , Cr , Fe can be Te vacancies, sets of the type “dislocations-impurity atom”, the boundaries of blocks and grains, microcracks and concentration inhomogeneities [7-10].

Let us give the experimental data by the example of $Sb_2Te_3<Cr>$, $Bi_2Te_3<Cr>$, $Bi_2Se_3<Se>$. AFM images of nanoparticles formed on (0001) surface at chromium intercalation and synthesis of bismuth telluride together with Cr with subsequent crystallization are seen in Figs. 2 and 3. With intercalation at a temperature of 600 K chromium is introduced to the interlayers, like in nanoreactor interacting with superstoichiometric Sb_2Te_3 components: tellurium and antimony. This is testified by X-ray diffraction peaks from $CrSb$, $CrTe$ nanoparticles. X-ray diffraction patterns (Fig. 4) of intercalated $Sb_2Te_3<Cr>$ samples (obtained in the process of crystal growth) show peaks mainly from $CrSb$ nanoparticles at $2\Theta = 44^\circ$, 52° , 54° and 74° , and in $CrTe$ at $2\Theta = 54^\circ$ and the nanoislands of Sb_2Te_3 itself. Here, $T_e^{(1)}-T_e^{(1)}$ space serves not only as a nanoreactor, but as a nanocontainer for chromium (Fig. 4).

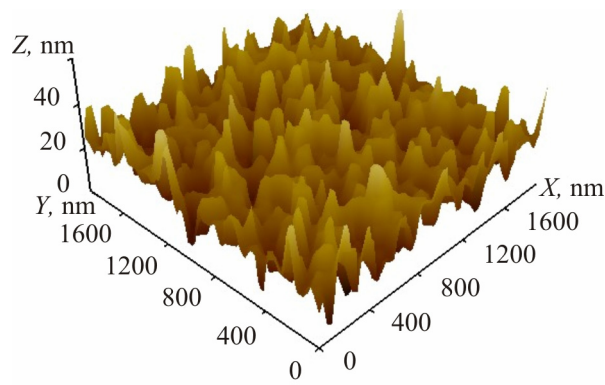


Fig. 2. 3D AFM image of (0001) surface of Cr-intercalated antimony telluride.

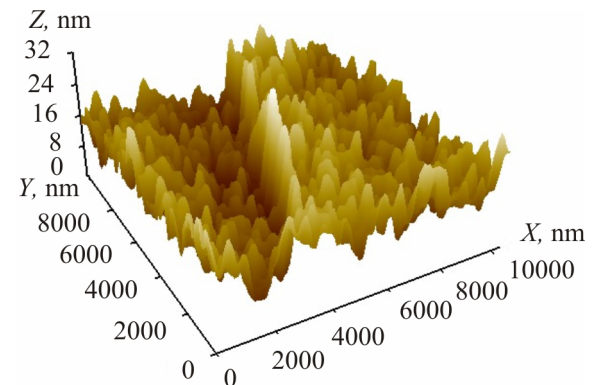


Fig. 3. 3D AFM image of (0001) surface of intercalated $Bi_2Te_3<Cr>$.

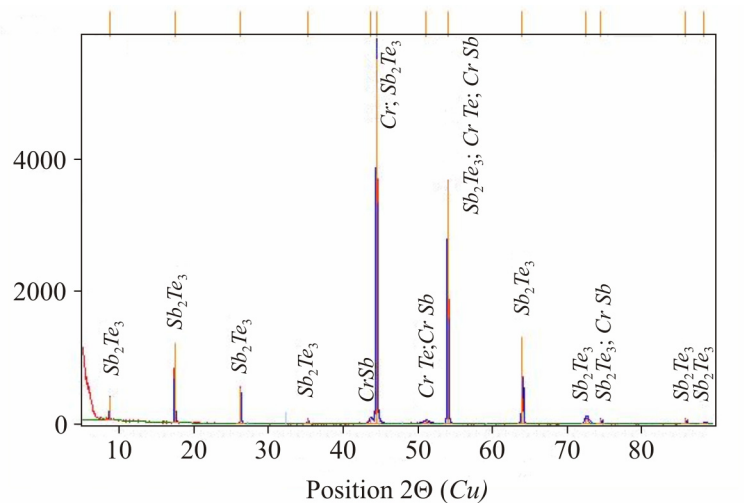


Fig. 4. X-ray diffraction image of (0001) surface of Cr doped $Sb_2Te_3<Cr>$.

Surface morphology of (0001) $Sb_2Te_3<Cr>$ in 3D scale with Cr intercalation is represented in Fig. 2; nanoislands here consist of $CrSb$, $CrTe$. Here one can observe traces of Cr and Sb_2Te_3 ; the height of nanoislands varies from 5 to 20 nm. AFM image of $Bi_2Te_3<Cr>$ shows nanoobjects of smaller size to 15 nm.

X-ray diffractometry for $Bi_2Te_3<Cr>$ is given in Fig. 5: here, $T_e^{(1)}-Te^{(1)}$ medium was a nanocontainer

for Cr : ($2\Theta = 43^\circ, 51^\circ$). X-ray diffraction images for $Bi_2Se_3<Se>$ are shown in Fig. 6, and for n -type $<ZnSe>$ solid solution in Fig. 7; X-ray diffraction peaks are mainly seen from $ZnSe$ at $2\Theta = 45^\circ, 73^\circ$ and 74° . In Bi_2Se_3 van der Waals gap serves not only as a nanocontainer, but also as a nanoreactor.

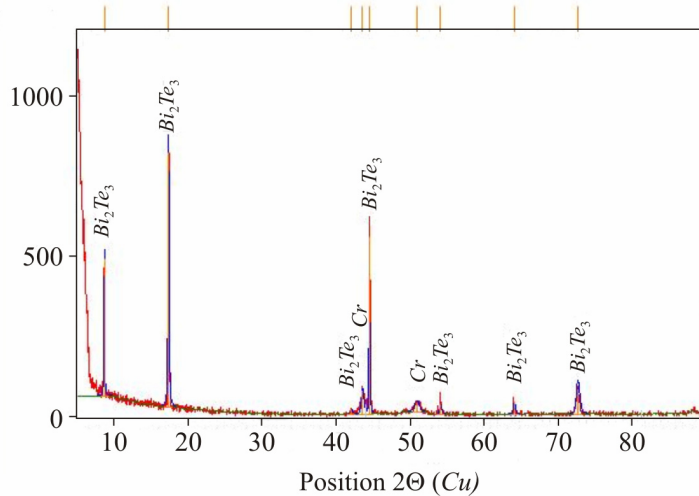


Fig. 5. 3D X-ray diffraction image of (0001) $Bi_2Te_3<Cr>$ surface.

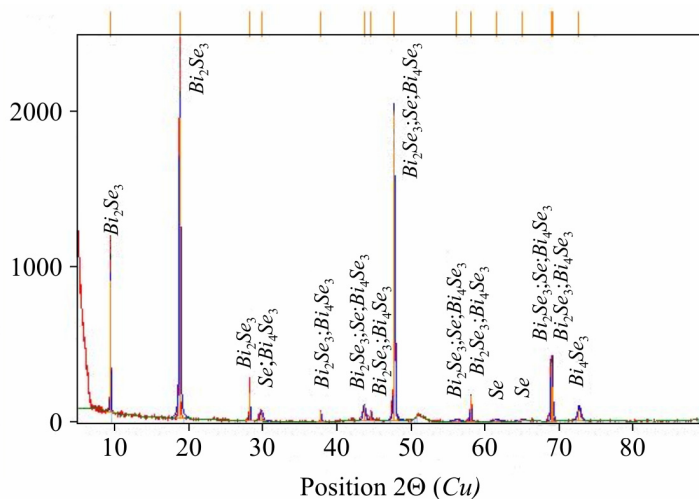


Fig. 6. X-ray diffraction image of fractal surfaces in $Bi_2Se_3<Se>$ system.

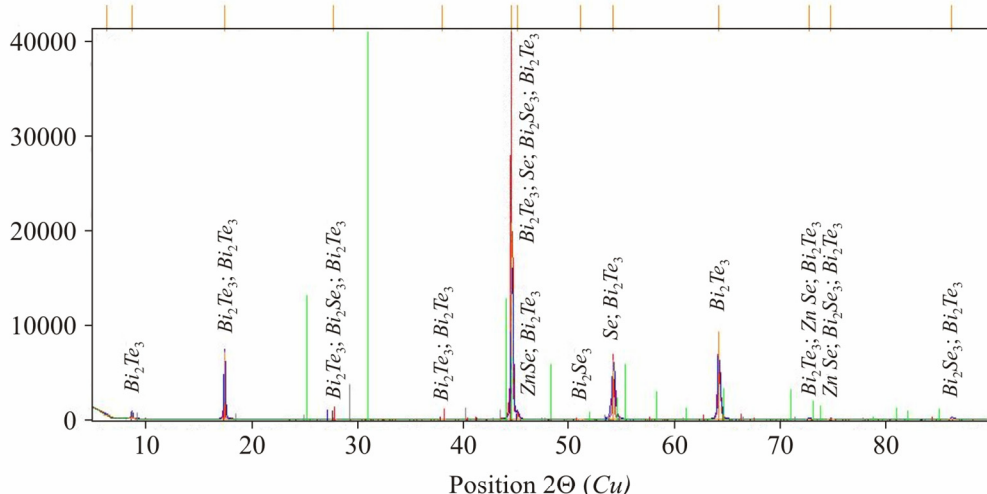


Fig. 7. X-ray diffraction image of (0001) in (Bi_2Se_3 4mol % - Bi_2Te_3 96 mol %) $<ZnSe>$ solid solution.

1.2. Mechanism of atoms diffusion and their aggregation

Supposed ways of particles diffusion and their aggregation with subsequent formation of nanoislands (Fig. 1) most probably are related to the process of filling with impurities of places around the dislocation wells and *Te* vacancies on the interlayer surface (0001) $A_2^V B_3^{VI}$. The onset of nanocells formation takes place in the process of impurities diffusion along the basis plane (0001) and their growth from the surface on *Te* vacancies and telluride quintets. Interacting and touching one another, nanoislands are formed on the basis plane (0001), which is evidently reflected on their topography. The process of coagulation reaches its peak whereby the nanoislands which are formed create a single nanofractal surface consisting of chromium which we observe in Fig. 3 for $Bi_2Te_3 < Cr >$ system.

Similar AFM surfaces between $T_e^{(1)}-T_e^{(1)}$ $A_2^V B_3^{VI}$ were obtained for $Bi_2Se_3 < Se >$ (see 8), as well as for solid solution (Bi_2Te_3 96 mol %- Bi_2Se_3 4 mol%) $< ZnSe >$ (Fig. 9).

Almost all steps of van der Waals zone filling are related to the process of quick introduction of easily diffusible impurities (*Zn*, *Cr* and *Se*) into $A_2^V B_3^{VI}$ along the basis plane as a result of diffusion directions (direction (a) in Fig. 1).

Nanoislands of fractal nature grow from nucleation center on telluride vacancies. Walking at random, *Zn*, *Cr* atoms move along the basis plane (0001) as a result of gradient diffusion. Contacting with the nucleus of a primary island, moving impurity atoms adhere to it. Then from a new point in the space between $T_e^{(1)}-T_e^{(1)}$ another atom starts to move, randomly walking and again contacting with another nanoobject, increasing its size.

The size of interlayer space $T_e^{(1)}-T_e^{(1)}$ in $Bi_2Te_3 \sim 3$ nm, the height of nanoparticles varies within 10 to 20 nm. Here, reversible compression or tension of quintets is also possible. The distance $T_e^{(1)}-T_e^{(1)}$ can be smoothly controlled, tuning the nanoreactor under study for given volume by filling with impurities the interlayer space.

Nanoobjects in the studied systems were self-organized, and in (Bi_2Te_3 - Bi_2Se_3) $< ZnSe >$ solid solution they were accompanied by association of particles of close dimensions (for instance, Bi_2Se_3 , *Se*, Bi_2Te_3 and *ZnSe*) – Fig. 9.

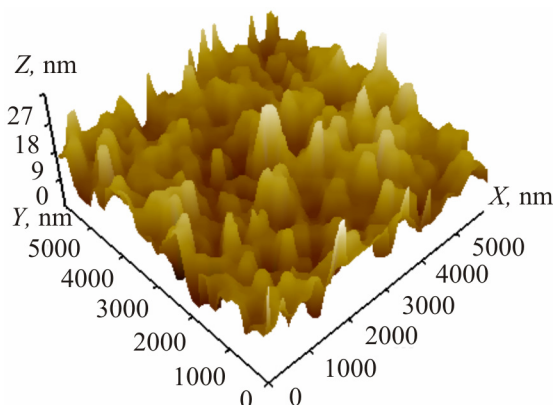


Fig. 8. 3D AFM image of (0001)
 $Bi_2Se_3 < Se >$ surface.

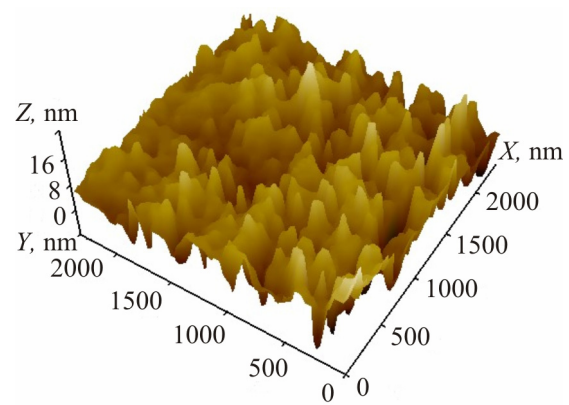


Fig. 9. 3D AFM image of (Bi_2Te_3 96 mol % – 4 mol %)
 $< ZnSe >$ solid solution surface.

According to the geometrical sign of dimensionality the resulting nanoobjects have nanosizes in all three directions: their height does not exceed 15 to 20 nm, their width and length vary within lower than 100 nm limits; i.e. in conformity with classification [2] these nanoobjects can be referred to nanoparticles with a disordered distribution. However, in (0001) surface morphology one can see nanoislands of smaller size ~ 5 to 10 nm that can be referred to clusters. As we see, nanoformations form a part of interlayer structure in doped $A_2^V B_3^{VI}$. In our opinion, they affect the anomalous Hall effect and

ferromagnetism in the systems that we investigated. We will now consider the physical characteristics of Sb_2Te_3 , Bi_2Te_3 and their solid solutions that are strongly affected by chromium atoms.

1.3. Thermoelectric figure of merit in solid solutions [8]

In *p*-type solid solutions based on bismuth and antimony chalcogenides p -(Bi , Sb)₂ (Te , Se)₃ the peculiarities of change in thermoelectric figure of merit (Z) were analyzed with regard to data obtained in the investigation of thermoelectric and galvanomagnetic properties. It is shown that in samples with optimal charge concentrations for the temperature range of 300 to 370 K in a multicomponent composition p - $Bi_{2-x}Sb_xTe_{3-y}Se_y$ ($x = 1.3$, $y = 0.06$) Z is determined by high mobility and low lattice thermal conductivity. Increase in the density of states effective mass and increase in the slopes of temperature dependence of mobility as compared to other compositions lead to Z increase in p - $Bi_2Sb_xTe_3$ solid solution at $x = 1.6$ in the temperature range of 370 – 550 K.

Increase in thermoelectric figure of merit in compositions under study is also determined by increase in compression of constant energy ellipsoids along the binary and bisector directions and by change in angle θ between the principal axes of ellipsoids and crystallographic axes [8].

The effect of suppression of intrinsic conduction in a narrow-gap semiconductor p - $Bi_{0.5}Sb_{1.5}Te_3$ by plastic deformation has been established. The effect becomes apparent in the attenuation of the Seebeck coefficient reduction at elevated temperatures due to intrinsic conduction. This effect can be caused by increased disorientation of crystal grains, formation of small-size nanoparticles leading to reduction of thermal conductivity and mobility of preferably interlayer charge carriers.

1.4. Anomalous Hall effect in $Sb_{2-x}Cr_xTe_3$

Layered semiconductor structures with nanoislands are characterized by a series of phenomena and properties that are of interest for the pursuance of the research and attractive in thermoelements.

Semiconductors of Sb_2Te_3 type have a rhombohedral structure (space group of symmetry $R\bar{3}m - D_{3d}^5$) with dyad axes C_2 and triad axes C_3 . Sb_2Te_3 crystals are always *p*-type due to high concentration of point charged defects of preferably anti-structural type, that is, antimony atoms occupy tellurium positions. The reason for such defects formation is a weak polarity of Sb - Te bonds. At liquid helium temperature the observed negative magnetoresistance and anomalous Hall effect, in our opinion, are related to the influence of nanoparticles formed in the medium of $Te^{(1)}\text{-}Te^{(1)}A_2^VB_3^{VI}$ (see Fig. 2).

The Hall coefficient in all the samples is positive and increases with increasing chromium content, which points to holes concentration reduction. However, it does not seem possible to use it for the calculation of holes concentration, since in bismuth and antimony tellurides there are two groups of holes with different concentrations and mobilities that are unknown.

Thus, we see that van der Waals gap is a peculiar kind of nanoreactor, where nucleation of quasi-two-dimensional layers with nanoislands between $Te^{(1)}\text{-}Te^{(1)}$ takes place on the surface (0001) (Sb_2Te_3) Bi_2Te_3 <impurity>. These structural voids – nanoreactors – are filled with compounds whose further modification leads to formation of ($CrSb$) nanoparticles. Formed by $Te^{(1)}\text{-}Te^{(1)}$ cavities of layered crystals, nanoreactors open up wide opportunities for the design of nanocomposites with given thermoelectric properties.

Study of surface morphology of (0001) Sb_2Te_3 and its solid solution $Bi_{1.2}Sb_{4.8}Te_9$ < Te > by electron microscopy and *X*-ray diffractometry methods has shown that atoms which did not react with other elements can also settle in the van der Waals gap $Te^{(1)}\text{-}Te^{(1)}$ (see Fig. 3). Conditions of formation in the interlayers-nanoreactors lead to the emergence of small-size nanoparticles. However, these results call for further research that will be published in our subsequent publications.

Paper [11] presents analysis of problems and approaches to their solving for semiconductor nanostructures with quantum dots as applied to interlayer nanoobjects in hand, as well as our data on the uniformity of nanoislands in their ensemble on the van der Waals surface (0001) $A_2^{V_2}B_3^{VI_3}$ <impurity>. In a compact array of nanoislands the imposition of elastic strain fields is possible, which creates effects that cause changes in the electron properties of nanostructured crystals. Problems whose solution calls for further efforts can be listed as follows: first, enhancement of size uniformity of nanoobjects array (see Figs. 2, 3 and 8, 9) with retention of a single shape and their elemental composition; second, control of space arrangement (space-ordered arrays) suitable for getting maximum compact and sparse arrays; third, reduction of the density of extended (dislocations) and point defects. Of particular interest are nanoparticles of small size (≤ 100 nm) as artificial atoms with a small number of bound states characterized by the value of energy gap between discrete levels, assuring the operation of devices at temperatures 100 to 350 K.

Let us compare the ATM images that we obtained in Fig. 9 to investigations [12] in percolation cluster of ZnSe quantum dots as a fractal object.

Of big importance are the results of studying samples with ZnSe quantum dots with the density corresponding to percolation threshold of excitons and much in excess, when quantum dots form conglomerates [12]. For the first time, emission of excitons from the percolation cluster of bound quantum dots as a fractal object was discovered. Structural analysis of photoluminescence spectra of samples has shown that they are determined by the contribution of exciton states located in different structural elements of percolation cluster, such as backbone (spine), dead ends and internal voids. The resulting percolation cluster of bound particles assures spreading the wave function of carriers for a microscopic distance. Percolation cluster is based on the so-called geometric or quantum percolation.

Experiments on the conductivity of samples allow establishing the moment of emergence of a percolation cluster of bound metal particles, but they cannot yield any information on the structure of percolation cluster, i.e. on its backbone, dead ends and internal voids. Percolation cluster is known to be a fractal object, so it cannot be uniform and continuous. The resulting AFM images (Fig. 9) can be referred to percolation clusters obtained above the percolation threshold. Further studies will be required in order to obtain on Bi_2Te_3 surface nanoobjects of ZnSe with distribution density below the percolation threshold.

Conclusions

Analysis of surface morphology of (0001) Bi_2Te_3 <Cr, ZnSe> has shown that nanoparticles are formed between $T_e^{(1)}$ - $T_e^{(1)}$ layers both in nanoreactor and nanocontainer.

The reason for quick growth of nanofractal “islands” is apparently that ZnSe, Cr come from vacancies to telluride quintets.

Interlayer impurities interact with formation of nanofragments of CrSb, CrTe and ZnSe.

Thus, between $A_2^{V_2}B_3^{VI_3}$ quintets, nanoparticles of size 5 to 10 nm are self-organized in nanoreactor of only CrSb and ZnSe, and in Bi_2Se_3 <Se> system, in the interlayers, nanoparticles are self-organized of Bi_4Se_3 .

References

1. P.M. Tarasov, Thermoelectric, Galvanomagnetic and Magnetic Properties of Doped $(Bi_{1-x}Sb_x)_2Te_3$ Single Crystals, *Author's Abstract of PhD Thesis* (M.V. Lomonosov Moscow State University, 2009), p. 21.

2. Yu.D. Tretyakov, A.V. Lukashin, and A.A. Yeliseev, Synthesis of Functional Nanocomposites on the Basis of Solid-Phase Nanoreactors, *Russian Chemical Reviews* **73** (9), 974-998 (2004).
3. O. Rabin, P.R. Herz, S.B. Cronin, L. Lin, A.I. Akinwande, and M.S. Dresselhaus, *Mater. Res. Soc. Symp. Proc.* **637**, 4.7.1 (2001)
4. K. Aleskerov, S.Sh. Kakhramanov, E.M. Derun, M.G. Pishkin, and G. Kavei, Some Peculiarities of Nanoobjects Formations in the Interlayer Space of Bi_2Te_3 Type Crystals, *Azerbaijan J. of Physics* XII (4), 41-45 (2007).
5. B.M. Smirnov, *Physics of Fractal Clusters* (Moscow: Nauka, 1991), p. 134.
6. Jens Feder, *Fractals* (New York: Plenum Press, 1989), p. 250
7. I.V. Gasenkova, T.E. Svechnikova, Research on the Structure of Single Crystals of Solid Solutions Based on Bismuth Telluride, Proceedings of Interstate Workshop “Thermoelectrics and their Applications” (2002), pp. 145-150.
8. L.N. Lukyanova, V.A. Kutasov, P.P. Konstantinov, and V.V. Popov, Thermoelectric Figure of Merit in *p*-type Solid Solutions Based on Bismuth and Antimony Chalcogenides at Above Room Temperatures, *Physics of the Solid State* **52** (8), 1492-1497 (2010).
9. B.M. Goltsman, V.A. Kutasov, and L.N. Lukyanova, Suppression of intrinsic conduction in *p*- $Bi_{0.5}Sb_{1.5}Te_3$ under plastic deformation *Physics of the Solid State* **50** (2), 235-236 (2008).
10. V.A. Kulbachinsky, P.M. Tarasov, and E. Bryuk, Anomalous Hall Effect and Ferromagnetism in a New Dilute Magnetic Semiconductor $Sb_{2-x}Cr_xTe_3$, *Letters to JETP* **81** (7), 426-430 (2005).
11. A.V. Dvurechensky, A.I. Yakimov, Physical Effects and Technologies as the Basis of Semiconductor Nanostructures with Quantum Dots for IR Range, *Izvestiya: Physics* **73** (1), 71-75 (2009).
12. N.V. Bondar, M.S. Brodin, Photoluminescence and Exciton Energy in Percolation Cluster of $ZnSe$ Quantum Dots as the Fractal Object, *Semiconductors* **46** (5), 644-648 (2012).

Submitted 08.04.2013.

N.V. Morozova, I.V. Korobeynikov, K.V. Kurochka, V.V. Shchennikov

Institute of Metal Physics of RAS, Urals Division,
18, S. Kovalevskaya Str., Yekaterinburg, 620990, Russia

**HIGH-PRESSURE INVESTIGATIONS
OF MATERIALS SUFFERING ABRUPT JUMPS
OF THE SEEBECK EFFECT**

Semiconductor compounds based on HgTe, Si, Bi₂Te₃ and PbTe, etc. have been found to suffer abrupt jumps of the Seebeck effect with (or without) the inversion of its sign on exposure to high pressure up to 20 GPa. Possible reasons for the above anomalous behavior of the Seebeck effect have been considered based on the analysis of the electron band structure features, as well as the variation of the defect-impurity system for different kinds of materials.

Key words: Seebeck effect, high pressure, semiconductors

Introduction

High pressure generally produces a strong impact on materials, in particular, it may cause abrupt changes of thermoelectric power (the Seebeck effect, S) [1]. These peculiarities are suitable for application in various kinds of electronic devices. The purpose of the present work is searching for materials possessing the above drastic variations of the Seebeck effect, and revealing general reasons for such behavior.

Experimental details

The measurements of the Seebeck effect were carried out in high-pressure chamber of toroidal type with semispherical concave anvils made of tungsten-carbide hard alloy with a diameter of anvil top ~ 1 mm [2, 3]. Typical sample sizes were $\sim 200 \times 200 \times 250 \mu\text{m}^3$. The chamber was loaded in an automated high-pressure setup [4]. The pressure values were determined to an accuracy of $\sim 10\%$ from a calibration “stress-pressure” curve based on the known and well-detectable pressure-induced transitions in Bi , PbS , PbSe , CdSe , and other compounds [2]. The anvils were characterized by high electrical conductivity, and, therefore, were used as electrical outputs to a sample. In the thermopower measurements an upper anvil was heated [4]. The temperature difference along sample thickness (ΔT) was measured by thermocouples. Possible small contribution to the thermopower values from the anvils themselves was checked by measuring S of pure lead having the value of S close to zero ($S \approx -1.27 \mu\text{V/K}$) [2-4].

Results and Discussion

The abrupt jumps of S under pressure application were first observed in mercury chalcogenides HgX ($X = \text{Te}, \text{Se}$) in [1] during the pressure-induced phase transition from zinc blende to cinnabar structure near $\sim 0.8 - 1.6$ GPa corresponding to semimetal – wide-gap semiconductor transformation of electron band structure [5-7]. In the present work, some ternary HgX -based compounds as well as

other certain compounds have been examined in search of the above phenomena.

In $HgTe$ -based compounds the sign inversion of S has been also found both in the initial cubic lattice at low P (~ 0.5 GPa for $HgTe$), and in the semiconductor phase near $\sim 4 - 6$ GPa (Fig. 1) [1]. The inversion of S in the semimetal phase of $HgTe$ is probably due to electronic transition to gap-less state [8], while the inversion of S in semiconductor phase with cinnabar structure corresponds to the variation of the partial contributions of electrons σ_n and holes σ_p into total conductivity $\sigma = \sigma_n + \sigma_p$ from $\sigma_n/\sigma_p > 1$ to $\sigma_n/\sigma_p < 1$. The behavior of $S(P)$ can be described using Eq. 1 [9] for an intrinsic semiconductor:

$$S = -\frac{k}{|e|} \left[\frac{b-1}{b+1} \cdot \frac{E_g}{2kT} + \left(r_n + \frac{5}{2} \right) \frac{b}{b+1} - \left(r_p + \frac{5}{2} \right) \frac{1}{b+1} - \frac{3}{4} \ln \frac{m_p^*}{m_n^*} \right], \quad (1)$$

where k is the Boltzmann constant, e is the electron charge, $b = \sigma_n/\sigma_p$ is the ratio of partial conductivities of electrons and holes, E_g is energy gap, T is the temperature, r_n (r_p) and m_n^* (m_p^*) are the scattering parameter and density-of-state effective mass of electrons (holes), respectively.

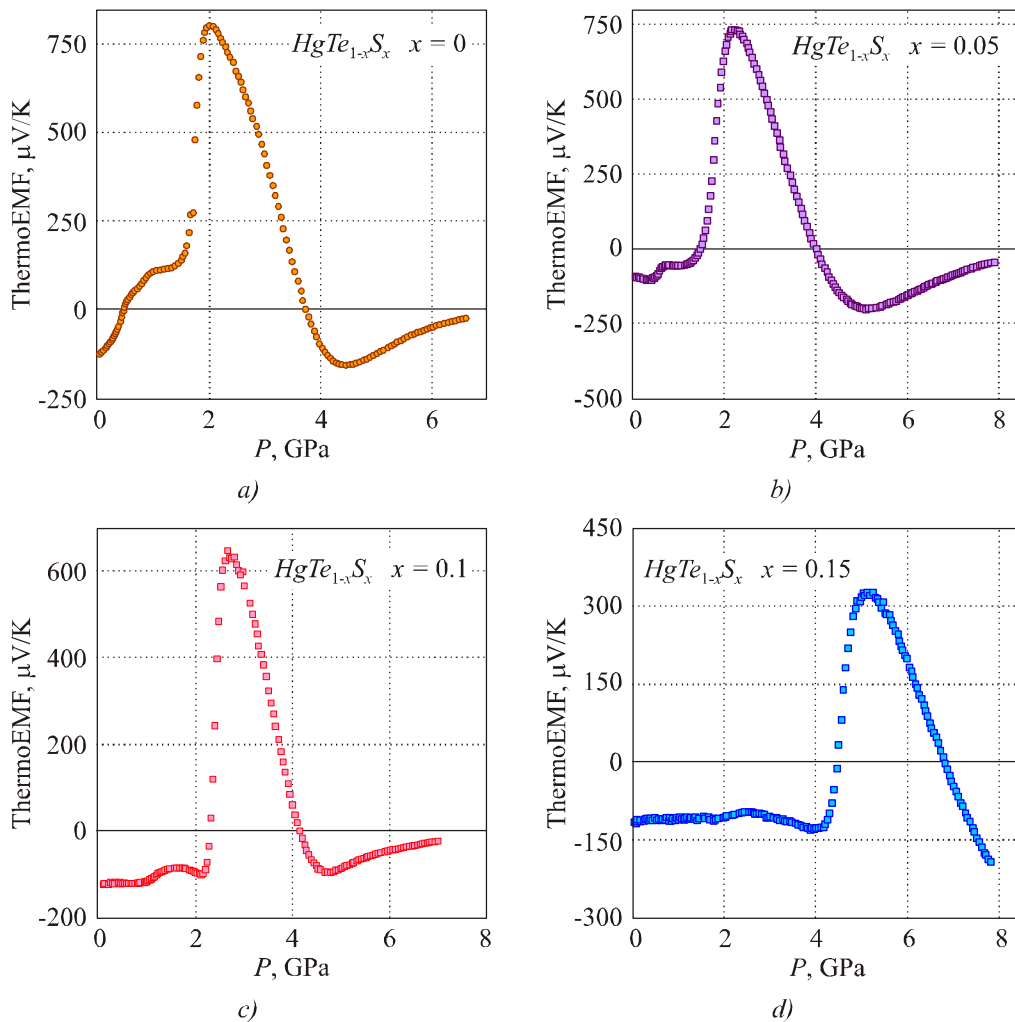


Fig. 1. Pressure dependences of thermoelectric power for $HgTe_{1-x}S_x$ crystals.

The opening of semiconductor gap E_g during semimetal-semiconductor phase transformation tends to an abrupt jump of S value, and change in the partial conductivity ratio σ_n/σ_p due to variation of parameters of the electron and hole bands under pressure, namely effective masses and mobilities

of electrons and holes, is the reason for S sign inversion. Both peculiarities are shifted toward higher pressures with increase in sulphur content (x) (Fig. 1). The high-pressure cinnabar phases of $HgTeS$ should be good thermoelectrics, similar to $HgTe$ [10, 11]. For $HgSe$ -based compounds only the first peculiarity of S (abrupt jump) is observed (Fig. 2). Similar behavior of $S(P)$ was also observed in many semiconductors at high pressures up to 30 GPa (PbX , $ZnTe$, $GaAs$ etc. [10]).

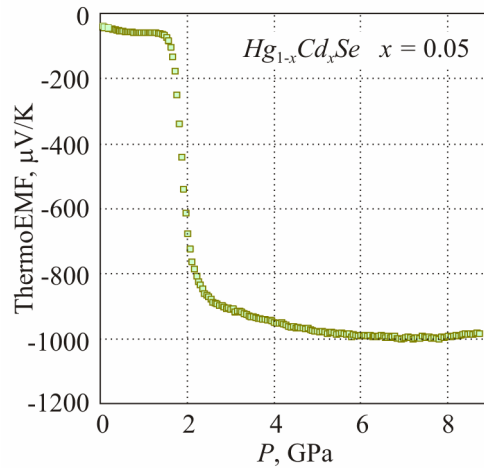


Fig. 2. Pressure dependence of thermoelectric power for $Hg_{1-x}Cd_xSe$.

In $Si_{1-x}Ge_x$ crystals ($x < 0.05$) the abrupt jumps of S with the sign inversion at moderate pressures [12] far from structural phase transitions can be also explained by Eq. 1 assuming the variation of the partial conductivity ratio due to changes in the “impurity-defect” system which tends to effective “doping” of materials. “Thermal donors” in Si are related to the interstitial oxygen atoms and structural defects and are known to be pressure dependent [13]. The variation of σ_p and σ_n in this case can be described by Eq. 2 and 3. for a doped semiconductor with two types of charge carriers [14]:

$$n = \frac{n_0}{2} + \left[\left(\frac{n_0}{2} \right)^2 + (4A_c A_v)^2 \exp\left(-\frac{E_g}{kT}\right) \right]^{1/2}, \quad (2)$$

$$p = -\frac{n_0}{2} + \left[\left(\frac{n_0}{2} \right)^2 + (4A_c A_v)^2 \exp\left(-\frac{E_g}{kT}\right) \right]^{1/2}. \quad (3)$$

Here, n_0 is the difference between the concentrations of donor and acceptor impurities; k is the Boltzmann constant, E_g is the semiconductor band gap; n and p are the concentrations of electrons and holes; A_c and A_v – are the densities of states in the electron and hole bands. The above change in the “impurity-defect” system leads to the sign inversion of n_0 and thus to the cardinal variation of σ_n/σ_p ratio from $\sigma_n/\sigma_p > 1$ to $\sigma_n/\sigma_p < 1$ (Fig. 3).

For Bi_2Te_3 – based compounds the topology of the Fermi surface occurs under doping because of the complex multi-band electron structure [15]. This topological transition can arise under pressure application [15] tending to the corresponding shift of the electron and hole bands and of the Fermi level position. Doping with In is known to enhance the anomalous behavior of S during the above transformation of electron structure under pressure [15], which becomes apparent in the abrupt jumps of $S(P)$ near ~ 1 GPa (Fig.4) [15].

At pressures $P \sim 3$ GPa another topological transition at Bi_2Te_3 occurs [15], causing the emergence of a peak on $S(P)$ curves for binary [15], as well as at ternary compounds based on Bi_2Te_3 (Fig. 4).

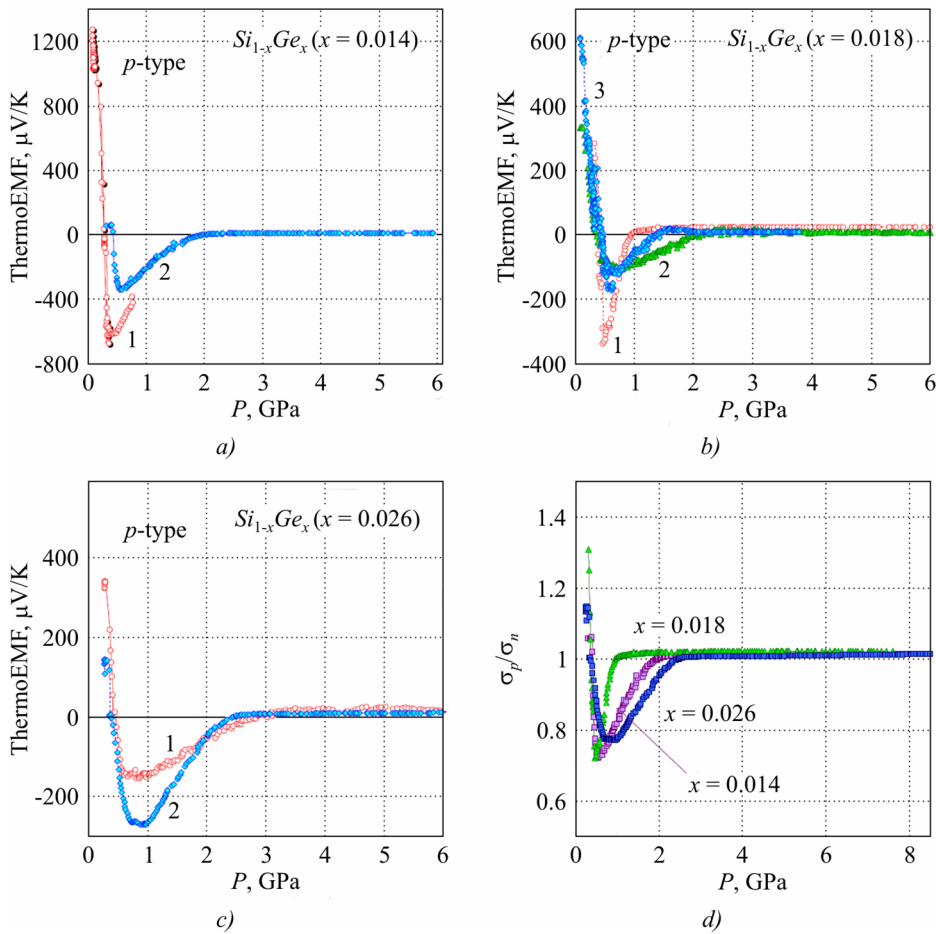


Fig. 3. Pressure dependence of thermoelectric power (a – c) and of hole-electron conductivity ratio (σ_p/σ_n) (d) for $Si_{1-x}Ge_x$ crystals. The figures mark the numbers of microsamples cut from the same $Si_{1-x}Ge_x$ crystal [12].

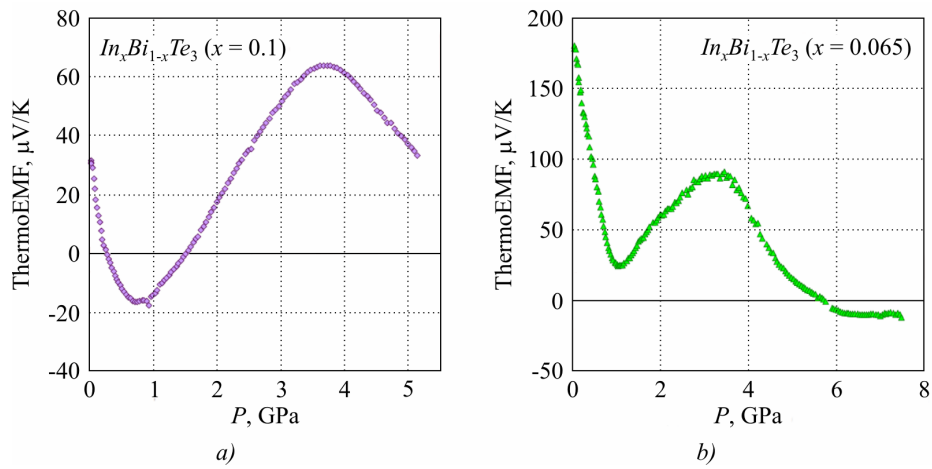


Fig. 4. Pressure dependences of thermoelectric power for $In_xBi_{1-x}Te_3$.

Conclusions

The abrupt jumps and the sign inversions of the Seebeck coefficient have been observed in some compounds under pressure. The main reasons for the above phenomena consist in the opening of semiconductor gap under phase transition and variation of either parameters of electron and hole bands, or the state of “defect-impurity” system under pressure tending to “doping” and compensation of electron (hole) contributions in conductivity. The change in the Fermi surface topology can also

produce the above effects. Certain phases and states arising under high pressure seem to be acceptable for thermoelectric applications [10, 11, 15, 16]. The experimental data of the present paper confirms the realization of the above mechanisms of S(P) variation for different kinds of compounds.

Acknowledgments. The work was done within RAS Program (Project no. 01.2.006 13394), by UD RAS as part of Program “Matter at high energy densities” of the Presidium of RAS (project 12-P-2-1004), by the Ministry of Education and Science of the Russian Federation (Contract 14.518.11.7020), and by the Oriented Basic Research Project of the Ural Branch of the Russian Academy of Sciences. The authors are grateful to Prof. V.A. Kulbachinskii, V.M. Frasunyak, N.V. Abrosimov and A. Misiuk for the samples given.

References

1. I.M. Tsidil'kovskii, V.V. Shchennikov, and N.G. Gluzman, Thermoelectric Power of Mercury Chalcogenides at Very High Pressures, *Semiconductors* **17** (5), 604-606 (1983).
2. V.V. Shchennikov, S.V. Ovsyannikov, and A.Y. Manakov, Measurement of Seebeck effect (Thermoelectric Power) at High Pressure up to 40 GPa, *J. Phys. Chem. Solids* **71**, 1168-1174 (2010).
3. S.V. Ovsyannikov, V.V. Shchennikov, M.A. Shvetsova, L.S. Dubrovinsky, and A. Polian, Tuning of the Stoichiometry of $Fe_{1-x}O$ Wüstite by Compression, *Phys. Rev. B* **81**, 060101 (2010).
4. V.V. Shchennikov, S.V. Ovsyannikov, A.Y. Derevskov, and V.V. Shchennikov, Jr., Automated Portable High-Pressure Setup for Study of Phase Transitions in Solids, *J. Phys. Chem. Solids* **67**, 2203-2209 (2006).
5. N.G. Gluzman, V.V. Shchennikov, Investigation of the High-Pressure Phase of $HgSe$, *Physics of the Solid State* **21** (10), 1844-1846 (1979).
6. V.V. Shchennikov, N.G. Gluzman, Pressure-Induced Zero-Gap Semiconductor-Finite-Gap-Metal Transitions in Mercury Telluride, *Physics of the Solid State* **23** (10), 1800-1803 (1981).
7. I.M. Tsidil'kovskii, V.V. Shchennikov, and N.G. Gluzman, Metallization of Mercury Chalcogenides under Ultrahigh Pressures, *Physics of the Solid State* **24** (9), 1507-1511 (1982).
8. V.V. Shchennikov, N.P. Gavaleshko, and V.M. Frasunyak, Phase Transition in $HgTeS$ Crystals at High Pressure, *Phys. Solid State* **37** (10), 1943-1946 (1995).
9. K. Seeger, *Semiconductor Physics* (Wien, NY, Springer, 1973), 514 p.
10. S.V. Ovsyannikov, V.V. Shchennikov, High-Pressure Routes in the Thermoelectricity or How One Can Improve a Performance of Thermoelectrics, *Chem. Mater.* **22** (3), 635-647 (2010).
11. X. Chen, Y. Wang, T. Cui, Y. Ma, G. Zou, and T. Iitaka, $HgTe$: A Potential Thermoelectric Material in the Cinnabar Phase, *J. Chem. Phys.* **128**, 194713 (2008).
12. I.V. Korobeinikov, N.V. Morozova, A. Misiuk, N.V. Abrosimov, V.V. Shchennikov, “Smart” Silicon: Switching Between *p*- and *n*-Conduction under Compression, *Appl. Phys. Lett.* **101** (6), 062107 (2012).
13. V.V. Shchennikov, Vs.V. Shchennikov, S.V. Streltsov, I.V. Korobeynikov, and S.V. Ovsyannikov, Thermoelectric Power of Different Phases and States of Silicon at High Pressure, *J. Electron. Mater.* 2013, DOI: 10.1007/s11664-013-2602-3.
14. W. Paul, D.M. Warshawer, *Solids under Pressure* (New York, McGraw-Hill, 1963), 524 p.
15. S.V. Ovsyannikov, V.V. Shchennikov, G.V. Vorontsov, A.Y. Manakov, A.Y. Likhacheva, and V.A. Kulbachinskii, Giant Improvement of Thermoelectric Power Factor of Bi_2Te_3 Under Pressure, *J. Appl. Phys.* **104**, 053713 (2008).
16. Y. Wang, X. Chen, T. Cui, Y. Niu, Y. Wang, M. Wang, Y. Ma, and G. Zou, Enhanced Thermoelectric Performance of $PbTe$ Within the Orthorhombic Pnma Phase, *Phys. Rev. B* **76**, 155127 (2007).

Submitted 28.05.2013.

**I.A. Drabkin¹, V.B. Osvenski¹, Yu.N. Parkhomenko¹, A.I. Sorokin¹,
G.I. Pivovarov², L.P. Bulat³**

¹State Scientific-Research and Design Institute of Rare-Metal Industry “Giredmet” JSC,
5/1, B. Tolmachevsky lane, Moscow, 119017, Russia;

²Technological Institute of Superhard and New Carbon Materials “Tisnum”,
7 a, Centralnaya Str., Troitsk, Moscow, 142190, Russia;

³The National Research University ITMO, 49, Kronverkskiy Ave.,
Saint-Petersburg, 197101, Russia

**ANISOTROPY OF THERMOELECTRIC PROPERTIES
OF P-TYPE NANOSTRUCTURED MATERIAL BASED
ON $(Bi, Sb)_2Te_3$**

Anisotropy of thermoelectric properties of nanostructured $Bi_{0.4}Sb_{1.6}Te_3$, material obtained by spark plasma sintering (SPS) method in the temperature range of 245 to 420 K has been investigated. It has been established that anisotropy value is increased with sintering pressure increase and temperature reduction. Electric conductivity anisotropy coefficient is higher than thermal conductivity anisotropy coefficient. Based on the experimental values of electric and thermal conductivity in different directions, texture coefficients in compacted material have been calculated. The resulting calculated temperature dependences of thermoEMF are in reasonable agreement with the experimental data. The results of calculation of temperature dependence of lattice thermal conductivity in perpendicular and parallel directions with respect to trigonal axis are given for a single-crystal grain in the extrinsic conduction region. Starting from some temperature depending on sample manufacturing conditions, the value of thermoelectric figure of merit ZT in a direction parallel to compaction axis, becomes higher than in a perpendicular direction, which is due to the emergence of minor carriers and the difference in the values of hole-electron mobility ratios in single-crystal material for parallel and perpendicular directions with respect to trigonal axis. Comparison of errors in determination of material thermoelectric parameters with Harman’s method and the method of separate measurement of electric conductivity, thermoEMF and thermal conductivity on different samples has been made. In the latter case measurement of electric and thermal conductivity without regard to anisotropy can yield overrated ZT values.

Key words: nanostructured material, anisotropy coefficient, electric conductivity, thermal conductivity.

Introduction

The Bi_2Te_3 compound and solid solutions on its basis possess a layered crystalline structure with monoatomic layers alternating as $Te^{(1)} - Bi - Te^{(2)} - Bi - Te^{(1)}$ in the c direction. These quintet layers are interconnected by weak Van der Waals bonds. Such anisotropic structure defines possible anisotropy of thermoelectric properties along and across the layers. In a bulk polycrystalline sample the anisotropy of properties is the stronger, the higher is texture degree, i.e. preferred crystallographic orientation of grains.

It is well known that single crystals and polycrystals obtained by methods of oriented

crystallization of the melt (for instance, zone melting) or extrusion, possess 100-percent or so texture and, as a consequence, pronounced anisotropy of thermoelectric properties. In polycrystalline material obtained by hot pressing of powders, the possibility of texture origination and anisotropy of thermoelectric properties increases with increasing grain size. Starting from work [1] where for the first time the bulk nanostructured material with high thermoelectric properties ($ZT = 1.4$) was obtained, it has been believed that samples with randomly oriented nanosize grains are isotropic. Therefore, in the majority of subsequent works that reported on obtaining *p*-type material with high ZT values the possibility of thermoelectric properties anisotropy was ignored.

However, a more thorough and purposeful investigation based on the measurement of thermoelectric properties in perpendicular and parallel directions with respect to compaction axis, revealed electric and thermal conductivity anisotropy of compacted material based on Bi_2Te_3 , including that produced from nanopowders. Anisotropy due to the presence of texture is more pronounced in *n*-type material [2].

Anisotropy value, characterized by anisotropy coefficient, depends on a combination of factors: solid solution composition [3], morphology of source powder particles [4], as well as compaction conditions, namely pressure and temperature. This accounts for a quantitative difference in anisotropy coefficients observed in the samples produced under different conditions.

In the present work, anisotropy of thermoelectric properties of *p*-type nanostructured $Bi_{0.4}Sb_{1.6}Te_3$ material obtained by spark plasma sintering (SPS) has been studied as a function of compaction temperature and pressure. Unlike the majority of works, electric conductivity, thermoEMF, thermal conductivity and thermoelectric figure of merit were determined by two methods: Harman's method of measurement on the same sample and method of separate measurement of electric conductivity, thermoEMF, thermal conductivity on different samples.

Experimental procedure

Nanostructured samples were obtained from nanopowders of synthesized material of given composition. As a source raw material, *Bi* (99.999), *Sb* (99.999), *Te* (99.999) was used. Synthesis was performed by direct alloying of components in sealed quartz ampoules. The resulting ingots were subject to mechano-activated treatment in protective atmosphere in high-energy planetary ball mill PM 400 (Retsch, Germany). Compact nanostructured material samples of composition $Bi_{0.4}Sb_{1.6}Te_3$ were obtained by SPS method in SPS-511S installation (SPS Syntex, Japan). This method offers a number of advantages over conventional hot-pressing technique [5]. Cold-pressed pellet, preliminarily produced from nanopowder, was transferred to SPS installation. All operations with nanopowder were carried out in a glove box in protective atmosphere with moisture content O_2 control. Concentration of O_2 was maintained below 10 ppm to prevent from powder oxidation.

Samples sintered in graphite mold were as thick as 3 to 10 mm with diameter 20 mm. Sintering was made at temperatures 450 and 500 °C under a pressure of 30 and 50 MPa during 5 minutes. From the resulting pellets on electric erosion cutting machine APTA-151 (Delta-Test, Russia) samples of different size were cut depending on the method of properties measurement.

Thermoelectric properties of the bulk nanostructured material were measured by two methods.

In the temperature range of 245 to 355 K measurements were made by six-wire Harman's method [6] on the samples of size $2.5 \times 2.5 \times 4$ mm³. The specific feature of this method is that thermoelectric figure of merit Z , thermoEMF α and electric conductivity σ are determined by direct measurement on the same sample, and thermal conductivity κ is calculated from the formula

$Z = \alpha^2 \sigma / \kappa$. In so doing, electric and thermal conductivity is measured in one direction, perpendicular or parallel to compaction axis.

Account of thermal losses due to heat fluxes through sample input leads and heat radiation from the sample and the leads allows reducing considerably the errors of Z measurement. The calculated values of proper corrections are given in [7]. The accuracy of Z determination by Harman's method is much higher as compared to separate measurement of α , σ and κ , since it is a quotient of electrical voltages obtained in the course of experiment. The advantage of Harman's method is independence of results on sample shape and possibility of measurements on small-size samples. The shortcoming of Harman's method is the presence of soldered electric contacts to sample which automatically adds contact resistances to sample resistance.

Measurements were made on automated bench (Giredmet, Russia) and installation DX-8080 (RMT, Russia). According to our estimates, with Harman's method the measurement errors are: thermoEMF $\pm 1.5\%$, electric conductivity $\pm 2\%$, thermoelectric figure of merit $\pm 3\%$, thermal conductivity determined by calculation $\pm 5\%$.

The temperature dependences of thermoelectric properties in the range of temperatures 300 to 420 K were also determined by separate measurement of electric conductivity, thermoEMF and thermal conductivity on different samples with subsequent calculation of thermoelectric figure of merit. Practically all the results reported in foreign works on thermoelectricity of recent years have been obtained by this method which employs standard equipment. Electric conductivity and thermoEMF were measured on ZEM 3 installation (Ulvac, Japan) on the samples of size $2.5 \times 2.5 \times 10 \text{ mm}^3$. Thermal conductivity was calculated by the formula $\kappa = D_t \times C_p \times d$, where D_t – temperature diffusivity, C_p – specific heat, d – density. Each of these parameters is measured on different samples, which increases the error in measuring κ and, hence, Z . Temperature diffusivity was measured by laser flash method on LFA 457 installation (Netzsch, Germany). Specific heat was measured by calorimetric method on the samples of size $0.7 \times 2 \times 4 \text{ mm}^3$ on DSC-404C installation (Netzsch, Germany). The density of samples was measured by Archimedes's method.

According to our estimates, with separate measurement of α , σ and κ , the errors are as follows: thermoEMF $\pm 7\%$, electric conductivity $\pm 4\%$, thermal conductivity $\pm 12\%$ (with regard to errors in measuring D_t , C_p and d), thermoelectric figure of merit – minimum $\pm 20\%$.

Note that with said method the relatively high error in measuring σ and α is primarily related to low accuracy of fixing the distance between thermocouples that simultaneously serve as probes. When measuring temperature diffusivity by nonstationary laser flash method it is not quite clear to which temperature one should compare the measured value, since heat wave, especially at the initial moment after heat pulse, propagates under conditions of strong overheat with respect to initial sample temperature. Besides, when measuring on samples pressed from powders with high anisotropy of thermal properties, heat wave propagates in conformity with local thermal resistance, rather than over the shortest distance. It may affect the time of heat wave propagation and the measured temperature diffusivity value.

Thus, the above measurement accuracies are permissible for studying temperature dependences of α , σ and κ , but give rather approximate estimate of thermoelectric figure of merit.

To determine anisotropy value of thermoelectric properties at different temperatures, measurements by both methods were performed in perpendicular and parallel directions with respect to sample compaction axis.

Experimental results and discussion

Compacted polycrystalline material formed by anisotropic crystals is locally inhomogeneous, since its constituent single-crystal grains are of different orientation. Any electrical measurement on such material will yield certain effective values of measured quantities. Anisotropy coefficient of the effective electric conductivity $K_{ep\sigma}$ in compacted material will be characterized by the ratio

$$K_{ep\sigma} = \frac{\sigma_{ep\perp}}{\sigma_{ep\parallel}}, \quad (1)$$

where $\sigma_{ep\parallel}$ – electric conductivity measured along compaction axis, and $\sigma_{ep\perp}$ – electric conductivity in a transverse direction. In a similar way, the anisotropy of effective thermal conductivity K_{epk} can be determined as the ratio of thermal conductivities along and across compaction axis.

Experimental values of electric conductivity and thermal conductivity anisotropy coefficients at room temperature for samples prepared under different SPS conditions are given in Table 1.

The emergence of electric conductivity and thermal conductivity anisotropy in pressed polycrystalline samples is naturally attributable to texture arising during compaction [3, 8]. The degree of texture increases with increase in pressure. However, with a rise in temperature as a result of recrystallization, texture becomes weaker, which leads to reduction of anisotropy coefficients.

Therefore, even in a relatively small range of change in SPS pressure and temperature, there is a tendency toward K_σ and K_k increase with pressure increase and temperature reduction. According to this, as follows from the results given in [3], in p-type samples produced by SPS method at 380 °C and pressure 50 MPa, at room temperature $K_\sigma = 1.36$, $K_k = 1.25$. In so doing, electric conductivity anisotropy is more pronounced than thermal conductivity anisotropy. This effect is particularly apparent in n-type Bi_2Te_3 material produced by SPS method, where electric resistance anisotropy at room temperature is from 1.4 [4] to 1.7 [2].

Table 1
Electric conductivity and thermal conductivity anisotropy coefficients measured by Harman's method in $Bi_{0.4}Sb_{1.6}Te_3$ samples at room temperature

SPS conditions			$K_{ep\sigma}$	t	K_{epk}	$n \times 10^{-19}, cm^{-3}$
Time, min	Pressure, MPa	Temperature, °C				
5	50	450	1.17 – 1.18	0.20 – 0.21	1.075 – 1.09	1.75
5	30	450	1.13 – 1.145	0.16 – 0.18	1.07 – 1.075	
5	50	500	1.12 – 1.13	0.15 – 0.16	1.05 – 1.07	
5	30	500	1.09 – 1.105	0.11 – 0.13	1.035 – 1.05	1.64

In single-crystal material there is electric conductivity anisotropy along trigonal axis $\sigma_{p\parallel}$ and in a perpendicular direction $\sigma_{p\perp}$. Let us denote electric conductivity anisotropy coefficient in a single crystal as $K_{p\sigma}$

$$K_{p\sigma} = \frac{\sigma_{p\perp}}{\sigma_{p\parallel}}. \quad (2)$$

For single crystals of composition $Bi_{0.4}Sb_{1.6}Te_3$ $K_{p\sigma} = 2.5$ [9]. If in compacted polycrystalline

material the distribution of grains orientation takes place completely at random, its properties are homogeneous in all directions. For such materials there are approximate formulae for the calculation of the effective values of electric conductivity, thermal conductivity and the Hall effect [10-13]. However, in the presence of texture in compacted material the anisotropy of electric conductivity effective values is created. For compacted material we will restrict ourselves to a linear approximation and assume

$$\sigma_{ep\perp} = \frac{2\sigma_{p\perp} + \sigma_{p\parallel}}{3} + t \frac{\sigma_{p\perp} - \sigma_{p\parallel}}{3}, \quad (3)$$

$$\sigma_{ep\parallel} = \frac{2\sigma_{p\perp} + \sigma_{p\parallel}}{3} - t \frac{2(\sigma_{p\perp} - \sigma_{p\parallel})}{3}, \quad (4)$$

where t – texture coefficient in a direction perpendicular to compaction axis. Multiplier 2 before $\sigma_{p\perp}$ is due to the fact that there are 2 perpendicular directions and one parallel.

In the absence of texture $t=0$ and $\sigma_{ep\perp} = \sigma_{ep\parallel} = \frac{2\sigma_{p\perp} + \sigma_{p\parallel}}{3}$. With a perfect texture (single crystal) $t=1$ and $\sigma_{ep\perp} = \sigma_{p\perp}$, and $\sigma_{ep\parallel} = \sigma_{p\parallel}$. In the absence of texture the difference between (3) or (4) and the expression for electric conductivity in the model of effective medium [11] is within the measurement accuracy and makes 3–4 % towards overrating of the effective values, i.e. is quite comparable to electric conductivity measurement error. Therefore, one can consider the expressions (3) and (4) suitable for the analysis of properties of compacted polycrystalline material with low texture coefficient values.

Electric conductivity anisotropy coefficient in compacted material is related to properties of single crystal by the ratios obtained from (3) and (4):

$$2\sigma_{ep\perp} + \sigma_{ep\parallel} = 2\sigma_{p\perp} + \sigma_{p\parallel} \quad (5)$$

and

$$\sigma_{ep\perp} - \sigma_{ep\parallel} = t(\sigma_{p\perp} - \sigma_{p\parallel}). \quad (6)$$

Dividing (6) by (5) and using designations (1) and (2) yields

$$t = \frac{(K_{ep\sigma} - 1)(2K_{p\sigma} + 1)}{(2K_{ep\sigma} + 1)(K_{p\sigma} - 1)}. \quad (7)$$

The values of texture coefficient calculated from (7) are listed in Table 1. Increase in pressure from 30 MPa to 50 MPa results in texture coefficient growth by about 0.03–0.04, and a rise in sintering temperature from 450 °C to 500 °C to the same increase of t .

In the model of effective medium the relation between charge carrier concentration and measured Hall coefficient R_{eH} is given by the expression [12]

$$R_{eH} = \frac{AB_{eH}}{nec}, \quad (8)$$

where n – charge carrier concentration, e – electron charge, c – light velocity, A – the Hall factor, B_{eH} – effective anisotropy factor. In the absence of texture the value of B_{eH} with regard to the values of effective masses can be approximately considered equal to 0.8 [14]. In a single crystal the difference

in anisotropy coefficients for the directions parallel and perpendicular to triad axis is 10 – 15 %. So, it should be expected that with low texture coefficients the difference in the effective anisotropy coefficients for different directions will be small and comparable to measurement error. Therefore, charge carrier concentration was determined from the Hall effect measured at temperature 77 K with regard to B_{eH} . In the process, the Hall factor A was considered equal to unity, since at this temperature and charge carrier concentration the degeneracy condition is observed. The values of hole concentration in the investigated samples are listed in Table 1.

Of particular interest is to study the temperature dependence of thermoelectric properties anisotropy. As an example, Fig. 1 shows measured by Harman's method temperature dependences of electric conductivity σ , thermoEMF α , thermal conductivity κ and thermoelectric figure of merit ZT for a sample obtained by SPS method at a pressure of 50 MPa and temperature 450 °C, as well as the respective temperature dependences of anisotropy coefficients.

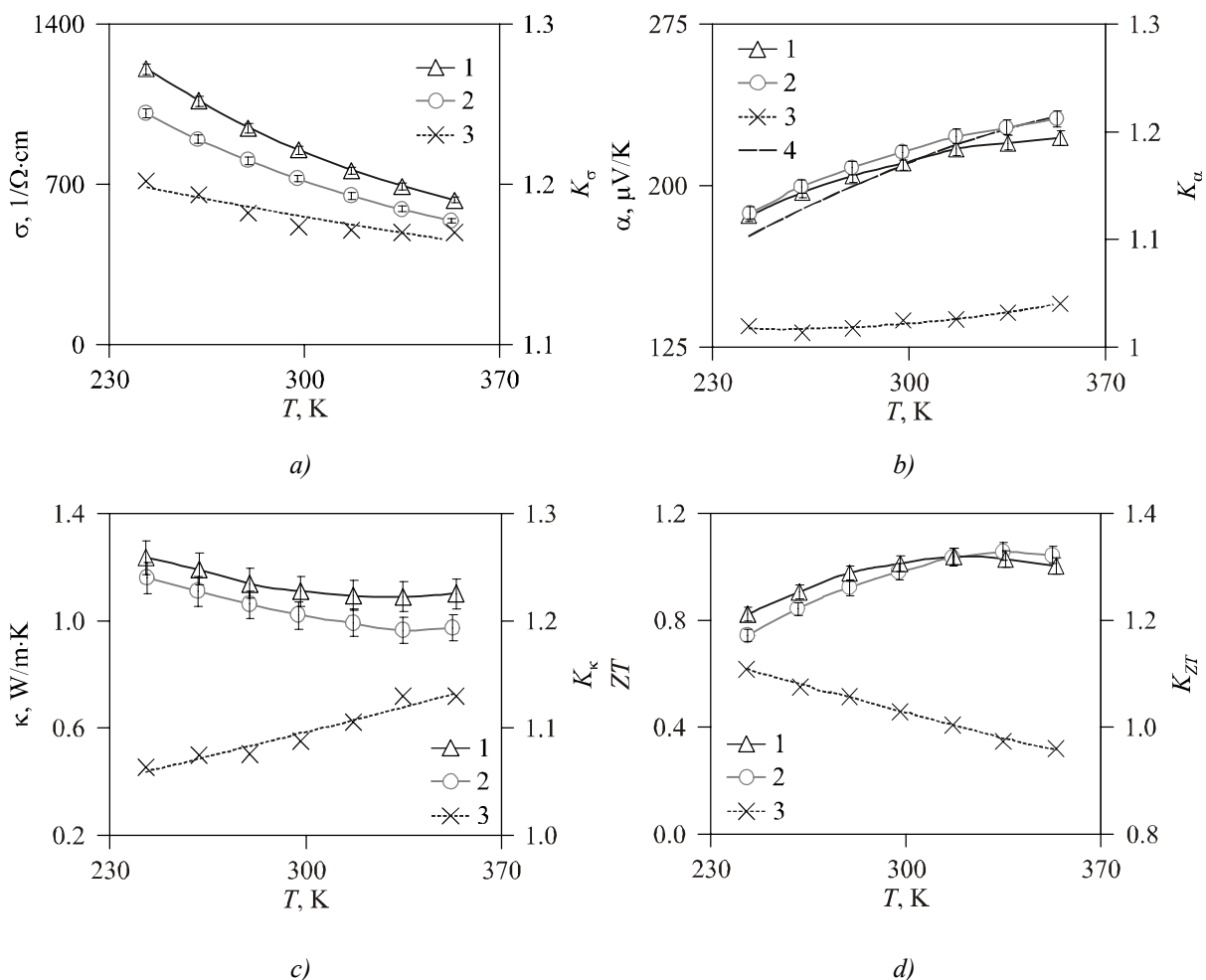


Fig. 1. Temperature dependences of electric conductivity (a), thermoEMF (b), thermal conductivity (c), dimensionless thermoelectric figure of merit (d) of $Bi_{0.4}Sb_{1.6}Te_3$, samples prepared by SPS method at a pressure of 50 MPa, temperature 450 °C.

Measurement by Harman's method: 1 – perpendicular to compaction axis, 2 – parallel to compaction axis, 3 – anisotropy coefficient, 4 – result of thermoEMF calculation.

The data on electric conductivity, the Hall effect and thermoEMF allow calculating with a knowledge of band parameters the temperature dependences of thermoelectric properties within the framework of parabolic bands and isotropic scattering of charge carriers. The difficulty of

calculation lies in a wide difference between the data on band parameters provided by different authors. Thus, according to [15], the density-of-state effective mass of holes m_p for composition $Bi_{0.45}Sb_{1.55}Te_3$ is $0.43m_e$, and according to [16] – $0.968 m_e$. In our calculation we considered scattering parameter $r = -0.5$, which corresponds to acoustic scattering of charge carriers. The density-of-state effective mass was chosen on condition of the best matching between calculated and experimental temperature dependences of thermoEMF. The ratio between hole and electron masses, between hole and electron mobilities, the energy gap width and coefficients of temperature dependence of the density-of-state effective masses and energy gap width were taken from [17]. Electron scattering parameter r was considered to be equal to hole scattering parameter. With regard to the above, the density-of-state mass of holes was $0.58(T/100)^{0.5}m_e$, the density-of-state mass of electrons was $0.5(T/100)^{0.35}m_e$.

The Fermi level was found from the solution of neutrality equation

$$n_p - n_n = n, \quad (9)$$

where n_p – hole concentration, n_n – electron concentration. ThermoEMF for single-crystal grains was found from

$$\alpha_{n,p} = \frac{k}{e} \left[\frac{(2r+5)F_{r+3/2}(\mu_{n,p}^*)}{(2r+3)F_{r+1/2}(\mu_{n,p}^*)} - \mu_{n,p}^* \right], \quad (10)$$

where k – the Boltzmann constant, e – electron charge, r – scattering parameter, F_n – the Fermi integrals, $F_n(\mu^*) = \int_0^\infty \frac{x^n}{1 + \exp(x - \mu^*)} dx$, $\mu_{n,p}^*$ – reduced Fermi level for electrons and holes. Indexes n and p denote electron or hole component. In the accepted approximations, the hole and electron components of thermoEMF are isotropic, but total thermoEMF in the region of mixed conduction can be anisotropic. A relation between the effective values of thermoEMF in a compacted polycrystalline sample and in single-crystal grains in the framework of model (2) and (3) is given by the ratios

$$\alpha_{ep\perp} = \frac{\alpha_{p\perp}\sigma_{p\perp}(2+t) + \alpha_{p\parallel}\sigma_{p\parallel}(1-t)}{3\sigma_{ep\perp}}, \quad (11)$$

$$\alpha_{ep\parallel} = \frac{2\alpha_{p\perp}\sigma_{p\perp}(1-t) + \alpha_{p\parallel}\sigma_{p\parallel}(1+2t)}{3\sigma_{ep\parallel}}, \quad (12)$$

where $\alpha_{p\perp}$, $\alpha_{p\parallel}$ – thermoEMF values in individual grains.

The resulting calculated temperature dependences of thermoEMF are represented in Fig. 1 and testify to their reasonable agreement with the experimental data. In the investigated temperature range a divergence between calculated values $\alpha_{ep\perp}$ and $\alpha_{ep\parallel}$ appears only at temperatures above 350 °C and does not exceed 1–2 μV/K. Experimental data (Fig. 1) also testify to the presence of small thermoEMF anisotropy (about 2 %) in compacted samples. Its emergence can be related to the effect of charge carrier scattering anisotropy on the grain boundaries. Electric conductivity anisotropy in a single crystal is also related to anisotropy of charge carrier mean free paths $K_{p\sigma}$. With a motion of charge carriers in a single grain of polycrystalline material for a direction perpendicular to trigonal axis, the mean free path is larger than for a parallel direction. Therefore, scattering processes on the grain boundaries will be more pronounced for a direction perpendicular to trigonal axis, which in the

presence of texture will result in the effective thermoEMF anisotropy for compacted material. However, this effect per se is very small and cannot result in considerable change of electric conductivity value, so determination of t without regard to scattering on grain boundaries can be considered to be sufficiently correct.

Relations of the type (2) and (3), with replacement σ by κ are also true for thermal conductivity. Based on them, with regard to texture coefficient, determined from the results of electric conductivity measurement, one can calculate thermal conductivity, parallel and perpendicular to triad axis in a single-crystal grain. Knowledge of band structure parameters allows calculating the electron component of thermal conductivity κ_{el} by the formulae [17]

$$\kappa_{el} = T \left(\frac{k}{e} \right)^2 \left\{ A_n \sigma_n + A_p \sigma_p + \frac{\sigma_n \sigma_p}{\sigma_n + \sigma_p} \left[\delta_n + \delta_p + \frac{E_g}{kT} \right] \right\}, \quad (13)$$

$$A_{n,p} = \left[\frac{(r+7/2) F_{r+5/2}(\mu_{n,p}^*)}{(r+3/2) F_{r+1/2}(\mu_{n,p}^*)} - \frac{(r+5/2)^2 F_{r+3/2}^2(\mu_{n,p}^*)}{(r+3/2)^2 F_{r+1/2}^2(\mu_{n,p}^*)} \right], \quad (14)$$

$$\delta_{n,p} = \left[\frac{(r+5/2) F_{r+3/2}(\mu_{n,p}^*)}{(r+3/2) F_{r+1/2}(\mu_{n,p}^*)} \right], \quad (15)$$

where T – temperature, E_g – energy gap width, σ_n and σ_p are used to mean the respective values of electric conductivity in a direction perpendicular and parallel to trigonal axis [18]. The first two terms in braces (13) characterize the electron and hole contribution to thermal conductivity, the last term is a bipolar thermal conductivity.

To make full calculation of thermal conductivity, as it was done for thermoEMF, does not seem possible due to absence of data on the lattice thermal conductivity for single crystals of given composition. Therefore, one can only calculate the lattice thermal conductivity in a single-crystal grain for extrinsic conductivity region, where electron contribution to thermal conductivity can be neglected. According to the results of calculation for a single grain, the lattice thermal conductivity parallel to trigonal axis has a conventional temperature dependence $\kappa_{L\parallel} \sim 1/T$, as illustrated in Fig. 2.

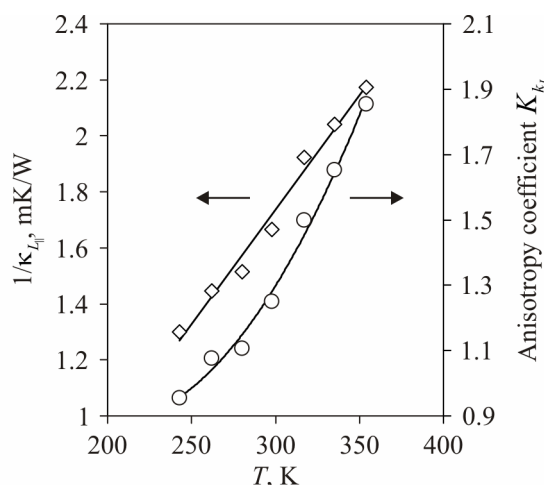


Fig. 2. Temperature dependence of lattice thermal conductivity in a single grain for a direction parallel to trigonal axis, and lattice conductivity anisotropy coefficient.

At the same time, the lattice thermal conductivity, perpendicular to trigonal axis, grows with a rise in temperature, as a result of which anisotropy coefficient $K_{k_L} = \kappa_{L\perp} / \kappa_{L\parallel}$ also grows with temperature (Fig. 2). Such a difference in thermal conductivity mechanisms along and across trigonal axis is hard to explain in the framework of scattering inside a grain. Most probably it is related not to intragranular properties, but to phonon scattering on grain boundaries. The mean free path of phonons inside a grain is larger for a direction perpendicular to trigonal axis. Therefore, for this direction scattering on grain boundaries will be more pronounced. With temperature reduction, the mean free path of phonons is increased and scattering on grain boundaries will be more pronounced, resulting in equalization of mean free paths (and, as a consequence, of thermal conductivity) along the directions parallel and perpendicular to triad axis.

Approximation of thermal conductivity anisotropy coefficient to electric conductivity anisotropy coefficient (Fig. 1) will contribute to Z increase with a rise in temperature, since in a polycrystalline sample it will reduce the eddy currents caused by different ways for heat flux and electric current.

From (9) it is seen that a crucial factor in bipolar thermal conductivity in *p*-type semiconductor at the initial stage, when $\sigma_p \gg \sigma_n$, is electron conductivity. In single-crystal material the ratio of electron and hole mobilities depends on crystallographic orientation. For a direction perpendicular to triad axis the bipolar thermal conductivity is higher than the respective value for a parallel direction. In compacted material with texture this yields that in a direction perpendicular to compaction axis thermal conductivity, with a rise in temperature, grows faster, as a result of which thermoelectric figure of merit drops faster than for a parallel direction. This accounts for intersection of thermoelectric figure of merit curves for parallel and perpendicular directions at temperatures close to 320 K (Fig. 1). Calculation of a bipolar thermal conductivity component shows that at a temperature of 415 K in a perpendicular direction $\kappa_{bip\perp} = 0.208 \text{ W/m}\cdot\text{K}$, and $\kappa_{bip\parallel} = 0.059 \text{ W/m}\cdot\text{K}$.

The above regularities of influence of SPS conditions on the anisotropy of thermoelectric properties are also observed with separate measurement of σ , α , κ . Fig. 3 represents the temperature dependences of thermoelectric properties measured by this method and the respective anisotropy coefficients for samples obtained by SPS method at a pressure of 30 MPa and 500 °C.

For SPS conditions 30 MPa and 500 °C at room temperature (~ 297 K), $K_{ep\sigma}$ and $K_{ep\kappa}$ are lower than in the samples obtained at 50 MPa and 450 °C (Fig. 1). The observed difference in temperatures corresponding to maximum ZT and intersection of curves $ZT\perp$ and $ZT\parallel$, in Figs. 1 and 3, is also apparently related to the difference in sample sintering conditions. At the same time, it should be noted that, as is evident from Fig. 3, when measuring D_t by laser flash method the differences in the values $\kappa_{e\perp}$ and $\kappa_{e\parallel}$ and appropriately calculated $ZT\perp$ and $ZT\parallel$ are within the accuracy of experimental procedure.

In this connection, we draw attention to another important feature of temperature diffusivity measurement procedure with the use of the LFA installation. As mentioned above, in this case the measured samples shaped as thin plates should have dimensions $10 \times 10 \text{ mm}^2$ or diameter 12 mm, and measurement is performed in a direction perpendicular to the surface of samples. In the majority of cases, including the works reporting very high values of $ZT > 1.3$, hot-pressed or spark plasma sintered samples shaped as pellets 2 – 3 mm thick are employed. Of such pellets one can cut out samples of necessary size for measuring D_t only perpendicular to compaction axis, and perform measurements along the compaction axis. This brings about a situation when $\kappa_{e\parallel}$ and $\sigma_{e\perp}$, $\alpha_{e\perp}$ are measured in different directions, which results in considerable overrating of thermoelectric figure of merit value.

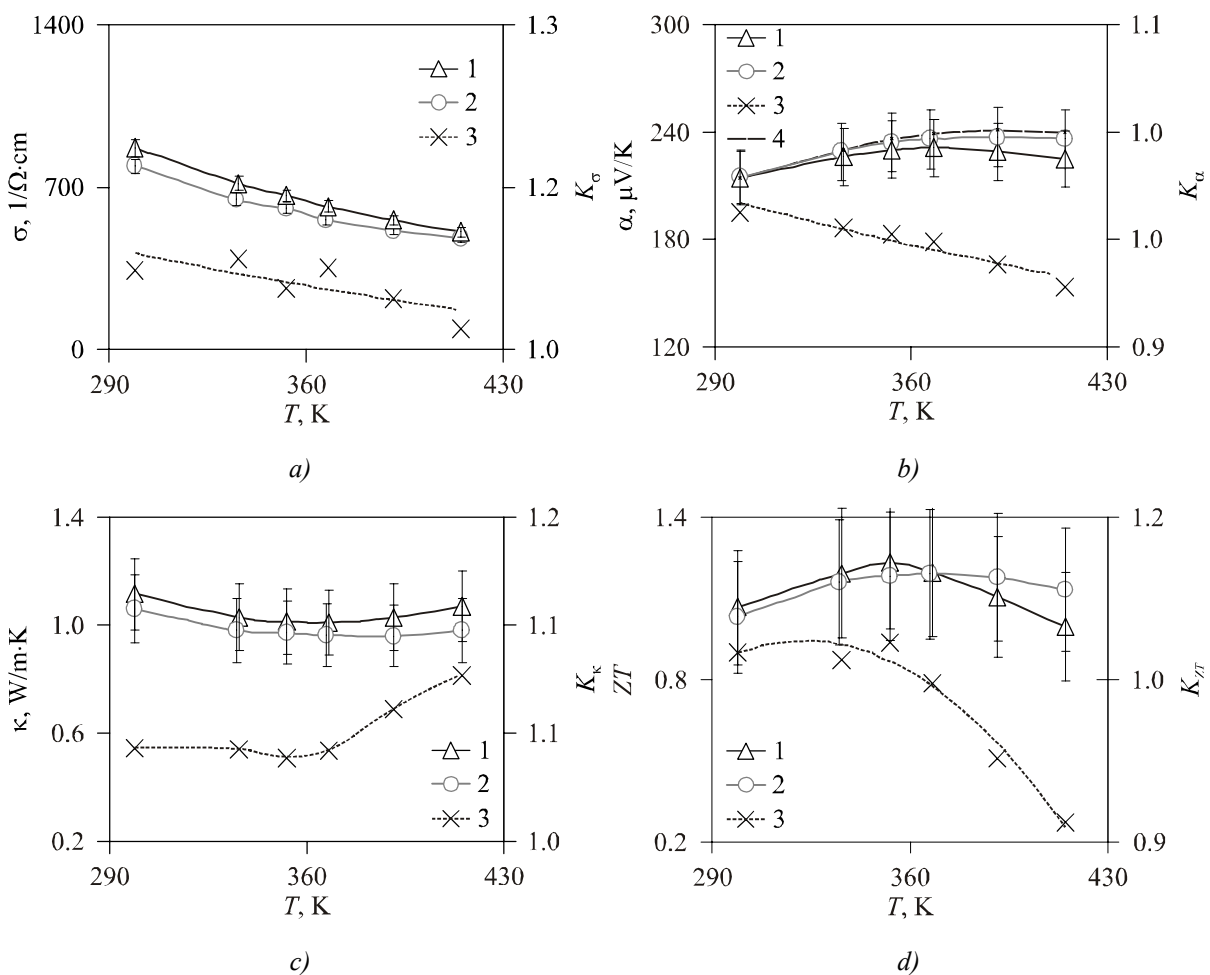


Fig. 3. Temperature dependences of electric conductivity (a), thermoEMF (b), thermal conductivity (c), dimensionless thermoelectric figure of merit (d) of $Bi_{0.4}Sb_{1.6}Te_3$, samples obtained by SPS method at a pressure of 30 MPa, temperature 500 °C.

Method of separate measurement: 1 – perpendicular to compaction axis, 2 – parallel to compaction axis, 3 – anisotropy coefficient, 4 – results of thermoEMF calculation.

For instance, in [3], where for a textured pellet 13 mm thick, obtained by SPS method in the mode of 50 MPa, 380 °C, when σ_\perp and κ_\parallel are measured in different directions, $ZT \sim 1.7$, and when $\sigma_{e\perp}$ and $\kappa_{e\perp}$ are measured in the same direction, $ZT \sim 1.1$.

Therefore, the values of $ZT > 1.3$ obtained on thin samples without regard to anisotropy give rise to doubt.

Conclusions

Anisotropy of thermoelectric properties of p-type nanostructured $Bi_{0.4}Sb_{1.6}Te_3$ material obtained by spark plasma sintering method (SPS) has been studied as a function of compaction pressure and temperature. Unlike the majority of works, the thermoelectric properties were determined both by Harman's method and the method of separate measurement of electric conductivity σ , thermoEMF α and thermal conductivity κ on different samples. In a direction perpendicular to compaction axis, σ_\perp and κ_\perp are higher than in a direction parallel to σ_\parallel and κ_\parallel . It has been established that electric conductivity anisotropy exceeds thermal conductivity anisotropy. The values of anisotropy

coefficients K_σ and K_κ increase with SPS pressure increase and temperature reduction. From the experimental values of electric and thermal conductivity in various directions coefficients of texture in compacted material have been calculated. The resulting calculated temperature dependences of thermoEMF are in reasonable agreement with the experimental data. For a single-crystal grain in the extrinsic conduction region the results of calculation of the temperature dependence of lattice thermal conductivity in perpendicular and parallel directions with respect to trigonal axis have been given. Starting from certain temperature depending on sample preparation conditions, the value of thermoelectric figure of merit ZT in a direction parallel to compaction axis becomes larger than in the perpendicular direction, which is due to the emergence of minor carriers and the difference in hole and electron mobility ratios in single-crystal material for directions parallel and perpendicular to trigonal axis. Comparison of the errors in determination of thermoelectric material parameters with Harman's method and the method of separate measurement of electric conductivity, thermoEMF and thermal conductivity on different samples has been made. In the latter case high values of $ZT > 1.3$ obtained on thin samples without regard to anisotropy, can be overrated due to specificity of temperature diffusivity measurement by laser flash method.

References

1. B. Poudel, Q. Hao, Y. Ma, X.Y. Lan, A. Minnich, B. Yu, X. Yan, D.Z. Wang, A. Muto, D. Vashaee, X.Y. Chen, J.M. Liu, M.S. Dresselhaus, G. Chen, and Z.F. Ren, High-Thermoelectric Performance of Nanostructured Bismuth Antimony Telluride Bulk Alloys, *Science* **320** (5876), 634 (2008).
2. Experimental Studies on Anisotropic Thermoelectric Properties and Structures of n -type $Bi_2Te_{2.7}Se_{0.3}$, *Nano Letters* **10**, 3373 (2010).
3. J. Shen, L.P. Hu, T.J. Zhu, and X.B. Zhao, The Texture Related Anisotropy of Thermoelectric Properties in Bismuth Telluride Based Polycrystalline Alloys, *Appl. Phys. Lett.* **99** (124102), 356 (2011).
4. D.H. Kim, C. Kim, S.H. Heo, and H. Kim, Influence of Powder Morphology on Thermoelectric Anisotropy of Spark-Plasma-Sintered Bi - Te -based Thermoelectric Materials, *ScienceDirect*. **59** (5), 405 (2011).
5. V.T. Bublik, D.I. Bogomolov, Z.M. Dashevsky et al., Comparison of Structure of Thermoelectric Material $Bi_{0.5}Sb_{1.6}Te_3$ Prepared by Hot Pressing and Spark Plasma Sintering Methods, *Izvestiya VUZov. Materialy Elektronnoi Tekhniki* **2**, 61 – 65 (2010).
6. V.N. Abrutin, I.A. Drabkin, I.I. Maronchuk, and V.B. Osvenski, Measurement of Thermoelectric Samples by Harman Method, IX Interstate Workshop Thermoelectrics and Their Applications (Saint-Petersburg, A.F.Ioffe FTI of RAS, 2004), P.303.
7. V. Abrutin, I. Drabkin, and V. Osvenski, Corrections Used when Measuring Thermoelectric Properties by Harman method, *Proc. 2nd Conference on Thermoelectrics* (Krakov, 2004), P.4.
8. W. Xie, J. He, S. Zhu, T. Holgate, S. Wang, X. Tang, Q. Zhang, and T. Tritt, Investigation of the Sintering Pressure and Thermal Conductivity Anisotropy of Melt-Spun Spark-Plasma-Sintered $(Bi, Sb)_2Te_3$ Thermoelectric Materials, *J. Mater. Res.* **26** (15), 2143 (2011).
9. O. Madelung, U. Rössler, and M. Schulz (ed.), Collaboration: Authors and editors. The Landolt-Börnstein Database, *Springer Materials* (<http://www.springermaterials.com>) **41C** (3), 17E-17F (1998).
10. V.I. Odelevsky, Calculation of Generalized Conductivity of Heterogeneous Mixtures, *Technical Physics* **21**, 1379 (1951).

11. D. Stroud, Generalized Effective Medium Theory for the Conductivity of an Inhomogeneous Medium, *Phys. Rev. B* **112** (8), 3368 (1975).
12. Xia Ting-Kang, D. Stroud, Theory of the Hall Coefficient of Polycrystals: Application to a Simple Model for $La_{2-x}M_xCuO_4$ ($M = Sr, Ba$), *Phys. Rev. B* **37** (1), 119 (1988).
13. G.N. Dulnev, Yu.P. Zarichniak, Thermal Conductivity of Mixtures and Composite Materials. Handbook (Leningrad: Energia, 1974), 264 p.
14. V.T. Bublik, Z.M. Dashevsky, I.A. Drabkin, et al., Transport Properties in the Temperature Range 190 – 300 K of Nanostructured p - $Bi_{0.5}Sb_{1.5}Te_3$ Prepared by Spark Plasma Sintering Technique (Saint-Petersburg, Thermoelectrics and Their Applications, 2010), 47 p.
15. L.N. Lukyanova, V.A. Kutasov, P.P. Konstantinov, and V.V. Popov, Thermoelectric Figure of merit in p -type Solid Solutions Based on Bismuth and Antimony Chalcogenides at Higher than Room Temperatures, *Physics of The Solid State* **52** (8), 1492 (2010).
16. M. Stordeur, M. Srölder, H. Sobottam, and V. Rieder, Investigation of the Valence Band Structure of Thermoelectric $(Bi_{1-x}Sb_xTe_3$ Single Crystals), *Phys. Stat. Sol. (b)* **150** (1), 150 (1988).
17. M.K. Zhitinskaya, V.I. Kaidanov, and V.P. Kondratyev, ThermoEMF Anisotropy in Bismuth Telluride Single Crystals, *Semiconductors* **10** (11), 2185 (1976).
18. I.A. Smirnov, V.I. Tamarchenko, *Electron Thermal Conductivity in Metals and Semiconductors* (Leningrad: Nauka, 1977), 151 p.

Submitted 22.04.2013.

I.V. Matsukevich, A.I. Klyndyuk



I.V. Matsukevich

Belarusian State Technological University,
13a, Sverdlov Str., Minsk, 220006, Republic Belarus



A.I. Klyndyuk

SYNTHESIS AND THERMOELECTRIC PROPERTIES OF $Ca_3Co_{3.85}M_{0.15}O_{9+\delta}$ ($M = V - Zn$) SOLID SOLUTIONS PREPARED BY CITRATE GEL METHOD

Citrate gel method was used to synthesize $Ca_3Co_{3.85}M_{0.15}O_{9+\delta}$ ($M = V - Zn$) solid solutions, to investigate their structure and microstructure, thermoEMF, electric conductivity and thermal expansion. Processes occurring in the preparation of $Ca_3Co_4O_{9+\delta}$ ceramics by citrate gel method were studied. It was established that the resulting materials are p-type semiconductors. The influence of partial substitution of cobalt cations by 3d-metal cations on the physical-chemical and thermoelectric properties of $Ca_3Co_{3.85}M_{0.15}O_{9+\delta}$ ceramics was analyzed. Maximum values of power factor are demonstrated by $Ca_3Co_{3.85}Fe_{0.15}O_{9+\delta}$ and $Ca_3Co_{3.85}Ni_{0.15}O_{9+\delta}$ solid solutions, namely 153 and 152 $\mu W/(m \cdot K^2)$ at 1100 K, which is a factor of 1.5 greater than for unsubstituted calcium cobaltite $Ca_3Co_4O_{9+\delta}$.

Key words: layered calcium cobaltite, citrate gel method, electric conductivity, thermoEMF, thermal expansion, power factor.

Introduction

A problem of scientific significance and practical importance lies in development of new thermoelectric materials efficient at elevated temperatures and resistant under these conditions to oxidation by atmospheric oxygen. Such properties are exhibited by layered calcium cobaltite $Ca_3Co_4O_{9+\delta}$ characterized by sufficiently high values of power factor and thermoelectric figure of merit at high temperatures [1, 2]. Functional characteristics of ceramics based on $Ca_3Co_4O_{9+\delta}$ can be improved using “soft”, low-temperature synthesis methods instead of solid-phase one [3-6], as well as through chemical modification of layered calcium cobaltite and, specifically, with a partial substitution of cobalt cations by 3d-metal cations [7-12].

In this work, $Ca_3Co_{3.85}M_{0.15}O_{9+\delta}$ ($M = 3d$ -metal) ceramics was prepared by citrate gel method, and influence of partial substitution of cobalt cations by 3d-metal cations on crystalline structure, thermal expansion, electrophysical and thermoelectric properties of $Ca_3Co_{3.85}M_{0.15}O_{9+\delta}$ phases was studied. It is shown that thermoelectric properties of layered calcium cobaltite are improved on introducing cobalt-substituting 3d-metal, and power factor attains its maximum value in the case of $Ca_3Co_{3.85}Fe_{0.15}O_{9+\delta}$ and $Ca_3Co_{3.85}Ni_{0.15}O_{9+\delta}$ solid solutions – 153 and 152 $\mu W/(m \cdot K^2)$, respectively, at 1100 K.

Experimental

For synthesis of $Ca_3Co_{3.85}M_{0.15}O_{9+\delta}$ ($M = V, Cr, Mn, Fe, Ni, Cu, Zn$) samples the following solutions were prepared: $Ca(NO_3)_2 \cdot 4H_2O$ (analytical grade) ($C_1 = 0.6\text{ M}$), $Co(NO_3)_2 \cdot 6H_2O$ (analytical

grade) ($C_2 = 0.8\text{ M}$), $Cr(NO_3)_3 \cdot 9H_2O$ (analytical grade), $Fe(NO_3)_3$ (chemically pure), $Ni(NO_3)_3 \cdot 6H_2O$ (analytical grade) (nitrate solutions of the rest of 3d-metals were prepared by dissolving oxides VO_2 (pure), Mn_2O_3 (pure), CuO (pure), ZnO (analytical grade) in concentrated nitric acid) ($C_3 = 0.8\text{ M}$) and $C_6H_8O_7$ (pure) ($C_4 = 0.5\text{ M}$), that were mixed in the ratios (of mole components) $3 : 3.85 : 0.15 : 15$. The resulting solutions were boiled out at 343 K to produce viscous violet gel which was dried at 383 to 393 K on electric stove to form a caramelized mass. The mass was crushed and further dried in a muffle furnace for 2 hours at 423 K with subsequent grinding. The resulting dirty pink powder was annealed for 4 hours at 873 K . The black powder obtained was thoroughly ground and pressed as pellets and bars that were further annealed for 5 hours at 1123 K with subsequent sintering for 8 hours at 1183 to 1193 K .

Samples identification and determination of their crystalline structure parameters was performed with the aid of X -ray phase analysis (X -ray diffractometer Bruker D8 XRD Advance, CuK_α -radiation, exposure range: $5 - 100^\circ 2\Theta$ with a step 0.05° , exposure conditions: $40\text{ kW}/40\text{ mA}$) and IR absorption spectroscopy (Nexus Fourier spectrometer by ThermoNicolet company, frequency range 300 to 1500 cm^{-1}). Index of oxygen nonstoichiometry (δ) in $Ca_3Co_{3.85}M_{0.15}O_{9+\delta}$ ($M = V - Zn$) was found using iodometric titration. The apparent density of samples (ρ_{exp}) was found by their mass and geometry.

Thermal analysis of precursor powder at synthesis of $Ca_3Co_4O_{9+\delta}$ by citrate gel method on drying at 403 K was performed using thermal analysis system Mettler Toledo (Switzerland) in the air in the temperature range of 298 to 1173 K at heating rate $10\text{ K}\cdot\text{min}^{-1}$.

The microstructure of sintered ceramics was studied through use of scanning electron microscope JSM-5610 LV with chemical analysis system EDX JED-2201 JEOL. Thermal expansion, electric conductivity and thermoEMF of sintered ceramic samples were studied in the air in the temperature range of 300 to 1100 K according to procedures described in [13-15]. The values of power factor (P) were calculated by the formula:

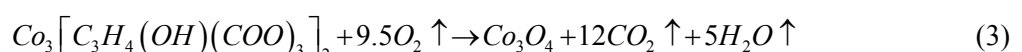
$$P = S^2 \cdot \sigma, \quad (1)$$

where S is thermoEMF, σ is electric conductivity.

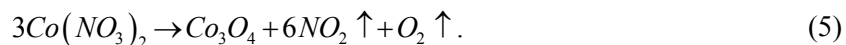
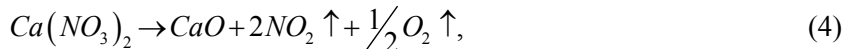
The values of apparent activation energy of electric conductivity E_A and linear thermal expansion coefficient α of samples were found from linear parts of dependences $\ln(\sigma \cdot T) = f(1/T)$ and $\Delta l/l_0 = f(T)$, respectively.

Discussion of results

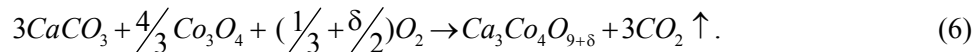
Decomposition of $Ca_3Co_4O_{9+\delta}$ precursor obtained by citrate gel method is a complicated procedure: TG curve in this case consists of eight parts (Fig. 1 a). During the first two process stages the loss of mass is $\approx 2.72\%$ ($298 < T < 373\text{ K}$) and $\approx 4.83\%$ ($373 < T < 539\text{ K}$), which corresponds to separation from the sample of free and bound water, respectively [4]. Reduction of powder mass during the third-sixth stages ($\approx 11.95\%$ at $539 < T < 576\text{ K}$, $\approx 6.03\%$ at $576 < T < 630\text{ K}$, $\approx 2.92\%$ at $630 < T < 688\text{ K}$ and $\approx 3.79\%$ at $688 < T < 851\text{ K}$) accompanied by pronounced exothermal effects with extremes at 588 , 599 and 687 K , occurs due to stepwise oxidation of calcium ($Ca_3[C_3H_4(OH)(COO)]_2$) and cobalt citrates ($Co_3[C_3H_4(OH)(COO)]_2$) to $CaCO_3$ and Co_3O_4 [4, 5] according to reactions



by atmospheric oxygen, as well as oxygen released at decomposition of calcium and cobalt nitrates:



The loss of mass during the seventh stage ($\approx 10.70\%$ at $851 < T < 1003$ K) is accompanied by fuzzy endothermic effect with extreme at 997 K and corresponds to calcium carbonate decomposition with formation of reaction product $\text{Ca}_3\text{Co}_4\text{O}_{9+\delta}$ [4, 5]:



Mass reduction during the eighth stage is not large ($\approx 0.39\%$ at $1003 < T < 1197$ K) and corresponds, apparently, to completion of $\text{Ca}_3\text{Co}_4\text{O}_{9+\delta}$ reaction formation.

Crystallites $\text{Ca}_3\text{Co}_4\text{O}_{9+\delta}$ had the shape of plates with the average dimensions $2.5 \times 1.7 \times 0.5$ μm ; in so doing, the plates were oriented with their broad side perpendicular to compaction axis (Fig. 1 b), which points to partial texturing of the obtained ceramics.

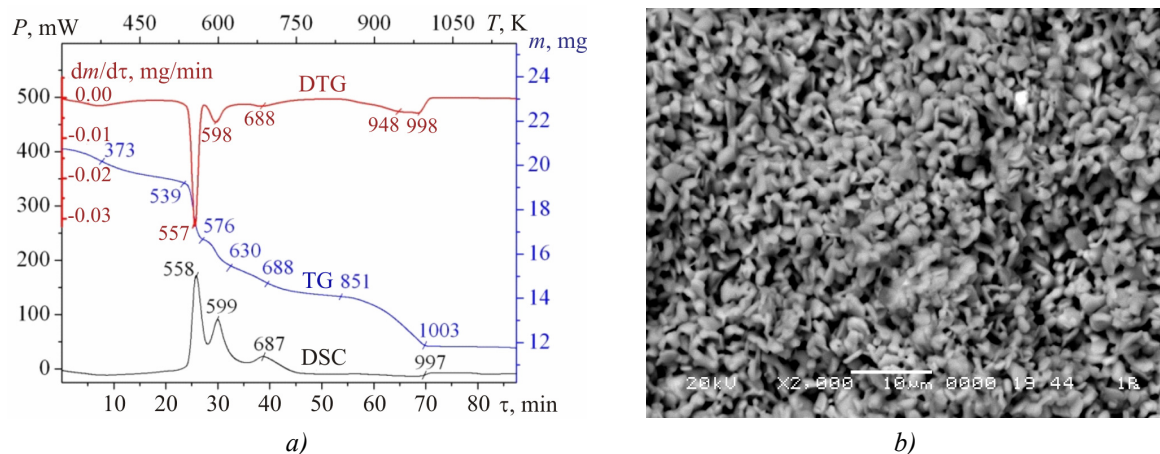


Fig. 1. Results of thermal analysis of $\text{Ca}_3\text{Co}_4\text{O}_{9+\delta}$ precursor (a) and micrograph of cleavage surface (perpendicular to compaction axis) of $\text{Ca}_3\text{Co}_4\text{O}_{9+\delta}$ ceramics (b) obtained by citrate gel method.

(DTG) differential thermogram, (TG) thermogram, (DSC) differential scanning calorimetry curve.

After the final synthesis stage, samples of calcium cobaltite $\text{Ca}_3\text{Co}_4\text{O}_{9+\delta}$ and $\text{Ca}_3\text{Co}_{3.85}\text{M}_{0.15}\text{O}_{9+\delta}$ ($M = V - \text{Zn}$) solid solutions were single-phase, within the accuracy of X-ray phase analysis, and had the structure of layered calcium cobaltite [16] (Fig. 2, curves 1 – 4). Parameter values of crystalline structure of $\text{Ca}_3\text{Co}_{3.85}\text{M}_{0.15}\text{O}_{9+\delta}$ phases are given in Table 1. Parameter values of unit cell $\text{Ca}_3\text{Co}_4\text{O}_{9+\delta}$ within the limits of claimed error coincide with the results [16] according to which for layered calcium cobaltite $a = 0.48376(7)$; $b_1 = 0.45565(6)$; $b_2 = 0.28189(4)$; $c = 1.0833(1)$ nm; $\beta = 98.06(1)^\circ$.

As is evident from the data represented in Table 1, the volume of unit cell and disproportion parameter (b_1/b_2) of $\text{Ca}_3\text{Co}_{3.85}\text{M}_{0.15}\text{O}_{9+\delta}$ solid solutions decrease from $M = V$ to $M = \text{Zn}$, which is mainly due to reduction of b_1 parameter of their crystalline structure.

IR absorption spectra of $\text{Ca}_3\text{Co}_{3.85}\text{M}_{0.15}\text{O}_{9+\delta}$ ($M = V - \text{Zn}$) powders comprised two distinct absorption bands with extremes at $\nu_1 = 563 - 573 \text{ cm}^{-1}$ and $\nu_2 = 726 - 733 \text{ cm}^{-1}$ (Fig. 2, curves 5 – 9), corresponding, according to [17], to valence vibrations of $\text{Co}(M) - \text{O}$ (ν_1) and $\text{Ca} - \text{O}$ (ν_2) bonds in the

structure of these oxides. The band ν_1 of $Ca_3Co_{3.85}M_{0.15}O_{9+\delta}$ solid solutions, as compared to unsubstituted phase $Ca_3Co_4O_{9+\delta}$, is displaced toward larger wave numbers, indicating to energy increase of cobalt-oxygen interactions in the structure of layered calcium cobaltite with partial substitution of cobalt cations by cations of other 3d-metals.

Table 1
*The values of crystalline structure parameters (a , b_1 , b_2 , c , β , V , b_1/b_2)
 and oxygen nonstoichiometry index (δ) of layered cobaltites $Ca_3Co_{3.85}M_{0.15}O_{9+\delta}$*

M	a , nm	b_1 , nm	b_2 , nm	c , nm	β , °	V , nm ³	b_1/b_2	δ
<i>V</i>	0.4839(7)	0.4591(7)	0.2837(9)	1.085(1)	98.23(6)	0.2386(9)	1.618	0.37
<i>Cr</i>	0.4838(7)	0.4595(8)	0.2841(9)	1.085(1)	98.20(7)	0.2387(9)	1.617	0.42
<i>Mn</i>	0.4830(6)	0.4561(7)	0.2819(9)	1.090(1)	98.26(8)	0.2377(9)	1.618	0.44
<i>Fe</i>	0.4868(5)	0.4557(5)	0.2843(6)	1.089(1)	100.3(1)	0.2378(6)	1.603	0.35
<i>Co</i>	0.4830(7)	0.4562(8)	0.2812(6)	1.085(1)	98.28(8)	0.2365(9)	1.622	0.35
<i>Ni</i>	0.4827(5)	0.4561(6)	0.2839(9)	1.084(1)	98.08(7)	0.2363(9)	1.607	0.35
<i>Cu</i>	0.4838(7)	0.4540(8)	0.2823(9)	1.081(1)	98.16(8)	0.2349(9)	1.608	0.55
<i>Zn</i>	0.4832(6)	0.4544(7)	0.2824(9)	1.083(1)	97.97(7)	0.2354(9)	1.609	0.48

The apparent density of $Ca_3Co_{3.85}M_{0.15}O_{9+\delta}$ solid solutions varied within 2.64 to 3.16 g/cm³ (Table 2) and was somewhat lower than that of basic calcium cobaltite (3.18 g/cm³), from which it can be concluded that partial substitution of cobalt by other 3d-metals impairs sintering behaviour of ceramics based on layered calcium cobaltite.

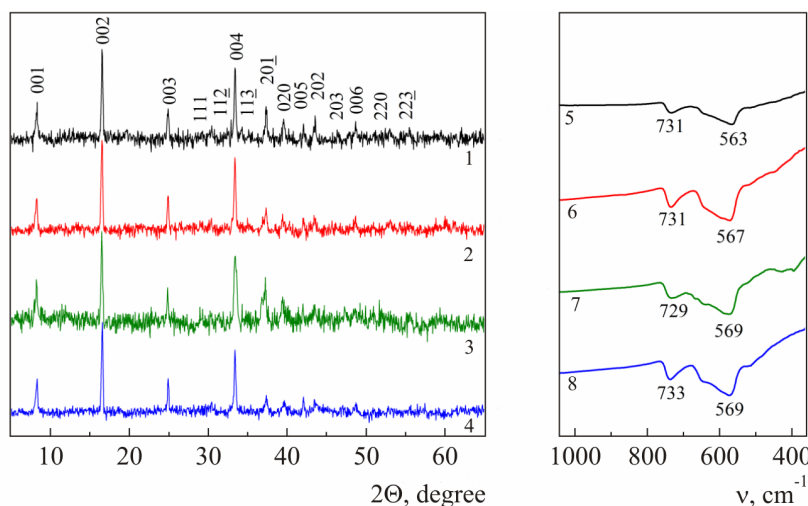


*Fig. 2. Powder diffraction patterns (1–4) (CuK_α -radiation) and IR absorption spectra (5–8)
 of $Ca_3Co_4O_{9+\delta}$ calcium cobaltite (1, 5) and solid solutions
 on its basis $Ca_3Co_{3.85}M_{0.15}O_{9+\delta}$: $M = Ni$ (2, 6), Fe (3, 7), Mn (4, 8).*

The temperature dependences of relative elongation of all investigated samples in the temperature range of 300 to 1100 K were linear, from which it follows that in this temperature range $Ca_3Co_{3.85}M_{0.15}O_{9+\delta}$ phases do not experience any structural phase transitions. The value of linear thermal

expansion coefficient of $\text{Ca}_3\text{Co}_{3.85}\text{M}_{0.15}\text{O}_{9+\delta}$ ($\text{M} = \text{V} - \text{Zn}$) oxides varied within $(1.20 - 1.31) \cdot 10^{-5} \text{ K}^{-1}$ (Table 2), and for all solid solutions (except for $\text{Ca}_3\text{Co}_{3.85}\text{Ni}_{0.15}\text{O}_{9+\delta}$ phase) it was lower than for basic calcium cobaltite. The dilatometry results are in good agreement with the data of IR absorption spectroscopy, according to which partial substitution of cobalt by other 3d-metals increases the energy of ionic interaction in the structure of $\text{Ca}_3\text{Co}_4\text{O}_{9+\delta}$ phase.

Table 2

The values of apparent density (ρ), linear thermal expansion coefficient (α), apparent electric conductivity activation energy (E_A), electric conductivity (σ_{1100}), Seebeck coefficient (S_{1100}) and power factor (P_{1100}) of $\text{Ca}_3\text{Co}_{3.85}\text{M}_{0.15}\text{O}_{9+\delta}$ ceramics

M	ρ , g/cm ³	$\alpha \cdot 10^5$, K ⁻¹	E_A , eV	σ_{1100} , S/cm	S_{1100} , $\mu\text{V/K}$	P_{1100} , $\mu\text{W}/(\text{m}\cdot\text{K}^2)$
<i>V</i>	3.02	1.22	0.075	21.7	229	114
<i>Cr</i>	2.86	1.25	0.099	13.7	242	79.8
<i>Mn</i>	2.64	1.21	0.075	7.73	278	59.8
<i>Fe</i>	3.09	1.20	0.068	23.1	258	153
<i>Co</i>	3.18	1.28	0.065	23.8	206	100
<i>Ni</i>	3.12	1.31	0.073	24.3	250	152
<i>Cu</i>	3.01	1.25	0.077	17.9	249	111
<i>Zn</i>	3.16	1.21	0.072	6.28	295	54.7

All materials investigated in this work were *p*-type semiconductors ($S > 0$, Fig. 3 *a, b*) whose conductivity in the temperature range of 800 to 1000 K varied from semiconductor to metal (Fig. 3 *a*), which is caused by partial reduction of samples due to partial oxygen release from their volume to the environment. The electric conductivity values of $\text{Ca}_3\text{Co}_{3.85}\text{M}_{0.15}\text{O}_{9+\delta}$ ($\text{M} = \text{V} - \text{Zn}$) solid solutions were, on the whole, lower, and the value of apparent electric conductivity activation energy was higher than for the unsubstituted phase (Table 2, Fig. 3 *a*).

ThermoEMF of investigated cobaltites increased with a rise in temperature (Fig. 3 *b*) and for $\text{Ca}_3\text{Co}_{3.85}\text{M}_{0.15}\text{O}_{9+\delta}$ ($\text{M} = \text{V} - \text{Zn}$) solid solutions it was higher than for $\text{Ca}_3\text{Co}_4\text{O}_{9+\delta}$ calcium cobaltite, the highest thermoEMF values being observed for $\text{Ca}_3\text{Co}_{3.85}\text{Mn}_{0.15}\text{O}_{9+\delta}$ and $\text{Ca}_3\text{Co}_{3.85}\text{Zn}_{0.15}\text{O}_{9+\delta}$ solid solutions (Table 2).

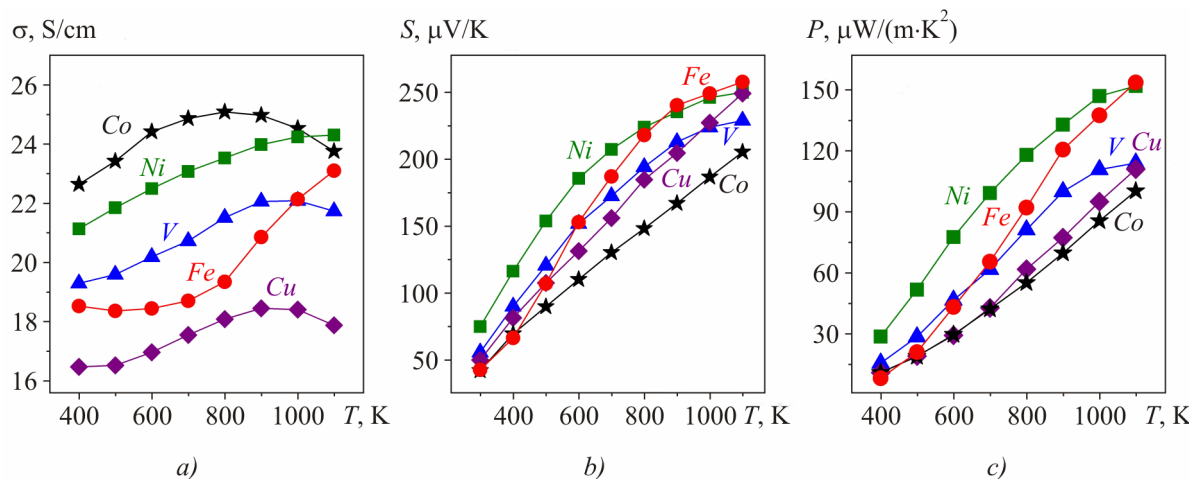


Fig. 3. Temperature dependences of electric conductivity σ (a), thermoEMF S (b) and power factor P (c) of $\text{Ca}_3\text{Co}_{3.85}\text{M}_{0.15}\text{O}_{9+\delta}$ ($\text{M} = \text{V}, \text{Fe}, \text{Co}, \text{Ni}, \text{Cu}$) ceramics.

The values of power factor of oxide ceramics increased with a rise in temperature and for $Ca_3Co_{3.85}M_{0.15}O_{9+\delta}$ solid solutions they were considerably higher than for the unsubstituted phase $Ca_3Co_4O_{9+\delta}$ (Fig. 3 c), with the highest P values demonstrated by $Ca_3Co_{3.85}Fe_{0.15}O_{9+\delta}$ and $Ca_3Co_{3.85}Ni_{0.15}O_{9+\delta}$ solid solutions, namely 153 and 152 $\mu\text{W}/(\text{m}\cdot\text{K}^2)$, respectively, at 1100 K, which is mainly due to high thermoEMF values of these oxides.

Conclusions

Citrate gel method was used to synthesize $Ca_3Co_{3.85}M_{0.15}O_{9+\delta}$ ($M = V - Zn$) oxide ceramics, to study its crystalline structure and microstructure and to investigate in the air at above room temperatures its thermal expansion, electrophysical and thermoelectric properties. Processes occurring in the preparation of calcium cobaltite by citrate gel method were studied. The values of linear thermal expansion coefficient of samples were calculated that made $(1.20 - 1.31) \cdot 10^{-5} \text{ K}^{-1}$. It was established that $Ca_3Co_{3.85}M_{0.15}O_{9+\delta}$ solid solutions are *p*-type semiconductors whose conductivity is lower and thermoEMF is higher as compared to basic calcium cobaltite $Ca_3Co_4O_{9+\delta}$. The highest values of power factor of the investigated compositions are possessed by $Ca_3Co_{3.85}Fe_{0.15}O_{9+\delta}$ and $Ca_3Co_{3.85}Ni_{0.15}O_{9+\delta}$ phases, namely 153 $\mu\text{W}/(\text{m}\cdot\text{K}^2)$ and 152 $\mu\text{W}/(\text{m}\cdot\text{K}^2)$, respectively, at a temperature of 1100 K.

Acknowledgements. The authors express gratitude to V.M. Kononovich for recording powder patterns, T.I. Barannikova for recording IR absorption spectra and V.G. Lugin for conducting electron microscopic studies. The work was performed in the framework of the state scientific research program “Functional and machine-building materials and technologies, nanomaterials and nanotechnologies in modern engineering”, subprogram “Crystal and molecular structures” (assignment 1.02).

References

1. *Oxide Thermoelectrics. Research Signpost*, Ed. by K. Koumoto, I. Terasak, and N. Murayama (Trivandrum, India, 2002), 255 p.
2. D. Kenfaui, D. Chateigner, M. Gomina and J.G. Noudem, Texture, Mechanical and Thermoelectric Properties of $Ca_3Co_4O_9$ Ceramics, *J. Alloys & Comp.* **490**, 472 (2010).
3. Y. Song, Q. Sun, L. Zhao, F. Wang, and Zh. Jiang, Synthesis and Thermoelectric Power Factor of $(Ca_{0.95}Bi_{0.05})_3Co_4O_9 / Ag$ Composites, *Mater. Chem. and Phys.* **113**, 645 (2009).
4. Y.F. Zhang, J.X. Zhang, Q.M. Lu, and Q.Y. Zhang, Synthesis and Characterization of $Ca_3Co_4O_{9+\delta}$ Nanoparticles by Citrate Sol-Gel Method, *Mater. Lett.* **60**, 2443 (2006).
5. N. Lerssongkram, S. Pinitsoontorn, and N. Keawprak, Synthesis and Thermoelectric Properties of $Ca_3Co_4O_9$ Prepared by Sol-Gel Method Using PVA, *KKU Research J.* **16** (1), 11 (2011).
6. T. Yin, D. Lui, Y. Ou, F. Ma, S. Xie, J.-F. Li, J. Li, Nanocrystalline Thermoelectric $Ca_3Co_4O_9$ Ceramics by Sol-Gel Based Electrospinning and Spark Plasma Sintering, *J. Phys. Chem. C* **114**, 10061 (2010).
7. Y. Wang, Y. Sui, X. Wang, W. Su and X. Lui, Enhanced High-Temperature Thermoelectric Characteristics of Transition Metals Doped $Ca_3Co_4O_{9+\delta}$, *J. Appl. Phys.* **107**, 033708 (2010).
8. Y. Wang, Y. Sui, P. Ren, L. Wang, X. Wang, W. Su, and H. Fan, Strongly Correlated Properties and Enhanced Thermoelectric Response in $Ca_3Co_{4-x}M_xO_{9+\delta}$ ($M = Fe$, Mn , and Cu), *Chem. Mater.* **22**, 1155 (2010).
9. Ch.-J. Liu, L.-Ch. Huang, and J.-Sh. Wang, Improvement of the Thermoelectric Characteristics of Fe -doped Misfit-Layered $Ca_3Co_{4-x}Fe_xO_{9+\delta}$ ($x = 0$, 0.05, 0.1, and 0.2), *Appl. Phys. Lett.* **89**, 204102 (2006).

10. Ch.-J. Liu, J.-L. Chen, L.-Ch. Huang, Zh.-R. Lin, and Ch.-L Chang, X-ray Absorption Spectroscopy Studies of *Fe*-doped Misfit-Layered $Ca_3Co_{4-x}Fe_xO_{9+\delta}$ ($x = 0, 0.05, 0.1$, and 0.2), *J. Appl. Phys.* **102**, 014908 (2007).
11. L. Xu, F. Li, and Y. Wang, High-Temperature Transport and Thermoelectric Properties of $Ca_3Co_{4-x}Ti_xO_{9+\delta}$, *J. Alloys & Comp.* **501**, 115 (2010).
12. T. Morimura, M. Hasaka, Sh.-I. Kondo, H. Nasashima, and H. Maeda, Microstructures and Thermoelectric Properties of Sintered $Ca_3Co_4O_9$ -based oxide, *J. Electr. Mat.* **41**, 1217 (2012).
13. A.I. Klyndyuk, E.A. Chizhova, Properties of Phases $RBaCuFeO_{5+\delta}$ (*R-Y, La, Pr, Nd, Sm-Lu*), *Inorganic Materials* **42** (5), 611 (2006).
14. A.I. Klyndyuk, E.A. Chizova, N.V. Sazanovich, and N.S. Krasutskaya, Thermoelectric Properties of Some Perovskite Oxides, *J. Thermoelectricity* **3**, 73 – 80 (2009).
15. A.K. Tripathi, H.B. Lal, Electrical Transport in Rare-Earth Orthochromites, *Mater. Res. Bull.* **15** (2), 233 (1980).
16. A.C. Masset, C. Michel, A. Maignan, M. Hervieu, O. Toulemonde, F. Studer, B. Raveau, J. Hejtmanek, Misfit-Layered Cobaltite with an Anisotropic Giant Magnetoresistance: $Ca_3Co_4O_9$, *Phys. Rev. B* **62** (1), 166 (2000-I).
17. Y. Zhang, J. Zhang, Rapid Reactive Synthesis and Sintering of Textured $Ca_3Co_4O_9$ Ceramics by Spark Plasma Sintering, *J. Mater. Proc. Technol.* **208**, 70 (2008).

Submitted 06.08.2012.

M.A. Korzhuev, T.E. Svechnikova

M.A. Korzhuev

A.A. Baikov Institute of Metallurgy and Material
Science of RAS, 49, Leninskiy Ave.,
Moscow, 119991, Russia



T.E. Svechnikova

**THERMODYNAMIC RESTRICTIONS FOR
THE NET POWER OF AUTOMOTIVE
THERMOELECTRIC GENERATORS AND
PROSPECTS OF THEIR USE IN TRANSPORT**

Experimental characteristics of automotive thermoelectric generators (ATEGs) placed on exhaust pipe (EP) are analyzed. It is shown that low net powers $W_e = 0.2 - 0.6 \text{ kW}$ and inefficient automotive waste heat recovery (WHR) using ATEG (total gain in car power $\Delta W \sim 0$) are related to the difficulties of heat exchange on the "exhaust gas (EG)/ ATEG" boundary. As a result, the specific power of ATEG also appears to be low $\tilde{W}^{\text{ATEG}} = W_e/m^{\text{ATEG}} \sim 20 - 30 \text{ W/kg}$ (here, m^{ATEG} is ATEG mass). Low values of W_e and \tilde{W}^{ATEG} are explained in the framework of A.S. Okhotin theory taking into account high thermal resistances of ATEG heat exchangers. It is shown that using A.F. Ioffe theory that does not take into account thermal resistances of heat exchangers, yields overestimated values of W_e , ΔW , \tilde{W}^{ATEG} and efficiency η^{ATEG} , and also the incorrect prediction of optimum energy gap E_g^{opt} of the leg materials. It is shown that the prospects of using high-power ATEGs in cars are essentially limited today. The ways for improvement of ATEG characteristics are discussed.

Key words: thermoelectricity, cars, waste heat recovery.

Introduction

At the present time, the world car park has exceeded ~ 1 billion units. As a result, cars have become the main pollutants of the Earth atmosphere by exhaust gases (EG) and waste heat [1]. Internal combustion engines (ICE) of modern cars have rather high efficiency $\eta^{\text{ICE}} \sim 0.4$ [2]. However, the major part of burning fuel power Q_0 and part of the net power of internal combustion engine $W^{\text{ICE}} = \eta^{\text{ICE}} Q_0$ are irretrievably lost through the exhaust pipe (EP) ($Q_0^{\text{EP}} \sim 0.3 Q_0$), cooling system (CS) ($Q_0^{\text{CS}} \sim 0.3 Q_0$), transmission and auxiliary mechanisms of a car (L) ($Q_0^L \sim 0.2 Q_0$) (Fig. 1 a). As a result, to overcome the motion resistance force of a car F_R , power consumption does not exceed $W_T^{\text{AUTO}} \sim \frac{1}{2} W^{\text{ICE}} \sim 0.2 Q_0$ [3, 4]. Hence, a need for waste heat recovery and fuel saving in cars [1, 4-6] is created. For these purposes, since the mid XX century in various countries automotive thermoelectric generators (ATEGs) have been developed, that are usually placed on the exhaust pipe of a car (Fig. 1 b) [3-12]. In this case, part of exhaust heat ($Q_0^{\text{ATEG}} < Q_0^{\text{EP}}$) is taken away to ATEG input and converted into net electric power $W_e = \eta^{\text{ATEG}} Q_0^{\text{ATEG}}$ via the Seebeck effect. (Here η^{ATEG} and Q_0^{ATEG} are the efficiency and thermal flux power at ATEG input) (Fig. 1 b) [1, 2]. As a result, on condition of $V_0 = \text{const}$, car power will increase by the value $\Delta W = W_e$, and the relative fuel consumption will be reduced accordingly $\delta A = \Delta A/A \sim -\Delta W/0.2 Q_0 < 0$ (Here A is the initial fuel consumption by a car, ΔA is its change after installation of ATEG, V_0 is car speed) [4, 13].

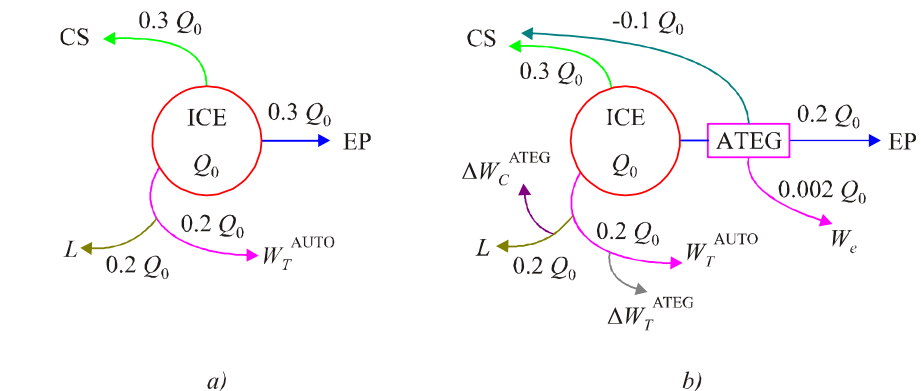


Fig. 1. Heat and energy fluxes in a car before (a) and after (b) ATEG installation on exhaust pipe.

Here, Q_0 and W_T^{AUTO} – power of burning fuel and its share spent for car motion;
 L – losses in car mechanisms; ΔW_T^{ATEG} and ΔW_C^{ATEG} – losses due to ATEG transportation and cooling
 $(\eta^{\text{ATEG}} = 0.02; W_e = 0.2 \text{ kW}; \Delta W_T^{\text{ATEG}} = 0.1 \text{ kW}; \Delta W_C^{\text{ATEG}} = 0.2 \text{ kW})$.

However, in practice the ratio $\Delta W = W_e$ in a car is never fulfilled because ATEG needs part of ICE power $\Delta W^{\text{ICE}} = \Delta W_T^{\text{ATEG}} + \Delta W_C^{\text{ATEG}}$ for its transportation ($\Delta W_T^{\text{ATEG}} > 0$) and forced cooling of the cold junctions ($\Delta W_C^{\text{ATEG}} \geq 0$) (Fig. 1 b) [13-15]. In this case, the waste heat recovery power of a car is reduced accordingly to

$$\Delta W = W_e - \Delta W_T^{\text{ATEG}} - \Delta W_C^{\text{ATEG}} \quad (1)$$

and even becomes negative, if service expenses ΔW_T^{ATEG} and ΔW_C^{ATEG} are significant [13-15]. Thus, in practice, there are two main modes of ATEG operation in a car: 1) real waste heat recovery with fuel economy ($0 < \Delta W < W_e, \delta A < 0$), and 2) simple energy generation, when no real waste heat recovery takes place, and total fuel consumption and greenhouse gas emission by cars is increased ($\Delta W < 0 < W_e, \delta A > 0$) [13-18].

The purpose of this study was to investigate the current state of ATEG problem. The experimental characteristics of serial ATEG prototypes developed recently for motorcycles, cars and trucks [1-5, 7] are analyzed. It is shown that in all the cases the performance characteristics of ATEG are significantly lower than expected by developers, owing to which the majority of ATEGs work in low-efficient simple energy generation mode [3, 6, 13]. Low efficiency of modern ATEGs is attributable in the paper to thermodynamic limitations of their specific power $\tilde{W}^{\text{ATEG}} = W_e/m^{\text{ATEG}} < 20 - 30 \text{ W/kg}$ (here m^{ATEG} – ATEG mass) in "CAR + ATEG" system. Low values of \tilde{W}^{ATEG} are explained in the paper through use of A.S. Okhotin theory [20], taking into account high parasitic thermal resistances of ATEG heat exchangers (R_{HE}^{ATEG}) on the "exhaust gas/ATEG" boundary. It is shown that because of consistently high R_{HE}^{ATEG} the prospects of using high-power ATEGs in cars are considerably limited today. Various ways for enhancement of ATEG performance are discussed, of which improvement of their heat exchangers seems to be most important.

1. "CAR-ATEG" system

Placing of ATEG in a car forms a complex thermodynamic system "CAR-ATEG" containing two dissimilar heat engines (ICE and ATEG) [13-15]. ATEG installation increases the overall mass of a car $m^{\text{AUTO+ATEG}} = m^{\text{AUTO}} + m^{\text{ATEG}}$ and its front dimensions $\Delta S^{\text{AUTO+ATEG}} \approx \Delta S^{\text{AUTO}} + \Delta S^{\text{ATEG}}$, resulting in increased motion resistance force $F_R \rightarrow F_R + \Delta F_R$ (Here m^{AUTO} is mass of a car, and ΔS^{AUTO} and ΔS^{ATEG} are front dimensions of a car and ATEG, respectively ($a \rightarrow b$, Figure 2) [3]. Moreover, with

increase in $W_e > 0$, conflict between heat engines (ICE and ATEG) is developed in "CAR-ATEG" system. The conflict is due to competition of heat engines for sources and sinks of heat in the system [14]. Development of the conflict between heat engines in "CAR-ATEG" system reduces the efficiency of the ICE and restricts increase in W_e and ΔW of ATEG [13-18]. The influence of all factors discussed above on the experimental characteristics of ATEG is considered below.

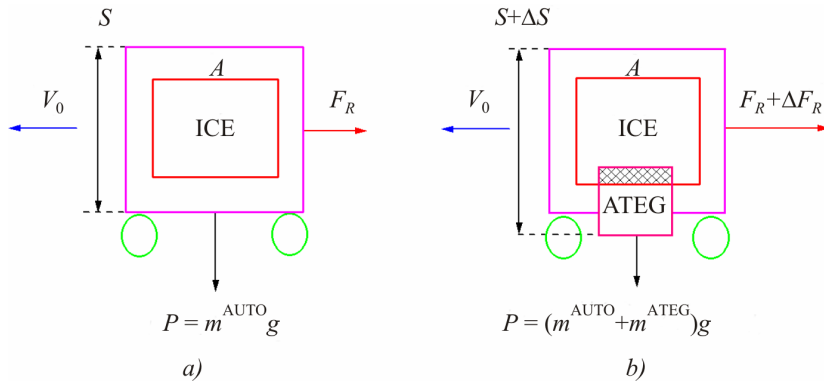


Fig. 2. Changes in mass m , weight P , front dimensions ΔS , motion resistance force ΔF_R and development of a conflict between heat engines (internal combustion engine and ATEG) (shaded area) with ATEG installation on a car (A) (a → b).

1.1. Experimental characteristics of ATEG

Table 1 shows the experimental characteristics of serial ATEG prototypes designed for motorcycles, cars, pickups and trucks [1, 2-7]. According to [1, 2-7], we have calculated the specific power of vehicles $\hat{W}^{\text{AUTO}} = W^{\text{AUTO}}/m^{\text{AUTO}}$ and the specific power of installed ATEG $\hat{W}^{\text{ATEG}} = W_e/m^{\text{ATEG}}$, waste heat recovery power ΔW and a change in fuel consumption δA with ATEG operated at full capacity (Table 1). In the calculations we used the ratio (1) assuming for simplicity $\Delta W_C = 0$; $\Delta W_T^{\text{ATEG}} = \Delta W_{T1}^{\text{ATEG}} + \Delta W_{T2}^{\text{ATEG}}$ (Here $\Delta W_{T1}^{\text{ATEG}} = 0.1 W^{\text{ICE}} \cdot m^*$ and $\Delta W_{T2}^{\text{ATEG}} = 0.1 W^{\text{ICE}} S^*$ are additional expenditures of engine power to overcome rolling friction and air resistance when driving, $m^* = m^{\text{ATEG}}/m^{\text{AUTO}}$ and $S^* = \Delta S^{\text{ATEG}}/S^{\text{AUTO}}$ are the mass-factor and form-factor of ATEG in a car). Table 1 shows that the operating efficiency of modern ATEGs (Table 1) is generally low.¹ Maximum W_e values of ATEG did not exceed $\sim 1/3 - 2/3$ of the calculated values needed to power the vehicles. In so doing, all ATEGs (Table 1) were operated mainly in a low-efficiency simple energy generation mode (SEG) ($\Delta W < 0$) (motorcycles, cars), or in the mode of real waste heat recovery which is close to simple energy generation mode (pickups, trucks). A change in SEG → WHR mode (Table 1) was due to a decrease in mass-factor m^* and form-factor S^* of ATEG in motorcycle → truck series.

As a result, in practice, the real waste heat recovery was possible only for trucks ($m^{\text{AUTO}} > 6$ t; $\Delta W > 0$, $\delta A < 0$), but not for cars, pickups ($m^{\text{AUTO}} = 2 - 5$ t; $\Delta W \sim 0$, $\delta A \sim 0$) and motorcycles ($m^{\text{AUTO}} \ll 1$ t; $\Delta W < 0$, $\delta A > 0$). From Table 1 it is also evident that at $m^* = \text{const}$ the waste heat recovery power ΔW can be increased by reducing the form-factor of ATEG ($S^* \rightarrow 0$).² In this case the value of ΔW will be only limited by two main factors – W_e and m^{ATEG} determining specific power \hat{W}^{ATEG} . According to our calculations, the specific powers of ATEG for all vehicles proved to be low $\hat{W}_T^{\text{ATEG}} < 20 - 30$ W/kg, and never exceeded even the specific power of internal combustion engine spent on vehicle motion $\hat{W}_T^{\text{AUTO}} = \frac{1}{2} \hat{W}^{\text{ICE}} \sim 15 - 26$ W/kg (Table 1) [4, 13]. As a result, for motorcycles, cars

¹ Characteristics of ATEG (Table 1) were obtained when driving on the highway at a limit speed $V_0 \sim 110 - 150$ km/h. When driving in the city ($V_0 \sim 30 - 60$ km/h), they will be reduced by a factor of 3 to 6 again.

² It can be done due to the use of air cowls and flush mounting of ATEG [3, 9].

and pickups we have $\hat{W}_T^{\text{AUTO}} > \hat{W}_e$, that is, the gain in the total power of a car due to net power W_e of ATEG does not compensate ICE service costs even for ATEG transportation (Table 1). On the contrary, for trucks we get $W_e > W_T$, which is related to their relatively low specific power expenditures on motion ($\hat{W}^{\text{AUTO}} < \hat{W}^{\text{ATEG}}$) (Table 1). The issue of low specific power \hat{W}^{ATEG} calls for special discussion.

Table 1
Characteristics of serial ATEG prototypes designed for various vehicles [1, 2-7]

Nº	Characteristics	Motorcycle ^a	Car ^b	Pickup ^c	Truck ^d
1.Vehicle	Engine displacement V , l and type	0.4 G	3.4 D	5.3 G	14 D
	Internal combustion engine power, W^{ICE} , kW	7.4	125	146	162
	Mass, m^{AUTO} , kg	150	1545	2770	10000
	Specific power \hat{W}^{AUTO} , W/kg	49	81	53	16.2
	Specific power of motion, $\hat{W}_T^{\text{AUTO}} = \frac{1}{2} \hat{W}^{\text{ICE}}$, W/kg	24	40	26	8
	Front size S^{AUTO} , m ²	0.7	2.5	4	5
2.ATEG	Achieved maximum power W_e , W	10	200	300* 600**	400*** 1000****
	Necessary power, W_e^* , W	100 – 200	~ 600	~ 1000	> 1000
	Material of ATEG legs	Fe_2Val	$(Bi, Sb)_2Te_3$	$PbTe$	$(Bi, Sb)_2Te_3$
	Mass, m^{ATEG} , kg	~ 3	13	39.1	13
	Specific power \hat{W}^{ATEG} , W/kg	3.3	15	7.7* 15.4**	30.8*** 76.9****
	Dimensions, ΔS^{ATEG} , cm ²	100	220	590	412
	Mass-factor, m^*	0.02	0.008	0.014	0.001
3. Power losses	Form-factor, S^*	0.014	0.009	0.015	0.008
	Losses due to mass-factor, W_{T1}^{ATEG} , W	20	143	279	29
	Losses due to form-factor, W_{T2}^{ATEG} , W	14	149	292	180
	Total power gain, $\Delta W = (W_e - W_{T1}^{\text{ATEG}} - W_{T2}^{\text{ATEG}})$, W	-24	-92	-271* 29**	191*** 791****
	Change in fuel consumption, $\delta A = \Delta W / (0.2 Q_0)$, %	0.65	0.15	0.37* -0.04**	-0.24*** -0.97****

^{a)} Suzuki ¹⁰; ^{b)} BMW531 ^{5, 6}; ^{c)} GM Sierra 1500 ³; ^{d)} Engine NTC-350 ³; * – traffic in the city ($V_0 \sim 60$ km/h); ** – traffic on the highway ($V_0 \sim 110 - 150$ km/h)³; *** – received; **** – expected. G – gasoline, D – diesel.

1.2. Low specific power of ATEG

Table 2 shows a comparison of the specific power \hat{W}^{ATEG} to the specific power of thermoelectric generators (TEG) of other types (\hat{W}^{TEG}) using solid or liquid heat carriers [19, 21-23].

According to Table 2, using the same thermoelectric materials (TEM) we have $\hat{W}^{\text{TEG}}/\hat{W}^{\text{ATEG}} \geq 10 - 20$. Accordingly, provided $W_e = \text{const}$, the masses of ATEG will exceed considerably the masses of other types of TEG ($m^{\text{ATEG}}/m^{\text{TEG}} \sim 10 - 30$ and more) (Table 2).

Table 2
*Comparison of specific power \hat{W}^{ATEG} to that of thermoelectric generators
 of other types \hat{W}^{TEG} using liquid or solid heat carriers*

Material of legs	Density d , g/cm ³	Specific power \hat{W} , kW/kg		$\hat{W}^{\text{TEG}}/\hat{W}^{\text{ATEG}}$ ratio
		ATEG	Other TEGs	
<i>Bi-Sb-Te-Se</i>	6.5 – 7.8	0.015 [3]	0.17 – 0.3 [21] ~ 0.2 [4]	11 – 20
<i>PbTe</i>	8.16	0.008 – 0.015 [3]	0.2 – 0.25 [4, 21]	13 – 31
<i>Si-Ge</i>	2.5 – 2.9	0.003 [3, 8]	≤ 1.2 [21]	400
<i>Mg₂Si_{0.4}Sn_{0.6}</i>	~ 2.9	~ 0.07 – 0.1 [8, 23]	~ 0.8 – 1 [23]	8 – 14

As is known, the mass of legs m_L necessary for production of assigned net power of TEG W_e is given by the expression

$$m_L = Vd = 2W_e l^2 d / (A\Delta T^2), \quad (2)$$

where V and d are the volume and density of thermoelectric material, l is the height of legs; $A = Z\kappa = \alpha^2\sigma$ is power factor; α , σ and κ are the Seebeck coefficient, specific electric and heat conductivity of legs, and ΔT is operating temperature difference on thermocouple legs [22]. From Eq. (2) it follows that for the same TEM ($A, d = \text{const}$) the ratio $\hat{W}^{\text{TEG}}/\hat{W}^{\text{ATEG}} \sim 10 - 30$ (Table 2) can be explained by increased ATEG height l and reduced operating temperature differences ΔT on their legs. Comparison of the TEG and ATEG design features has confirmed this assumption. Indeed, the height of ATEG legs reaches $l^{\text{ATEG}} \sim 5, 7.5$ and 10 mm [3, 4, 7, 22], whereas in other types of TEG it is significantly lower (usually $l^{\text{TEG}} = 1 - 3$ mm) [21, 23]. In the same way, the operating temperature differences on ATEG legs are much lower $\Delta T^{\text{ATEG}} \sim \frac{1}{2}\Delta T_0$ [9, 24] compared to other types of TEG, where usually $\Delta T^{\text{TEG}} \sim \Delta T_0$. (Here ΔT_0 is the available temperature difference provided by the source of heat) [21, 23]. As a result, other things being equal, we have $W_e^{\text{TEG}}/W_e^{\text{ATEG}} \sim 2$, $m^{\text{ATEG}}/m^{\text{TEG}} \sim 2$, which yields $\hat{W}^{\text{TEG}}/\hat{W}^{\text{ATEG}} \sim 10 - 20$ in accordance with Table 2. Low \hat{W}^{ATEG} values are attributable below to difficulties of heat exchange in "CAR+ATEG" system [2, 13-15].

2. ATEG calculations

2.1. Heat exchange in "CAR+ATEG" system

Unlike the internal combustion engine, ATEG is the "external" combustion engine, so it needs two additional heat exchangers connected to heat sources and sinks in a car [2, 15]. Heat removal from ATEG is generally provided by "standard" or additional autonomous cooling system with water or air cooling [3-6].³ As sources of heat for ATEG, apart from the exhaust pipe, we will also consider internal combustion engine and cooling system having additional reserves for waste heat recovery of cars (Fig. 1). Heat in a car is transferred by hot gases from the internal combustion engine to exhaust pipe, and also by a coolant (water and/or air) through cooling system to atmosphere. Heat in ATEG is

³ The use of standard car cooling system is considered to be optimum [3, 4].

transferred by electrons and phonons due to thermal conductivity of legs and the Peltier effect (in energy generation mode) [2, 17]. In so doing, the mechanisms of heat transfer in ATEG appear less efficient than combined heat and mass transfer in the pipes [13-15]. As a result, thermal resistance of ATEG (R_{T}^{ATEG}) essentially exceeds thermal resistances of internal combustion engine, exhaust pipe and cooling system ($R_{T}^{ICE, EP, CS}$) which determines the difficulties of heat exchange in the system [13, 14]. Besides, as mass transfer in ATEG legs is impossible⁴, for heat removal to ATEG in a car one can use only parallel connection of ATEG to the pipes [13, 16]. In this case it is possible to take away to ATEG not the entire heat flux in a pipe ($Q_0^{ICE, EP, CS}$), but only its small part $Q_0^{ATEG} \sim Q_0^{ICE, EP, CS} \cdot R_{T}^{ICE, EP, CS} / (R_{T}^{ATEG} + R_{T}^{ICE, EP, CS}) \ll Q_0$, inversely proportional to R_{T}^{ATEG} .

The scheme of parallel connection of ATEG to exhaust pipe is shown in Fig. 3. From Fig. 3 it is seen that process of heat removal from exhaust gas to ATEG (arrow) is interfered by motionless gas and coke layers with a low heat conductivity adsorbed on the "exhaust gas/exhaust pipe" heat exchange boundary (2, 4) [2, 23, 26]. A layer of adsorbed gas (of thickness $d \sim 1 - 2$ microns) is constantly present on the inside of exhaust pipe at any velocities of exhaust gas motion in it (V^{EP}) (2, Fig. 3) [2]. Thus, coke layers (4, Fig. 3) can achieve thickness $c \sim 1$ mm and more in the "cold" parts of exhaust pipe [13, 16].

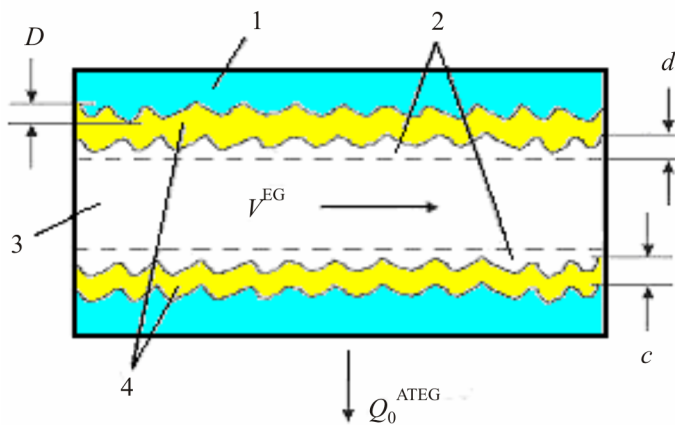


Fig. 3. Parallel connection of ATEG to exhaust pipe. 1 – exhaust pipe case; 2 – adsorbed gas layer; 3 – exhaust gas; 4 – carbon deposit; d, c – gas and carbon deposit layers; V^{EG} – exhaust gas velocity; D – roughness of exhaust pipe internal surface, Q_0^{ATEG} – input heat flux of ATEG.

Owing to high thermal resistances of the adsorbed layers (2, 4, Fig. 3), the thermal resistances of ATEG essentially increase. Thus, input heat fluxes Q_0^{ATEG} and the operating temperature difference on ATEG legs decrease accordingly $\Delta T \sim \Delta T_0 \cdot R_{T}^{ATEG} / (R_{T}^{HE} + R_{T}^{ATEG})$ [11, 13, and 24]. We have taken into account the above peculiarities of heat exchange in "CAR + ATEG" system in deciding on ATEG thermal model [13].

2.2. ATEG thermal model

ATEG thermal model used in the work is shown in Fig. 4 [13]. The model (Fig. 4) takes into account thermal resistances of exhaust pipe $R_{EP}^T = R_0^T + R_1^T$ (here R_0^T and R_1^T are the beginning and the remaining portion of exhaust pipe), thermocouple legs R_3^T , and also "hot" and "cold" heat exchangers R_2^T and R_4^T of ATEG ($R_{TO}^T = R_2^T + R_4^T$). The formulae for calculation of ATEG parameters for the model (Fig. 4) corresponding to maximum power (I), or maximum efficiency (II) modes are presented in Table 3. Two boundary conditions were used: 1) constant temperature of junctions ($T_h = \text{const}$, $T_c = \text{const}$) (The theory of A.F. Ioffe) [19] and 2) constant temperature of heat-carriers ($T_h' = \text{const}$, $T_c' = \text{const}$) (The theory of A.S. Okhotin) [20].

⁴ Exception is provided by "permeable" thermoelements [25].

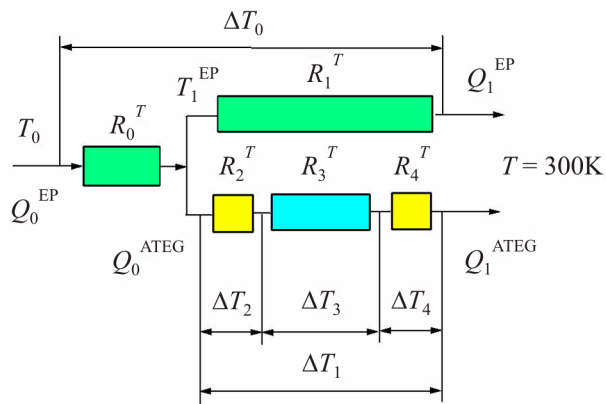


Fig. 4. Thermal model of parallel connection of ATEG to exhaust pipe and the respective temperature differences ΔT_i (ATEG idling mode). Thermal resistances of segments: R_0^T – exhaust pipe beginning; R_1^T – exhaust pipe remainder; R_3^T – thermocouple legs; R_2^T and R_4^T – “hot” and “cold” heat exchangers of ATEG [13].

Table 3

*Optimum parameters of thermoelectric generators operated in the modes of maximum power (I) and maximum efficiency (II) under various boundary conditions (the shaded area is for ratios suitable for calculations of ATEG) **

Mode	Parameters	Boundary conditions	
		Fixed temperature of junctions: $T_h = \text{const}$, $T_c = \text{const}$ [11]	Fixed temperature of heat carriers: $T_h' = \text{const}$, $T_c' = \text{const}$ [12]
I. Maximum power	Relative electric load, $M = R/r$	1	$A^* = M_0$
	Power, W_e^{\max}	$E_{ID}^2/(4r) = W\Delta T^2/4$	$E_{ID}^2/(4A^*r) = W\Delta T^2/4A^*$
	Temperature difference on the legs, ΔT	$(T_h - T_c)$	$(T_h' - T_c')(A^* + 1)/(4A^*)$
	Efficiency, $\eta (W_e^{\max})$	$\eta_c/(2 + 4/ZT_h - \eta_c/2)$	$\sim 0.22 \eta_c(M_0 - 1)/(M_0 + T_c'/T_h')$
	Optimum dimensionless height of legs, l_0	$\beta \sim 0.1$	$Bi = M_0$
II. Maximum efficiency	Relative electric load, $M = R/r$	M_0	M_0
	Temperature difference on the legs, ΔT	$(T_h - T_c)$	$(T_h' - T_c')$
	Power, $W_e (\eta_{\max})$	$M_0 E_{SC}^2/[r(1 + M_0)^2]$	0
	Efficiency, η_{\max}	$\eta_c(M_0 - 1)/(M_0 + T_c'/T_h')$	$\eta_c(M_0 - 1)/(M_0 + T_c'/T_h')$
	Optimum height of legs, l_0	∞	∞

Here: $M = R/r$ is relative electric load of ATEG; R is electric resistance of load; $r = r_0(1 + \beta)$ is electric resistance of ATEG; r_0 is electric resistance of legs; $\beta = (r_j + r_c)/r_{sc}$ is factor of electric losses; r_j , r_c and r_{sc} are electric resistances of contacts, connecting plates and semiconductor material of legs, $M_0 = (1 + Z \bar{T})^{1/2}$; $Z = Z_0/(1 + \beta)$ and Z_0 is the thermoelectric figure of merit of TEG with and without account of electric losses; $T = \frac{1}{2}(T_h + T_c)$ is the average temperature; $E_{ID, SC} = (\alpha_p - \alpha_n) \Delta T^{ID, SC}$ are thermoEMF in idling and short circuit mode of thermocouples; $\eta_c = (T_h - T_c)/T_h$ is the Carnot factor; $A^* = (1 + Z \bar{T})/(1 + Bi)$ is the ATEG's constant; $R^T = (R_3 + R_4 + R_5)$ – the sum of thermal resistances of legs and heat spreaders; $Bi = R_{nn}^T / R_{mo}^T$ – the ratio of thermal resistances of semiconductor legs of ATEG and heat exchangers (integral Biot criterion of ATEG).

Comparison of Fig. 4 and Table 3 shows that the Ioffe theory [19] takes into account only the contribution of thermocouple legs (R_3^T) and their contact electric resistances (through parameter β) to overall thermal and electrical balance of ATEG ($R_3^T \neq 0, R_0^T = R_1^T = R_2^T = R_4^T = 0$, the integral Biot criterion of ATEG $Bi = R_3^T / (R_2^T + R_4^T) = \infty$) (Fig. 4). However, in real practice for all ATEGs we have $Bi \sim 1$ [13], so the Ioffe theory [19] is not the best approximation for ATEG [20]. It is shown below that the Okhotin theory [20] that takes into account the contribution of ATEG heat exchangers R_{TO}^T to thermal balance of the system ($R_2^T, R_3^T, R_4^T \neq 0, Bi \sim 1$, Fig. 4) is best suited for the calculations of ATEG.

2.3. The Ioffe and Okhotin theories

For the calculations of ATEG we employed a cylindrical layered model of length $L = 0.6$ m, with an internal diameter $D = 0.05$ m [13]. The optimal height of ATEG legs $l = 0.5$ cm (for Bi_2Te_3) was estimated from the condition $Bi = M_0$ (Table 3). In the calculations, the film thickness of the adsorbed gas on the surface of the heat exchange "exhaust gas/exhaust pipe" was assumed equal to the roughness of exhaust pipe ($d \sim D \approx 0.0001$ m) (2, Fig. 3). The contribution of coke layer (4, Fig. 3) to R_2 for simplicity was not taken into account [13]. Calculations were made using Ohm's and Kirchhoff's laws for electrical and thermal circuits of ATEG. [13]. In our calculations we employed the values $Q_0^{ICE, EP, CS} = Q_0; 0.3 Q_0; 0.3 Q_0; \Delta T_0^{ICE, EP, CS} \sim 1400; 650; 50$ K and $Q_0 = 100$ kW (gasoline engine $W^{ICE} \approx 54$ h.p.).

Figure 5 shows the results of calculation of the thermal resistances $R^T = \Delta T/Q$ (A) and available thermal heads ($Q\Delta T$) (B) for internal combustion engine (the area of combustion chamber), exhaust pipe and cooling system (the area from ICE water "jacket" to radiator) with water (4) and air cooling (5) of ATEG. From Figure 5 it follows that in all the cases the relation $R_T^{ATEG} \gg R_T^{ICE, EP, CS}$ is fulfilled, and in going from water cooling to air cooling, the thermal resistance R_T^{ATEG} further increased by a factor of ~ 2 (4 \rightarrow 5). Thus, below we will consider the case of ATEG water cooling only ($R_4^T = 0$).⁵

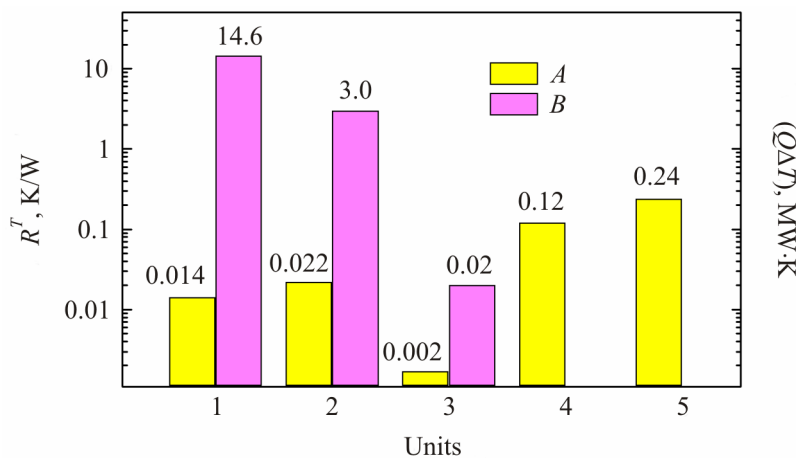


Fig. 5. Thermal resistances $R^T = \Delta T/Q$ (A) and available thermal heads ($Q\Delta T$) (B) for different car units.
 1 – internal combustion engine; 2 – exhaust pipe; 3 – cooling system; 4 – standard size ATEG with Bi_2Te_3 legs ($l = 5$ mm). ATEG cooling: 4 – water; 5 – air (calculated according to model in Fig. 4, at $R_0 = 0$).

Figs. 6 – 8 show the dependences of the efficiency η^{ATEG} , as well as operating temperature difference on the legs ΔT and the optimum height of the legs l versus the ZT of the samples, calculated using the

⁵ If necessary, ATEG air cooling is used only in motorcycles [1, 7].

theories of Ioffe [19] and Okhotin [20] in maximum efficiency and maximum power modes (Table 3). According to our calculations, in maximum efficiency mode the values of η in the theories of Ioffe [19] and Okhotin [20] coincide (curve 1, Figure 6). However, when passing to the mode of maximum power (which is the operation mode of ATEG), these theories yield significantly different values of η_W . The Ioffe theory gives $\eta_W \sim 0.8 \cdot \eta$, and the Okhotin theory – $\eta_W \sim 0.22 \cdot \eta$ (curves 2 and 3, Figure 6).

In addition, in maximum power mode, the Okhotin theory [20] predicts the dependence of the temperature difference ΔT on ATEG legs on the ratio of its thermal and electrical characteristics (A^* and M). As a result, the expected values of W_e and the optimum height of the legs l are also found to depend on the thermal resistances of heat exchangers ($R_2^T, R_4^T \neq 0$) and the relative electrical load $M = R/r$ of ATEG (I, Table 3). This significant difference between the Ioffe [19] and Okhotin [20] theories (Fig. 6 – 8) is due to account in the theory [20] of the contribution of large parasitic thermal resistances of heat exchangers R_2^T and R_4^T (Fig. 4), which in the theory [19] are assumed equal to zero. This result can be explained by the known rule of H. Lenz (Figure 9), which is applicable to any source of energy operated in maximum power mode [27, 28]. Since any TEG is a thermal and electric engine simultaneously, Lenz's rule, generally speaking, should be applied to it twice, namely, first to the thermal, and then to the electric circuits [17].

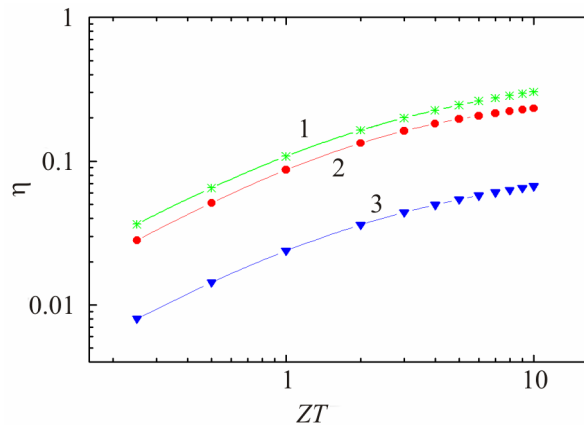


Fig. 6. The efficiency η^{ATEG} versus thermoelectric figure of merit ZT of thermocouple leg materials.

Modes: 1 – maximum efficiency;

2, 3 – maximum power. Theories: 1, 2 – Ioffe [19];

1, 3 – Okhotin [20] ($T_h = 600$ K; $T_c = 300$ K).

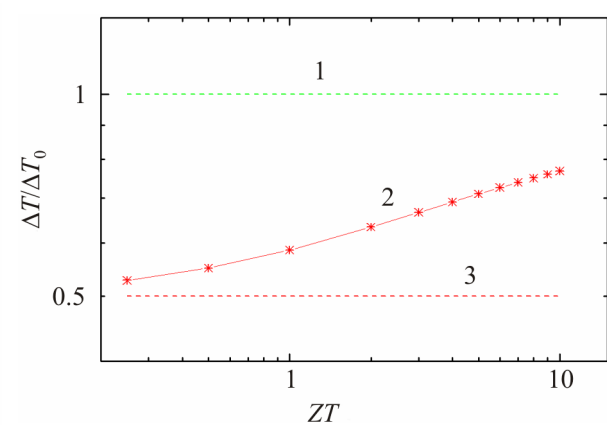


Fig. 7. The ratio of operating temperature difference ΔT on ATEG legs to temperature difference of heat-carriers $\Delta T_0 = (T_h - T_c)$ in maximum power mode versus figure of merit ZT of materials.

Theories: 1 – Ioffe [19]; 2, 3 – Okhotin [20];

3 – Lenz's rule.

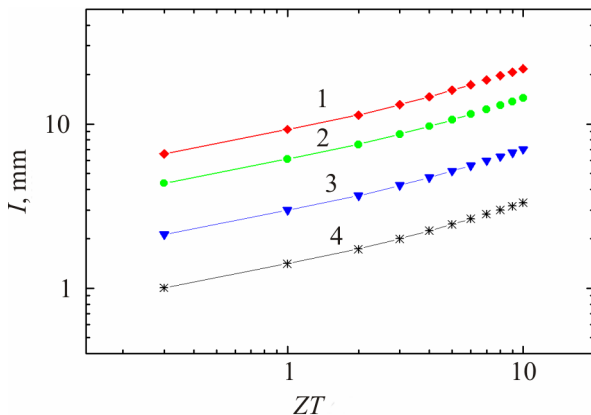


Fig. 8. The optimum length of legs l of ATEG (1 – 3) and TEG versus thermoelectric figure of merit ZT (water cooling). Leg materials: 1 – PbTe; 2, 4 – Bi_2Te_3 ; 3 – “phonon glasses”. Thermal conductivity κ , W/(cm·K): 1 – 0.025; 2, 4 – 0.015; 3 – 0.005. Theories: 4 – Ioffe [19]; 1 – 3 – Okhotin [20].

2.4. The Lenz rule

According to Lenz's rule for electric circuits, maximum power W_e of ATEG as electric engine is achieved with equal electrical resistivities of legs (r) and the load (R) ($r = R$) (Fig. 9 b) [19, 20]. On the other hand, according to Lenz's rule for thermal circuits, the maximum thermal head ($Q\Delta T$) on ATEG legs is achieved with equal thermal resistances of heat exchangers and legs ($R_{TO}^T = r^T$, Fig. 9 c; $R_{TO}^T = R_2^T + R_4^T$, $r^T = R_3^T$, Fig. 4). Both theories [19, 20] apply Lenz's rule to electric circuits of ATEG (Fig. 9 b), however, it is only the Okhotin theory [20] that additionally applies Lenz's rule to its thermal circuits (Fig. 9 c) (Table 3). In the Ioffe theory [19] the thermal resistances of heat exchangers are neglected ($R_{HE}^T = 0$, Table 3), so, Lenz's rule is not applied to ATEG thermal circuits. As a result, the temperature difference on the legs turns out to be equal to available temperature difference assigned by the heat source ($\Delta T_0 = \Delta T_r$, Fig. 9 c). This approximation is well satisfied in the case of the TEGs using solid or liquid heat carriers (Table 2).

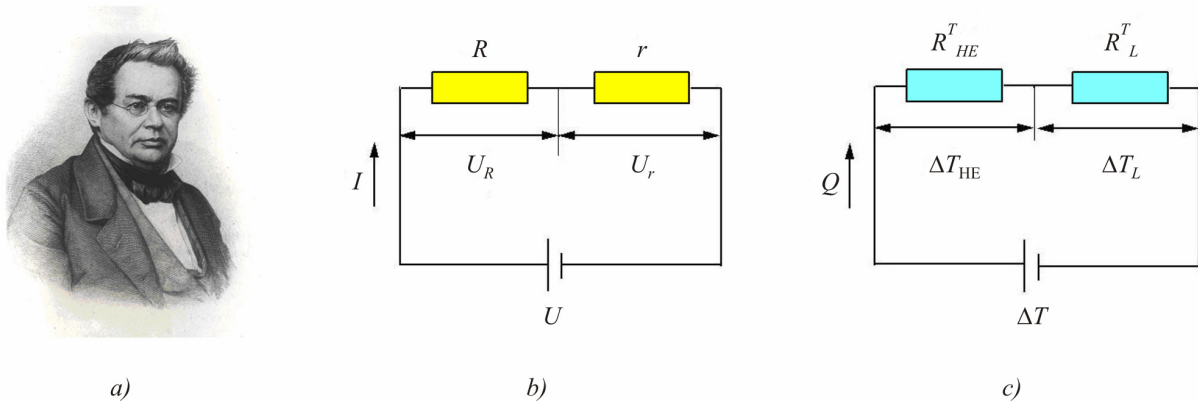


Fig. 9. Academician E.H. Lenz (1804 – 1865) (official portrait at RAS) [27, 28] (a), and application of his rule to electric ($R = r$) (b) and thermal ($R_{TO}^T = r^T$) (c) ATEG circuits.

Here: R and r are electric resistances of external load and the legs;
 R_{HE}^T and R_L^T are thermal resistances of heat exchangers and ATEG legs.

In the Okhotin theory [20], where $R_{HE}^T \neq 0$ (Fig. 9 c), the application of Lenz's rule to ATEG thermal circuits yields $\Delta T = \frac{1}{2} \Delta T_0$ for idling mode (3, Figure 7) [20].⁶ According to the theory [20], in maximum power mode the value of ΔT on ATEG legs further increases with a rise in ZT (curve 2, Figure 7) [20]. Accordingly, in the theory [20], the optimal length l of ATEG legs increases as compared to the Ioffe theory [19], but the increase in l appears proportional to the thermal conductivity κ of the TEM (curves 4 → 1, Figure 8).

Theories [19] and [20] also give a different prediction for the value of the net power W_e of ATEG in a car (Fig. 10). Fig. 10 shows the input thermal fluxes Q_0^{ICE} , Q_0^{EP} and Q_0^{CS} in a car (a, I → III), their share which can be taken away to ATEG (Q_0^{ATEG}) (b), and calculated net power $W_e = \eta^{ATEG} Q_0^{ATEG}$ ($\eta^{ATEG} = 0.05$) with ATEG operated in maximum power mode without account of thermal resistances of heat exchangers (the Ioffe theory [19]) (c) and with account of their contribution (the Okhotin theory [20]) (d). Fig. 10 shows that the Ioffe theory gives 3 fold overestimated values of ATEG power $W_e = 0.5$; 0.17 and 0.003 kW corresponding to placing ATEG on the internal combustion engine (I), on the exhaust pipe (II) and cooling system (III) (c). Actually, with account of parasitic thermal resistance of heat exchangers $R_{TO}^T \approx R_2^T$ we have $W_e < 0.5$; 0.17 and 0.003 kW (d, Fig. 10), which is ~ 0.5, 0.2, and 0.03 % of the power released at fuel combustion Q_0 (d, Fig. 10).

⁶ Earlier, Lenz's rule for ATEG thermal circuits was taken into account in [9, 24].

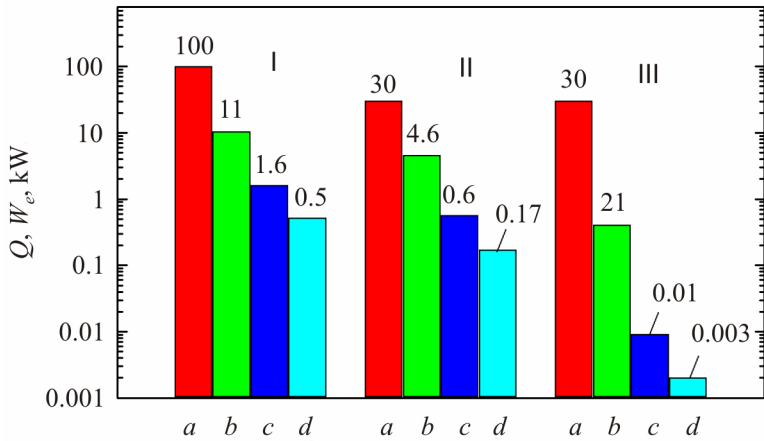


Fig. 10. Available input heat fluxes of a car Q_0 (a), their share that can be taken away to ATEG (Q_0^{ATEG}) (b), and maximum net power W_e of ATEG (c, d) (water cooling). Theories: c – Ioffe [11]; d – Okhotin [12]. ATEG location: I – ICE; II – EP; III – CS ($Q_0 = 100$ kW, $ZT = 1$).

The last estimates are in agreement with the experiment (Table 1), so the Okhotin theory [20] is a better approximation for ATEG calculations than the Ioffe theory.⁷ Further development of ATEG theory supposes a detailed account of the interaction between heat engines of "CAR-ATEG" system.

3. Conflict between ICE and ATEG

3.1. Placing ATEG in a car

A conflict between various heat engines forming one thermodynamic system is a widespread technical problem [2]. The specific feature of the conflict between ICE and ATEG in "CAR+ATEG" system is its dependence on ATEG location in a car [13]. According to Figs. 3 and 10, as a heat source for ATEG, the exhaust pipe ($Q_0^{ATEG} \leq 0.3Q_0$) and ICE ($Q_0^{ATEG} \leq Q_0$) are suitable due to appropriate parameters of R_T and $(Q_0\Delta T)$. Placing ATEG on cooling system ($Q_0^{ATEG} \leq 0.3Q_0$) is ineffective because of the smallness of R^T and $(Q_0^{CS}\Delta T)$.⁸ However, placing ATEG on ICE is not efficient either because of the conflict between ICE and ATEG that develops with increasing W_e in "CAR + ATEG" system [13-15]. Indeed, at placing ATEG in ICE, the heat engines compete for burnt fuel power Q_0 [15]. In this case the conflict between heat engines evolves rapidly with increase in W_e resulting in a sharp decrease in the overall efficiency of (ICE + ATEG) system

$$\eta_{ICE+ATEG}^{ICE+ATEG} = \eta_{ICE}^{ICE}(1 - \delta) + \eta_{ATEG}^{ATEG}\delta, \quad (3)$$

where $\delta = Q_0^{ATEG}/Q_0$ is the share of heat rejected from internal combustion engine to ATEG [15]. The reduction of $\eta_{ICE+ATEG}^{ICE+ATEG}$ has a simple physical meaning because part of burnt fuel power Q_0 is used by less efficient heat engine ($\eta_{ATEG}^{ATEG} \ll \eta_{ICE}^{ICE}$) [2, 15]. For this reason, ATEG is not currently installed in ICE, despite the large available thermal head ($Q\Delta T$) and the acceptable value of thermal resistance R_T^{ICE} (1, Figure 5) [17, 18].⁹

On the other hand, at placing ATEG on exhaust pipe, both heat engines compete for peripheral

⁷ The Ioffe theory [19] was used for ATEG calculation in [1, 3-6], owing to which the expected characteristics proved to be overestimated (Table 1).

⁸ According to our estimate, the efficiency of cooling system waste heat recovery can be increased by a factor of 10 and more by placing the hot junctions of ATEG thermocouples in the internal combustion engine case.

⁹ Placing ATEG in the internal combustion engine may prove to be efficient in the future on achievement of $\eta_{ATEG}^{ATEG} - \eta_{ICE}^{ICE}$ parity as a result of increase in TEM ZT .

thermal fluxes in the system (Q_0^{EP} and Q_0^{CS}), and the conflict between heat engines is reduced accordingly. In this case, the basic influence of ATEG on the work of internal combustion engine is expressed in the reduction of exhaust pipe temperature (T^{EP}) and in the rise of cooling system temperature (T^{CS}) [13]. Note that the Ioffe theory [19] does not predict any reduction of T^{EP} temperature (Table 3), whereas in the theory of Okhotin [20] a reduction of T^{EP} temperature for high-power ATEG may prove to be considerable (up to 100K) [13]. As a result, the value W_e of ATEG is limited at the expense of decrease in the Carnot factor η_C and owing to coke deposition on the internal side of exhaust pipe which makes heat exchange difficult (4, Fig. 4) [13, 14]. According to our estimate, with coke layer thickness $d = 0.3$ mm, the value W_e of ATEG can decrease by a factor of 3 to 5 [17-18]. On the other hand, increase in T^{EP} results in the overload of cooling system which necessitates power increase of cooling system drives (ΔW_C^{ATEG}) [13-15]. Assuming for simplicity that $\Delta W^{\text{CS}} \sim 0.03 Q_1^{\text{ATEG}}$, where Q_1^{ATEG} is output heat flux power of ATEG, we get $\Delta W_C^{\text{ATEG}} \sim W_e$. Thus, with regard to ΔW_C^{ATEG} the real power of waste heat recovery ΔW can essentially decrease as compared to account of only mass-factor m^* of ATEG (Table. 1) [18].

3.2. Real operating modes of ATEG

Fig. 11 shows a reduction in automotive waste heat recovery power ΔW (1) with a rise in ATEG W_e with consecutive account of the contribution of ATEG mass-factor m^* (1 → 2), as well as additional power expenses for ATEG cooling ΔW_C^{ATEG} (2 → 3). In the calculation of ATEG m^* (Fig. 11) it was assumed that $m^{\text{ATEG}} = k_m \cdot m_L$, where m_L is overall mass of leg materials (Bi_2Te_3) (2), $k_m = 2$ is the factor that takes into account the mass of ATEG armature. From Fig. 11 it is evident that with account of losses due to ATEG mass-factor m^* , the system passes from a mode of ideal waste heat recovery (A) ($\Delta W = W_e$) into a mode of real waste heat recovery (B), where fuel saving is still possible, ($0 < \Delta W < W_e$, $\delta A < 0$). Then, with additional account of service expenses ΔW_C^{ATEG} (4), the system passes into simple energy generation mode (C), where fuel consumption by a car is increased ($\Delta W < 0$, $\delta A > 0$) (Fig. 11) [17, 18].

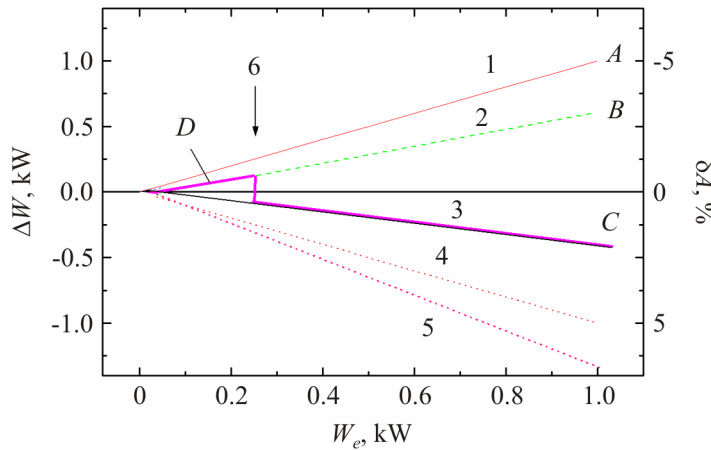


Fig. 11. Waste heat recovery ΔW of a car versus ATEG power (1–3). Modes: 1 – without regard to losses ($\Delta W = W_e$); 2 – account of losses due to motion; 3 – account of losses due to cooling system (CS) cooling and motion (5). Losses: 4 – due to CS cooling; 5 – CS cooling and motion; Modes: A – ideal waste heat recovery; B, D – real waste heat recovery; C – simple generation of energy; D – the use of CS reserves. 6 – the moment of switching additional power of CS drives.

(CS reserve – 30 % (9 kW), $Q_0 = 100$ kW; $k_m = 2$; $\eta^{\text{ATEG}} = 0.03$; $l = 6$ mm; Bi_2Te_3).

From Fig. 11 follows that at small net powers $W_e \geq 0$ and $\Delta W_C^{\text{ATEG}} = 0$ (interval D) any ATEG can work in a car in a mode of real waste heat recovery (B) at $\Delta W_C^{\text{ATEG}} = 0$, provided the reserves of standard automotive cooling system are used for cooling cold junctions of ATEG [14]. Extent of interval D in Fig. 11 corresponds to cooling system reserve of cooling power $\Delta W_C \sim 30\%$ (9 kW). When a larger power comes from ATEG to cooling system (at $W_e > 0.2$ kW), additional cooling systems drives are switched on (arrow 6, Fig. 11) and ATEG passes into simple energy generation mode (C), where fuel consumption of a car is increased ($\Delta W < 0$, $\delta A > 0$). Thus, using a combined operation mode DC (Fig. 11), one can, if necessary, either reduce W_e to increase waste heat recovery power ΔW , or, on the contrary, increase W_e , converting ATEG into simple energy generation mode.

Fig. 12 shows dependences of ATEG effective efficiency $\eta^* = \eta^{\text{AUTO}}(W_e/\Delta W_R^*)$ versus W_e in the described B, C and D modes (Fig. 11). From Fig. 12 it is evident that in a mode of real waste heat recovery (B and D) the value η^* of ATEG appears enough high (~ 0.5) (B).

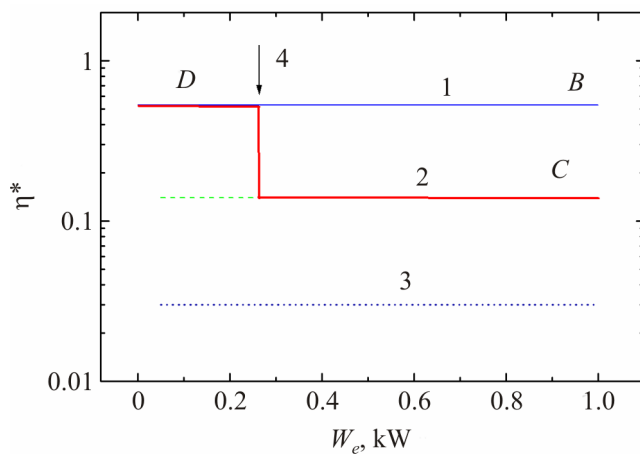


Fig. 12. Dependences of effective efficiency $\eta^ = \eta^{\text{AUTO}} W_e / \Delta W^{\text{ICE}}$ of electric energy generation by means of ATEG in a car. Modes: B, D – real waste heat recover (1); C – simple generation of energy (2); 3 – individual efficiency of ATEG as a heat engine; 4 – the moment of switching additional power of cooling system drives.*

In going to simple energy generation mode (C) the value η^* decreases to ~ 0.12 , but also essentially exceeds own efficiency of ATEG as heat engine ($\eta^{\text{ATEG}} \sim 0.03$) (3, Fig. 12). The mechanism of increase in effective efficiency $\eta^{\text{ATEG}*}$ in a car in B, C and D modes (Fig. 11) has a simple physical meaning [18]. As it is known, ATEG uses automotive waste heat which does not demand fuel consumption increase ($\delta A > 0$) per se [1]. The fuel consumption increase ($\delta A > 0$) is necessary only for indemnification of service expenses of ICE for transportation ($\Delta W_T > 0$) and cooling of ATEG cold junctions ($\Delta W_C^{\text{ATEG}} \geq 0$). These indemnifications are made at the expense of power increase of ICE which is heat engine with higher efficiency than ATEG ($\eta^{\text{ICE}} = 0.2 - 0.4$). Thus, the ratio $\eta^{\text{ATEG}*} > \eta^{\text{ATEG}}$ (1 – 3, Fig. 12) is a consequence of co-operative effect in “CAR + ATEG” system [18]. The above described power saving operation modes of ATEG (B, C, D, Fig. 11 and 12) are of practical interest. Thus, in all the modes (B, C, D, Fig. 11 and 12) the overall performance of ATEG can be raised at the expense of using new TEM with improved characteristics [13, 14].

4. Thermoelectric materials for ATEG

Fig. 13 shows the temperature dependences of dimensionless figure of merit ZT and the optimum band gap $E_g^{\text{opt}} \sim 8k_0T$ (here k_0 is the Boltzmann constant) of TEM suitable for ATEG. The

available temperature differences ΔT_0 for gasoline and diesel engines (b, d) and their real values (a, c), reduced because of thermal resistance of heat exchangers are shown.

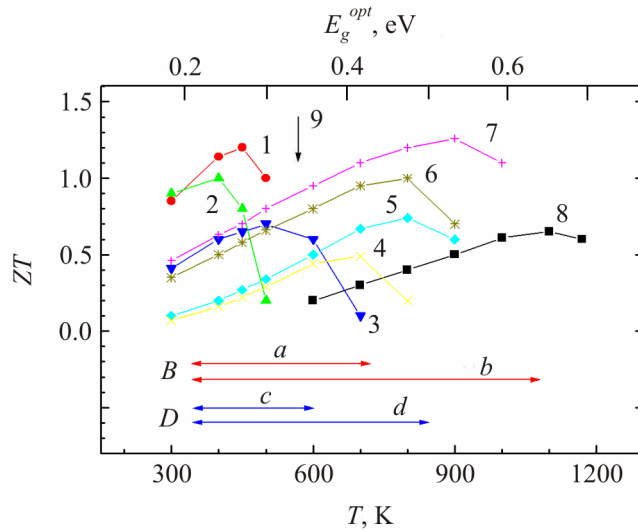


Fig. 13. The temperature dependences of dimensionless figure of merit ZT and optimum band gap E_g^{opt} of thermoelectric materials. 1 – $n\text{-Bi}_2\text{Te}_{2.7}\text{Se}_{0.3} < I, In >$ [29]; 2, 3 – $\text{Bi}_2\text{Te}_3 - \text{Sb}_2\text{Te}_3$ [30, 31]; 4 – $p\text{-Mg}_2\text{Si}_{0.4}\text{Sn}_{0.6}$ [23]; 5 – PbTe [31]; 6 – $n\text{-Mg}_2\text{Si}_{0.4}\text{Sn}_{0.6}$ [32]; 7 – $\text{AgPb}_x(\text{SbTe})_{1-x}$ (LAST) [31]; 8 – Ge-Si [31]; 9 – “dip”. Temperature differences on ATEG legs ΔT : b, d – available; a, c – real. The engines: a, b – gasoline; c, d – diesel.

From Fig. 13 it is evident that theories of Ioffe [19] and Okhotin [20] give essentially different criteria of searching for new thermoelectric materials for ATEGs. According to the Ioffe theory [19], for ATEG one needs materials with the energy gap $E_g^{opt} = 0.4 - 0.6$ eV ($T_{max} = 700 - 1100$ K) (d, b , Fig. 13). From [30, 31] it follows that exactly TEM with $E_g^{opt} = 0.4 - 0.6$ eV have been intensively developed by some specialists recently (5, 7, Fig. 13). However, with account of Lenz’s thermal rule (Fig. 9), the real temperature differences ΔT on ATEG legs will be lower – $E_g^{opt} \sim 0.25 - 0.4$ eV ($T_{max} = 400 - 700$ K) (a, c , Fig. 13) [20]. Such alloys with $E_g^{opt} \sim 0.25 - 0.4$ eV are not available now which is indicated by a “dip” in the range of temperatures $T = 400 - 700$ K existing on the family of curves $ZT = f(T)$ (marked by arrow 9, Fig. 13). From the TEM now available, the best fit for ATEG is given by alloys of the type Bi-Sb-Te-Se with $E_g \sim 0.2$ eV (2, Fig. 9) which are widely used by ATEG developers (Table 1). Recently, we have managed to increase maximum ZT of these alloys and shift it a little towards high temperatures by doping with In (1, Fig. 13) [29]. Among other materials suitable for ATEG, one can mention alloys based on Mg-Si-Sn with a low density $d \sim 3 \text{ g/cm}^3$ and energy gap $E_g = 0.5$ eV slightly above the optimum (6, 7, Fig. 13). The use of alloys based on Mg-Si-Sn can lead to essential decrease in the mass-factor m^* of ATEG [23, 32].

5. Discussion

Technology of automotive waste heat recovery using ATEG has been developed since the mid XX century in different countries [12]. However, an efficient ATEG has not been created to this day, which is generally attributable by ATEG developers to technical difficulties [1, 3-7]. The specified term (over 50 years) essentially exceeds the usual time for development of any technical product (several years). It shows that not only technical problems prevent from successful solution of ATEG problem [13-14].

In the present work it is established that automotive waste heat recovery using ATEG has rigid thermodynamic restrictions. This conclusion is based on the analysis of the results of experimental research on serial ATEG prototypes developed recently for motorcycles, cars and trucks [1, 3-7]. It is shown that in all the cases the experimental characteristics of ATEG appear to be essentially lower than the calculated ones [1, 3-7]. In this work, it is attributable to use in calculations of the Ioffe theory [19] that does not take into consideration high thermal resistance of heat exchangers on the “exhaust gas/exhaust pipe” boundary. As a result, the expected characteristics of ATEG have proved to be overestimated, and the prospects for using ATEG in cars overoptimistic [1, 3-7].

On the other hand, low experimental characteristics obtained in practice for modern ATEGs (Table 1) have been explained in the work by means of the Okhotin theory [20] that takes into account consistently high parasitic thermal resistance of ATEG heat exchangers on the “exhaust gas/exhaust pipe” boundary [2]. An additional factor reducing characteristics of ATEG is heterogeneity of ATEG and internal combustion engine as heat engines causing heat exchange difficulties in “CAR + ATEG” system. Besides, with a rise in W_e , a conflict of heat engines (internal combustion engine and ATEG) is developed in “CAR + ATEG” system, limiting growth of ATEG W_e and ΔW . As consequence, specific power of ATEG \hat{W}^{ATEG} is essentially inferior to that of other TEG types using liquid or solid heat-carriers (Table 2) [18].

Accordingly, the basic way for ATEG performance enhancement seems to be perfection of their heat exchangers (a reserve in specific power \hat{W}^{ATEG} up to 10 times and more) [18]. In this case, the increase in ZT of TEM, by our estimates, can be only of auxiliary nature now (a real reserve in \hat{W}^{ATEG} up to 2 times). This conclusion is proved by the literary data. Really, the greatest progress in ATEG performance enhancement has been achieved recently by improvement of ATEG heat exchangers design [3, 9, 11, and 26]. It would seem that now, alongside with perfection of heat exchangers, one should not rule out the use of power saving ATEG operation modes described in the present work (Fig. 11 and 12). Examples of using similar ATEG operation modes by the manufacturers can be found in the literature. It is demonstration of the efficiency of automotive waste heat recovery by an example of low-power ATEG $W_e \leq 0.2 \text{ kW}$) [6]. There were also proposals of replacement (full, or partial) of belt-driven automobile generators by more advanced ATEGs with increased efficiency $\eta^{\text{ATEG}*} > 0.1 - 0.5$ [10].

Conclusions

1. Installation of automotive thermoelectric generator (ATEG) on a car exhaust pipe creates essential thermodynamic restrictions on the value of generated net electric power W_e and recovered energy ΔW .
2. Therefore, the prospects of using high-power ATEGs for waste heat recovery and fuel consumption decrease in automobiles ($\Delta W > 0$, $\delta A < 0$) are essentially limited now.
3. Nevertheless, ATEGs of moderate power can be efficiently used in automobiles in waste heat recovery and simple energy generation modes, with regard to their high net efficiency ($\eta^{\text{ATEG}*} > 0.1 - 0.5$), increased due to cooperative effect in “CAR + ATEG” system.

References

1. C.B. Vining, The Limited Role for Thermoelectrics in Climate Crisis, *J. Thermoelectricity* **4**, 7-19 (2008).
2. V.A. Kirillin, V.V. Sychev, A.V. Sheindlin, *Technical Thermodynamics* (Moscow: Energiya, 1974), 448 p.

3. K.M. Saqr, M.K. Mansour, and M.N. Musa, Thermal Design of Automobile Exhaust-based Thermoelectric Generators: Objectivities and Challenges, *International J. Automotive Technology* 9(2), 155- 160 (2008).
4. D.M. Rowe, J. Smith, G. Thomas and G. Min, Weight Penalty Incurred in Thermoelectric Recovery of Automobile Exhaust Heat, *J. Electronic Materials* 40 (5), 784-788 (2011).
5. J. Lieb, S. Neugebauer, A. Eger, M. Linde, B. Masar, W. Stütz, The Thermoelectric Generator from BMW is Making Use of Waste Heat, *MTZ* 70 (4) 4-11 (2009).
6. A. Eger, M. Linde, *The BMW Group. Roadmap for the Application of Thermoelectric Generators* (San Diego, 2011), 23 p.
7. T. Kajikawa, Advances Thermoelectric Power Generation in Japan, *J. Thermoelectricity* 3, 5-18 (2011).
8. N. Espinosa, M. Lazard, L. Aixala, and H. Scherrer, Modeling Thermoelectric Generator Applied to Diesel Automotive Heat Recovery, *JEMS* 39(9), 1446-1455 (2010).
9. L.I. Anatychuk, O.J. Luste, and R.V. Kuz, Theoretical and Experimental Study of Thermoelectric Generators for Vehicles, *JEMS* 40 (5), 1326-1331 (2011).
10. J.W. Fairbanks, Development of Automotive Thermoelectric Generators and Air Conditioner / Heaters, *Proceedings of XIV International Forum on Thermoelectricity* (Moscow 17-20.05.2011), [On line: <http://forum.inst.cv.ua/>].
11. L.I. Anatychuk, R.V. Kuz, and Yu.Yu. Rozver, Thermoelectric Generators for Gasoline Engines, *J. Thermoelectricity* 2, 81-94 (2012).
12. E.M. Fajnzilber, L.M. Drabkin, Use of Heat of the Fulfilled Gases of Engines in the Thermoelectric Generator for a Power Source of Elements of an Electric Equipment of Cars, *Automotive Industry* 7, 9-10 (1996).
13. M.A. Korzhuev, Yu.V. Granatkina, Some Bottlenecks in the Automobile Thermoelectric Generators and a Search for New Materials to Eliminate Them, *J. Thermoelectricity* 1, 81-94 (2012).
14. M.A. Korzhuev, Conflict between Internal Combustion Engine and Thermoelectric Generator during Waste Heat Recovery in Cars, *Technical Physics Letters* 37 (4), 8-15 (2011).
15. M.A. Korzhuev, I.V. Katin, On the Placement of Thermoelectric Generators in Automobiles, *JEMS* 39 (9), 1390-1394 (2010).
16. M.A. Korzhuev, I.V. Katin, Reduced Life Time of the Vehicles by Installation of Thermoelectric Generator on Exhaust Pipe of the Internal Combustion Engine, *Chaos and Structures in Nonlinear Systems. Theory and Experiment* (Karaganda: E.A. Buketov State University, 2012), p. 250-254.
17. M.A. Korzhuev, I.V. Katin, Potential Economic Impacts of the Thermoelectric and Automobile Industries Associated with the Start of Mass Production of Automotive Thermoelectric Generators, *Thermoelectrics and their Applications*. Ed. by M.I. Fedorov and L.N. Lukyanova [On line:] <http://www.ioffe.ru/Thermolab>
18. M.A. Korzhuev, I.V. Katin, Some Features of Automotive Thermoelectric Generators (ATEG) and the Prospects for their Use in Transport, Thermoelectrics and their Applications. Ed. by M.I. Fedorov and L.N. Lukyanova [On line:] <http://www.ioffe.ru/Thermolab>
19. A.F. Ioffe, *Semiconductor Thermoelements* (Moscow-Leningrad: USSR Acad.Sci., 1960).
20. A.S. Okhotin, A.A. Efremov, V.S. Okhotin, and A.S. Pushkarsky, *Thermoelectric Generators* (Moscow: Atomizdat, 1976), 320 p.
21. B.S. Pozdnyakov, E.A. Koptelov, *Thermoelectric Power* (Moscow: Atomizdat, 1974), 264 p.
22. G.K. Kotyrlo, Yu.N. Lobunets, *Calculation and Designing of Thermoelectric Generators and Thermal Pumps. Handbook* (Kyiv: Naukova Dumka, 1980).
23. Yu.G. Manasian, *Ship's Thermoelectric Devices and Installations* (Leningrad: Sudostroyeniye,

- 1968), 284 p.
24. G.J. Snyder, Thermoelectric Power Generators. Efficiency and Compatibility, In: *Thermoelectric Handbook. Macro to Nano*. Ed: D.M. Rowe (CRC Press. Taylor & Francis.: Boca Raton, London, N.Y., 2006), P. 9.1-9.26.
25. L.I. Anatychuk, *Thermoelectricity. V. 2. Thermoelectric power converters* (Kyiv, Chernivtsi: Institute of Thermoelectricity, 2003), 376 p.
26. S.N. Plehanov, V.E. Novikov, and A.J. Terekov, Thermoelectricity in Russia – 250 years, *Thermoelectrics and their Applications*. Ed. by M.I. Fedorov and L.N. Lukyanova [On line:] <http://www.ioffe.ru/Thermolab>
27. *Academy of Sciences of the USSR. Personal structure (1724-1917). Book 1* (Moscow: Science, 1974), 480 p.
28. M. Gliozzi, *Storia della fisica* (Torino, Italy, 1965), 464 p.
29. T.E. Svechnikova, I.Yu. Nikhezina, M.A. Korzhuev, Thermoelectric Properties of $n\text{-Bi}_2\text{Te}_{2.7}\text{Se}_{0.3}$ - I , In Crystals, *Inorganic Materials* **47**(12), 1314-1318 (2011).
30. G.S. Nolas, J. Sharp, H.J. Goldsmid, *Thermoelectrics. Basic Principles and New Materials Developments* (Springer, Berlin, Heidelberg, N.Y, 2001).
31. J.R. Sootsman, D.Y. Chung, and M.G. Kanatzidis, New and Old Concepts in Thermoelectric Materials, *Angew. Chem. Int. Ed.* **48**, 8616-8639 (2009).
32. G.N. Isachenko, V.K. Zaitsev, M.I. Fedorov, T.A. Gurieva, and P.P. Konstantinov, Thermodynamic Properties of Solid Solutions between *p*-type Compounds Mg_2X ($X = Si, Ge, Sn$), *Thermoelectrics and their Applications*. Ed. by M.V. Vedernikov and L.N. Lukyanova (SPb: PIYF, 2010), P. 99-102.

Submitted 01.03.2013.

**V.R. Bilinsky-Slotylo, L.N. Vikhor, V.Ya. Mykhailovsky,
R.N. Mochernyuk, A.F. Semizorov**

Institute of Thermoelectricity NAS and MES of Ukraine,
1, Nauky Str., Chernivtsi, 58029, Ukraine

EFFICIENCY IMPROVEMENT OF GENERATOR MODULES BASED ON *CoSb* THROUGH USE OF SEGMENTED AND MULTI-STAGE STRUCTURES

Results of computer simulation of thermoelectric generator modules of homogeneous, segmented and functionally graded materials (FGM) based on CoSb are presented. It is shown that the efficiency of modules made of homogeneous materials reaches ~ 8 %, two-segmented materials – ~ 10 %, FGM – ~ 11 %. Studies on characteristics of two-stage modules have shown that bismuth telluride materials as the cold stage, and skutterudites as the hot stage improve the efficiency of thermoelectric converters to 12 %.

Key words: generator modules, heat recovery, thermoelectric energy converters, FGM.

Introduction

Waste heat from industrial production and internal combustion engines is one of the factors of environmental pollution. This heat recovery by direct thermal into electric energy conversion and its return to working cycles will improve the ecological situation considerably. Therefore, creation of efficient waste heat recuperators is a relevant economical and ecological task.

Thermoelectric method of direct thermal into electric energy conversion is rather attractive for recovery of waste heat from various industrial heating plants and engines. Absence of movable parts and possibility of operation under extreme conditions make thermoelectric generators highly reliable. The main factor restricting wide use of thermal generators in recuperators is low efficiency of thermal into electric energy conversion due to low dimensionless figure of merit of thermoelectric materials $ZT = \alpha^2 \cdot \sigma \cdot T / \kappa$ (where α – the Seebeck coefficient, T – temperature, σ – electric conductivity, κ – thermal conductivity).

This generates a need for new efficient, cheap and ecologically clean materials. During recent decade the researchers' attention has been attracted by skutterudites [1]. These are promising materials based on *CoSb* for a wide use in thermal generators operated at the hot side temperature to 773 K. They are characterized by rather high values of the Seebeck coefficient and electric conductivity. Two main techniques are employed for their figure of merit improvement [1]: the first technique is based on filling crystal lattice voids of *CoSb* materials with atoms of rare-earth elements by doping; the second technique is the use of doping to increase scattering on point defects, as to well as to control of charge carrier concentration.

Analysis of the results of experimental studies on thermoelectric characteristics of skutterudites [1-9] shows that to obtain *n*-type materials the most efficient doping impurities for *CoSb₃* are *In*, *Ga*, *Ni*, *Eu*, *Te*, *Se*, *S* [2-6], and for *p*-type materials with improved parameters it is reasonable to perform doping with several elements at once, namely *Fe* and *Yb*; *Fe*, *Yb* and *La*; *Ca* and *Fe*; *Ca* and *Mn* [7-9].

The purpose of this study is to evaluate the possibility of efficiency improvement of generator modules made of homogeneous, segmented, functionally graded and multi-stage structures through determination of the optimal doping level of skutterudite-based materials.

Design of thermoelectric modules from segmented and FGM legs

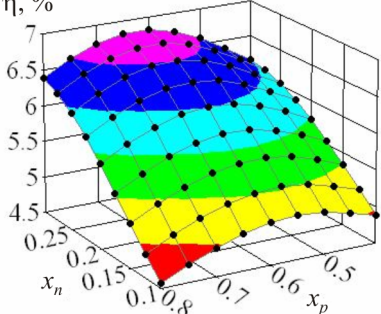
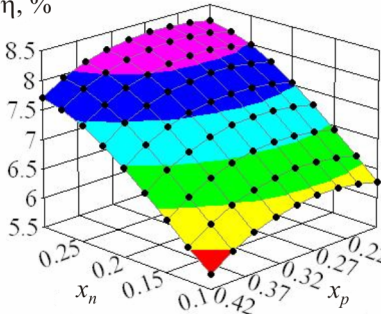
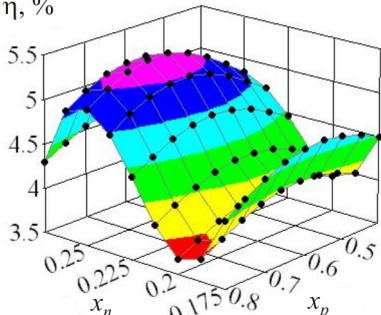
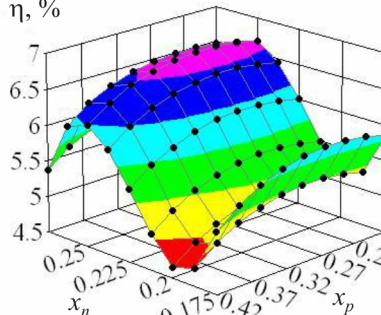
A search for optimal composition of *CoSb* based materials for homogeneous and segmented legs of thermoelectric modules was performed with the use of optimal control theory methods [10, 11]. In the calculations, the experimental dependences of thermoelectric parameters thermoEMF, electric conductivity and thermal conductivity on the temperature and concentration of doping impurities in *n*- and *p*-*CoSb* samples were employed. Calculations were performed for modules with the following parameters: number of thermoelements – 32 couples, height of legs – 5.6 mm, cross section areas of legs – $4 \times 4 \text{ mm}^2$. The values of contact resistances were assumed equal to $5 \cdot 10^{-5} \Omega \cdot \text{cm}^2$.

The results of calculation of characteristics of thermoelectric modules of homogeneous materials based on *CoSb* in the operating temperature range 323 – 773 K are represented in Table 1. Optimal concentrations of doping impurities x_n and x_p in leg materials are given whereby maximum efficiency η and the corresponding power P of modules are achieved, and dependences of efficiency on impurity concentration in the legs are given.

Table 1

Parameters of generator modules of homogeneous materials

*based on *CoSb*₃ at $T_h = 773 \text{ K}$, $T_c = 323 \text{ K}$*

<i>n</i> -type leg <i>p</i> -type leg	<i>Yb</i> _{<i>x</i>} <i>Fe</i> ₂ <i>Co</i> ₂ <i>Sb</i> ₁₂ (<i>x</i> = 0.4 – 0.8) [7]		<i>Yb</i> _{<i>x</i>} <i>La</i> _{0.85–<i>x</i>} <i>Fe</i> _{2.7} <i>Co</i> _{1.3} <i>Sb</i> ₁₂ (<i>x</i> = 0.17 – 0.42) [9]	
<i>Tl</i> _{0.1} <i>In</i> _{<i>x</i>} <i>Co</i> ₄ <i>Sb</i> ₁₂ (<i>x</i> = 0.1 – 0.3) [12]	$x_n = 0.3$	$P = 19 \text{ W}$	$x_n = 0.3$	$P = 22 \text{ W}$
	$x_p = 0.65$	$\eta = 6.8 \%$	$x_p = 0.25$	$\eta = 8.3 \%$
<i>CoSb</i> _{2.875–<i>x</i>} <i>Ge</i> _{0.125} <i>Te</i> _{<i>x</i>} (<i>x</i> = 0.175 – 0.275) [13]				
	$x_n = 0.25$	$P = 15 \text{ W}$	$x_n = 0.25$	$P = 18.4 \text{ W}$
	$x_p = 0.62$	$\eta = 5.35 \%$	$x_p = 0.25$	$\eta = 6.75 \%$
				

Analysis of data presented in Table 1 shows that dependences of module efficiency on the distribution of ytterbium impurity in materials for *p*-type legs, namely *La*_{0.85}*Fe*_{2.7}*Co*_{1.3}*Sb*₁₂ and *Fe*₂*Co*₂*Sb*₁₂, are characterized by a smooth change indicating to marginal impact of *p*-type leg doping component on module characteristics. As regards *n*-leg, dependences of module efficiency on indium

concentration in $Tl_{0.1}Co_4Sb_{12}$ are characterized by essential growth with increase in the concentration of doping component, whereas Te doping of $n\text{-}CoSb_{2.875}Ge_{0.125}$ leads to the appearance of two extrema.

Maximum efficiency $\eta = 8.3\%$ is exhibited by module of $n\text{-}Tl_{0.1}In_{0.3}Co_4Sb_{12}/p\text{-}Yb_{0.25}La_{0.6}Fe_{2.7}Co_{1.3}Sb_{12}$ materials. So, exactly these compounds are reasonable to be used for creation of functionally graded thermoelectric materials by formation of nonuniform impurity distribution.

Fig. 1 shows optimal distributions of indium concentration x_n along the leg of n -type $Tl_{0.1}In_xCo_4Sb_{12}$ and ytterbium concentration x_p along the leg of p -type $Yb_xLa_{0.85-x}Fe_{2.7}Co_{1.3}Sb_{12}$ determined by computer methods.

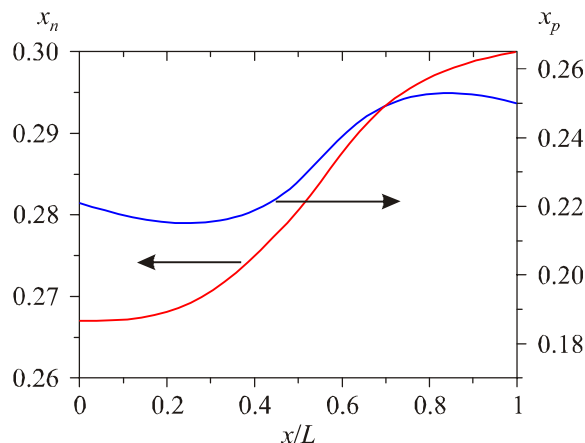


Fig. 1. Distributions of optimal impurity concentration along the height of legs for generator modules of FGM based on $n\text{-}Tl_{0.1}In_xCo_4Sb_{12}/p\text{-}Yb_xLa_{0.85-x}Fe_{2.7}Co_{1.3}Sb_{12}$. $x/L = 0$ corresponds to the cold side of leg.

Maximum efficiency of module with an optimal distribution of doping impurities in the legs (Fig. 1) with temperature difference $323 - 773$ K reaches 10.6% , and the generated electric power – 29.7 W.

The results of calculation of modules with two-segmented legs are presented in Table 2. Optimal materials for each segment of n - and p -legs are determined, as well as the heights of segments whereby maximum efficiency η of modules is achieved.

Table 2

Parameters of generator modules of two-segmented legs
 based on CoSb at $T_h = 773$ K, $T_c = 323$ K

n -type leg \ p -type leg	$Yb_xFe_2Co_2Sb_{12}$ $(x = 0.4 - 0.8)$ [7]		$Yb_xLa_{0.85-x}Fe_{2.7}Co_{1.3}Sb_{12}$ $(x = 0.17 - 0.42)$ [9]	
$Tl_{0.1}In_xCo_4Sb_{12}$ $(x = 0.1 - 0.3)$ [12]	$x_n^h = 0.3$	$\ell_n^h = 2.8$ mm	$x_n^h = 0.295$	$\ell_n^h = 2.9$ mm
	$x_n^c = 0.27$	$\ell_n^c = 2.8$ mm	$x_n^{ca} = 0.27$	$\ell_n^c = 2.7$ mm
$CoSb_{2.875-x}Ge_{0.125}Te_x$ $(x = 0.175 - 0.275)$ [13]	$x_p^h = 0.68$	$\ell_p^h = 2.8$ mm	$x_p^h = 0.25$	$\ell_p^h = 2.7$ mm
	$x_p^c = 0.62$	$\ell_p^c = 2.8$ mm	$x_p^c = 0.218$	$\ell_p^c = 2.9$ mm
		$P = 27$ W	$\eta = 9.1\%$	$P = 28.8$ W
				$\eta = 10.3\%$
	$x_n^h = 0.25$	$\ell_n^h = 2.8$ mm	$x_n^h = 0.25$	$\ell_n^h = 2.9$ mm
	$x_n^c = 0.238$	$\ell_n^c = 2.8$ mm	$x_n^c = 0.24$	$\ell_n^c = 2.7$ mm
	$x_p^h = 0.7$	$\ell_p^h = 2.8$ mm	$x_p^h = 0.234$	$\ell_p^h = 2.7$ mm
	$x_p^c = 0.632$	$\ell_p^c = 2.8$ mm	$x_p^c = 0.202$	$\ell_p^c = 2.9$ mm
		$P = 22.6$ W	$\eta = 7.35\%$	$P = 24.6$ W
				$\eta = 8.5\%$

For modules of homogeneous materials and double-segmented legs the highest efficiency is achieved with the use of *n*-type $Tl_{0.1}In_xCo_4Sb_{12}$ and *p*-type $Yb_xLa_{0.85-x}Fe_{2.7}Co_{1.3}Sb_{12}$ (Table 2).

Research on multi-stage generator modules

Optimal materials were selected for each stage using optimal control theory methods such that the cold and hot stages were characterized by maximum efficiency in the temperature range 323 – 523 K and 523 – 773 K, respectively. Design calculation of two-stage modules 40 × 40 mm² (Table 3) was made for series connection of the cold and hot stages at thermal and electric compatibility of stages.

In the calculations, experimental concentration-temperature dependences of thermoelectric parameters of *BiTe* materials were employed [14]. In module № 1 skutterudite based materials were selected for both stages. In modules № 2 and № 3 for the low-temperature stage use was made of *Bi-Te*. In Table 3, the values of electric conductivity σ of *Bi-Te* based materials at 300 K and impurity concentrations in skutterudites, optimal for each stage, are presented, as well as power and efficiency values of modules are calculated.

Table 3
Parameters of two-stage generator modules of CoSb₃ based materials
at T_h = 773 K, T_c = 323 K

№	Parameter	Parameter value		
		Module № 1	Module № 2	Module № 3
1.	Cold stage leg materials	<i>n</i> -type leg $Tl_{0.1}In_{0.27}Co_4Sb_{12}$	$(Bi_2Te_3)_{0.90}(Sb_2Te_3)_{0.05}(Sb_2Se_3)_{0.05}$, doped with I ₂ , $\sigma_0^n = 1365 \Omega^{-1}\text{cm}^{-1}$	
		<i>p</i> -type leg $Yb_{0.196}La_{0.654}Fe_{2.7-}Co_{1.3}Sb_{12}$	$(Bi_2Te_3)_{0.25}(Sb_2Te_3)_{0.72}(Sb_2Se_3)_{0.03}$, doped with Pb, $\sigma_0^p = 1570 \Omega^{-1}\text{cm}^{-1}$	
2.	Hot stage leg materials	<i>n</i> -type leg $Tl_{0.1}In_{0.295}Co_4Sb_{12}$		
		<i>p</i> -type leg $Yb_{0.24}La_{0.61}Fe_{2.7}Co_{1.3}Sb_{12}$		
3.	Cross-sectional area of cold and hot stage legs, mm ²	1.8 × 4.3		
4.	The height of cold stage leg, mm	2.9	2.7	3
5.	The height of hot stage leg, mm	3	3.3	3
6.	The number of leg couples of cold and hot stages	48		
7.	Electric power P, W	14.1	13.8	16
8.	Voltage U, V	4.1	4.4	3.6
9.	Current I, A	3.5	3.2	4.4
10.	Efficiency η, %	10.2	11.2	11.9

From the data presented in Table 3 it is apparent that the efficiency of generator module where *CoSb* based materials are selected for both stages, reaches ~ 10.2 % (module № 1), which is inferior to *BiTe* based materials selected for the cold stage ($\eta \approx 11.2 \%$, module № 2). In this case, the electric

compatibility of stages is assured by optimal height values of thermoelements in each stage. The use of parallel-in-series connection of cold stage thermoelements (module № 3) allows improving module efficiency nearly to 12 %. Dependences of efficiency and generated electric power of two-stage modules based on $Bi_2Te_3/CoSb_3$ on their hot side temperature are presented in Fig. 2.

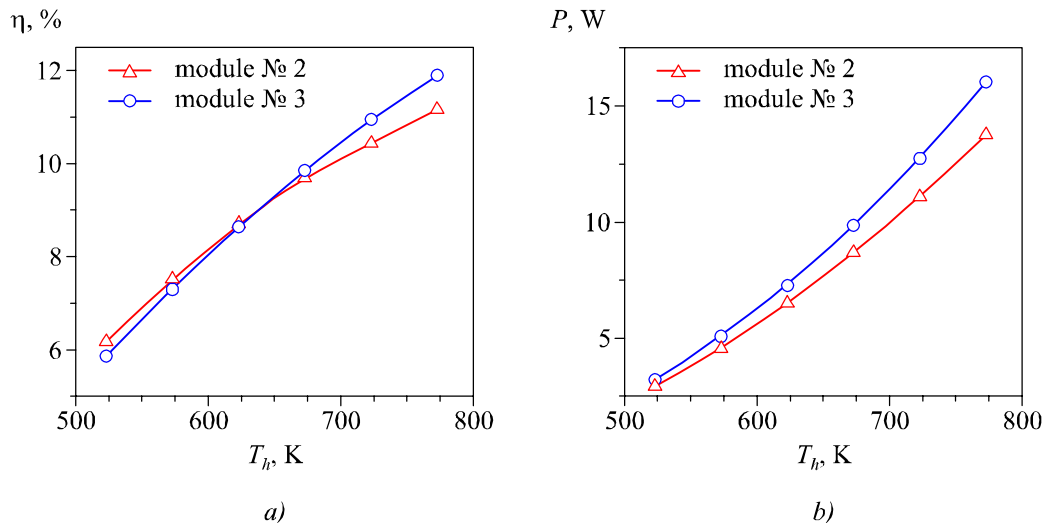


Fig. 2. Dependences of efficiency η (a) and electric power P (b) of two-stage modules based on $Bi_2Te_3/CoSb_3$ on their hot side temperature T_h at cold temperature $T_c = 323$ K.

At hot side temperature 773 K the efficiency of module № 3 ($\eta = 11.9 \%$) is higher than that of module № 2 ($\eta = 11.16 \%$). With a reduction in temperature T_h , the efficiency drops and at $T_h = 623$ K the efficiency of both modules is identical, and with further reduction of hot side temperature, the efficiency of module № 2 is somewhat higher.

From the data presented above it is evident that with the use of similar materials for stages and segments the efficiency of two-stage modules actually does not exceed the efficiency of modules with double-segmented legs.

Conclusions

Computer simulation methods were used to determine optimal parameters of materials for segments and optimal inhomogeneity functions of functionally graded materials whereby maximum efficiency of thermoelectric generator modules made of skutterudites is achieved.

The efficiency of modules in the operating temperature range 323 – 773 K lies within 5 – 8 % for modules of homogeneous materials, 7 – 10 % for modules of two-segmented legs and approaches 11 % for FGM modules. Using in $CoSb$ based modules of two-segmented legs instead of homogeneous materials allows increasing their efficiency by a factor of 1.2 – 1.4.

Research on multi-stage structures has shown that using $BiTe$ materials in the cold stage and skutterudites in the hot stage allows assuring the efficiency of thermoelectric conversion of thermal energy on the level of 11 – 12 %.

References

1. C. Uher, Skutterudite-Based Thermoelectrics. *Thermoelectrics Handbook. Macro to Nano*. Edited by D.M. Rowe (CRC Press, 2006), P.34-1–34-13.

2. A. Harnwunggmoung, K. Kurosaki, T. Plirdpring, T. Sugahara, Yu. Ohish, H. Muta, and Sh. Yamanaka, Thermoelectric properties of Ga-added $CoSb_3$ based Skutterudites, *J. Applied Physics* **110**, 013521 – 013521-5 (2011).
3. S.-Ch. Ur, Il-H. Kim, Electronic Transport Properties of Ni-doped $CoSb_3$ Prepared by Hot Pressing, *J. Korean Physical Society* **55** (3), 942-946 (2009).
4. Y.Z. Pei, S.Q. Bai, X.Y. Zhao, W. Zhang and L.D. Chen, Thermoelectric Properties of $Eu_xCo_4Sb_{12}$ Filled Skutterudites, *Solid State Sciences* **10** (10), 1422-1428 (2008).
5. B. Duan, P. Zhai, L. Liu, Q. Zhang, and X. Ruan, Beneficial Effect of Se Substitution on Thermoelectric Properties of $Co_4Sb_{11.9-x}Te_xSe_{0.1}$ Skutterudites, *J. Solid State Chemistry* **193**, 8-12 (2012).
6. B. Duan, P. Zhai, L. Liu, and Q. Zhang, Enhanced Thermoelectric Performance in Sulfur-Doped $Co_4Sb_{11.9-x}Te_xS_{0.1}$ Skutterudites, *Materials Letters* **79**, 69-71 (2012).
7. Ch. Zhou, D. Morelli, X. Zhou, G. Wang, and C. Uher, Thermoelectric Properties of *p*-type Yb -filled Skutterudite $Yb_xFe_yCo_{4-y}Sb_{12}$, *Intermetallics* **19** (10), 1390-1393 (2011).
8. K.-H. Park, Il-H. Kim, Thermoelectric Properties of Ca-filled $CoSb_3$ -based Skutterudites Synthesized by Mechanical Alloying, *J. Electronic Materials* **40** (5), 493-498 (2011).
9. L. Zhou, P. Qiu, C. Uher, X. Shi, and L. Chen, Thermoelectric Properties of *p*-type $Yb_xLa_yFe_{2.7}Co_{1.3}Sb_{12}$ Double-Filled Skutterudites, *Intermetallics* **32**, 209-213 (2013).
10. L.M. Vikhor, Computer design of thermoelectric generator modules, *Journal of Thermoelectricity* **2**, 60-67 (2005).
11. L.I. Anatychuk, L.N. Vikhor, *Thermoelectricity. Vol. IV. Functionally Graded Thermoelectric Materials* (Chernivtsi: Bukrek, 2012), 180 p.
12. A. Harnwunggmoung, K. Kurosaki, A. Kosuga, M. Ishimaru, Th. Plirdpring, R. Yimnirun, J. Jutimoosi, S. Rujirawat, Yu. Ohishi, H. Muta, and Sh. Yamanaka, Enhancement of Thermoelectric Properties of $CoSb_3$ -based Skutterudites by Double Filling of *Tl* and *In*, *J. Applied Physics* **112**, 043509 – 043509-6 (2012).
13. X. Su, H. Li, Q. Guo, X. Tang, Q. Zhang, and C. Uher, Structure and Thermoelectric Properties of *Te*- and *Ge*-doped Skutterudites $CoSb_{2.875-x}Ge_{0.125}Te_x$, *J. Electronic Materials* **40** (5), 1286-1291 (2011).
14. L.N. Vikhor, L.I. Anatychuk, Generator Modules of Segmented Thermoelements, *Energy Conversion and Management* **50**, 2366-2372 (2009).

Submitted 24.01.2013.

A.A. Nazarenko

A.A. Nazarenko

Moscow State Technical University of Radio Engineering,
Electronics and Automation, 78, Vernadsky Prospect,
Moscow, 119454, Russia

RELIABILITY ENHANCEMENT OF THERMOELECTRIC COOLERS USING POLYMER VACUUM COATINGS

The effect of parylene protective coatings on the durability of miniature thermoelectric coolers (TECs) under high-temperature storage in the air and high humidity, and under the influence of aggressive solutions was studied. According to the results of research the type of parylene was selected and optimal thickness of parylene coating was determined. TECs were tested according to standard MIL-STD-883F methods, and it was established that parylene coatings increase TEC reliability, namely parameter stability under high-temperature storage (125°C) and humidity is improved, structural elements are protected from the influence of aggressive media. It is shown that parylene coating does not noticeably change the thermophysical characteristics of TECs: for instance, the maximum temperature difference ΔT_{\max} of a single-stage TEC is reduced by only 0.3°C as compared to the initial values.

Key words: thermoelectric coolers, reliability, polymer coating, chemically active environment.

Introduction

Performance reliability of TECs is essentially restricted with use in the ordinary air atmosphere and aggressive media due to interaction of structural elements with the environment, which reduces the efficiency of module operation because of problems related to corrosion or moisture condensation with formation of “thermal bridge” between the hot and cold TEC junctions [1].

An efficient method of TECs protection from condensate formation is sealing by application of continuous polymer coating on the lateral surfaces of TECs (Fig. 1).

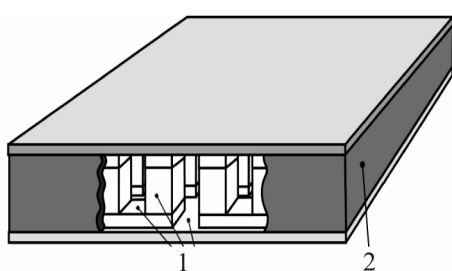


Fig. 1. TEC with double encapsulation by UR-231 varnish (1) and VGO-1 sealant (2).

For these purposes, multiple application of silicone, epoxy or varnish coatings is used to form a layer $50\dots80\ \mu\text{m}$ thick, for instance, two-component coating of UR-231 varnish and VGO-1 silicone sealant [4]. However, such coatings can be destroyed on exposure to repeated temperature cycling. Moreover, heat losses along the perimeter reduce considerably TEC characteristics. In particular, the value of maximum temperature difference ΔT_{\max} of a single-stage TEC is reduced by 3 to 5 K. For protection of miniature TECs this method is impractical.

Company RMT Ltd has developed and patented corrosion protection method for TECs, including miniature and multi-stage ones (Russian Federation patent № 41549). The internal and external surfaces of TECs are coated with a continuous parylene

protective film (Fig. 2). However, this patent does not indicate the specific type of parylene coating and its thickness.

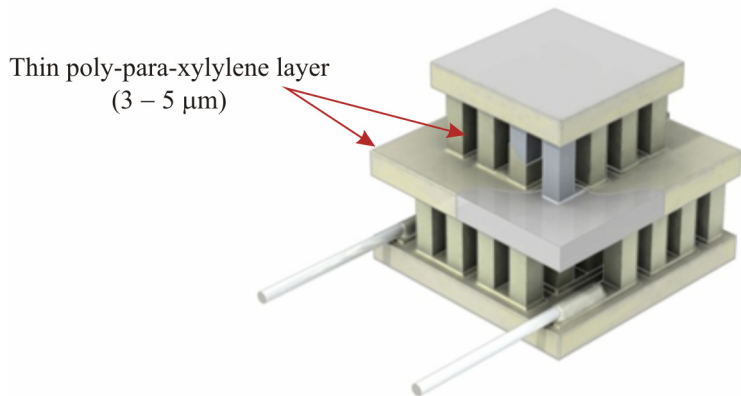


Fig. 2. Poly-para-xylylene polymer coating.

To the most efficient vacuum parylene coatings one can refer polymer coatings based on poly-para-xylylene (*Parylen N*), poly-dichloro-para-xylylene (*Parylen D*) and fluoropolymers (*Parylen F*), that are deposited from gas phase (without passing through the liquid state) at normal or reduced (to 0 °C) temperature, and coating formation does not require curing. High thickness uniformity of coatings, including sharp edges and narrow (< 1 µm) gaps, make them indispensable for complex-contoured surfaces. These factors provide poly-para-xylylene coatings (in the range of thickness from 3 to 10 µm) with protective properties as good as or superior to coatings based on epoxy, silicone and polyurethane resins 50 to 80 µm thick. Vacuum coatings assure reliable operation of protected TECs under conditions of increased humidity, temperature variation in a wide range (from – 80 to + 100 °C), as well as the influence of biological, chemical and other factors [3].

The purpose of this work is to select the type of parylene coating and determine its optimal thickness according to the results of studying the resistance of miniature TECs to environmental impacts.

Selection of coating type and experimental procedure

Analysis of the physical properties of *Parylen N*, *Parylen D* and *Parylen F* polymers (Table 1) has revealed that the best parameters as compared to other poly-p-xylylenes are possessed by *Parylen F* which offers the lowest moisture permeability (< 0.0009 g/(cm²·h)) and is the most thermally stable material (~ 400 °C in the air). However, high cost of material makes it economically unsound for use in large-scale production. *Parylen F* is reasonable to be used for encapsulation of high-temperature TECs, as well as for special missions requiring parameter stability under increased environmental impact.

Parylen N has the lowest thermal stability (80 °C) which restricts its application area and does not conform to test conditions.

Parylen D has moisture permeability 0.1 g/(cm²·h) and thermal stability 150 °C which meets the requirements of test performed in the framework of this paper. Therefore, for studying the protective properties of coatings we fixed on *Parylen D*.

For protective polymer synthesis in low vacuum as the original substance we used di-chlorinated [2, 2]-paracyclofan which is a fine crystalline white powder with the density of 1.42 g/cm³ and melting temperature ~ 310...330 °C [6].

As long as adhesion of poly-dichloro-p-xylylene (*Parylen D*) film to the surface of

heterostructure to a large extent depends on the substitutes in the benzene ring of paracyclofan structure and the material of coated surface, in the formation of protective *Parylen D* layer the surface is pre-treated by silane vapours [5].

Table 1
Basic properties of poly-para-xylylene and poly-dichloro-para-xylylene

Parameter	Value		
	<i>Parylen N</i>	<i>Parylen D</i>	<i>Parylen F</i>
Dielectric permittivity at 60 Hz	2.65	2.84	2.28
Electric strength, kV/mm	240	145	141
Bulk resistivity under standard conditions, Ohm·m	10^{15}	$8 \cdot 10^{14}$	$6 \cdot 10^{14}$
Dielectric loss tangent at 60 Hz	0.0002	0.003	0.003
Melting temperature, °C	400	310 – 330	270
Vitrification temperature, °C	60 – 70	110	140
Tensile strength, MPa	63	42	42
Thermal stability in the atmosphere, °C	80 – 90	140 – 150	380 – 400
Water absorption during 24 hours, %	0.01	0.06	0.02
Moisture permeability, g/(cm ² ·h)	0.3	0.1	0.009

Formation of *Parylen D* coating takes place during two-stage growth: application of intermediate silane adhesion layer 10 nm thick and deposition of basic poly-p-xylylene protective layer at constant sublimation temperature of paracyclofan original substance.

Parylen D coating was applied by gas-phase deposition method. The deposition took place at a pressure of 8 Pa in closed sublimator – pyrolysis reactor – deposition chamber system and device surface temperature ~ 40 °C for 45 min [5].

Thermoelectric coolers 1MD04-012, 1ML06-029 and 1MC06-060 manufactured by RMT Ltd, with their basic operating parameters given in Table 2, were used as experimental samples for the application of protective polymer coatings.

Table 2
Basic operating parameters of TECs

TEC type	ΔT_{\max} , K	Q_{\max} , W	I_{\max} , A	U_{\max} , V
1ML06-029-09	71	3.85	1	3.55
1MD04-012-07	72	0.38	0.8	0.85
1MC06-060-10	71	6.05	1.5	7.4

Criterion for estimation of the environmental resistance of thermoelectric modules is taken to be a change on environmental exposure in electric resistance R and thermoelectric figure of merit Z by not more than 5 % of the initially measured values. This criterion is used by RMT company and corresponds to reliability standards developed by Telcordia corporation. Requirements to TECs are formulated in Telcordia document GR-468-CORE (Generic Reliability Assurance Requirements for Optoelectronic Devices Used in Telecommunications Equipment) comprising general requirements to reliability of optoelectronic devices and components, as well as their test methods.

TEC test methods set forth in Telcordia GR-468-CORE are based on the US military standard MIL-STD-883F. This standard formulates methods for testing microelectronic products for military and aerospace applications.

The measurements were performed on Z -meter of DX4165 series manufactured by RMT Ltd.

To estimate the proposed method of TEC protection from aggressive media and humidity, the following tests were performed:

- high-temperature storage in the air;
- exposure to chemical environment;
- humidity test.

Test results

Check of TEC thermophysical parameters. Prior to application of parylene coatings on 1MC06-060-10 modules, maximum temperature difference (ΔT_{\max}) was measured in vacuum, in conformity with requirements of TU8420 001 34609988 12 "Performance specifications. TEC", which was on the average 70.1 °C. Measurements were repeated after application on these TECs of *Parylen D* coatings 5 µm thick, which averaged $\Delta T_{\max} = 69.8$ °C, i.e. ΔT_{\max} reduction made 0.3 °C.

High-temperature storage. To determine high-temperature durability of TEC with *Parylen D* protective coating 0, 3 and 5 µm thick, three lots of TEC 1MD04-012-07, 11 modules in each lot, were used. TECs were stored in the air at 125 °C for 1100 hours (accelerated test) instead of 85 °C/2000 hours recommended by Telcordia GR-468-CORE.

Prior to and after test the samples were subject to visual inspection and R and Z measurement. The results of measurement prior to and after test are represented in Table 3.

Table 3

*Results of testing modules IML04-012-07 for storage
 in the air at 125 °C for 1100 hours*

Coating thickness	Electric resistance R , Ω		Relative change, %	Thermoelectric figure of merit $Z \times 1000$, 1/K		Relative change, %
	Prior to test (R_1)	After test (R_2)		Prior to test (Z_1)	After test (Z_2)	
Without coating	1.61	1.66	3.11	2.67	2.60	-2.62
3 µm	1.62	1.65	1.85	2.67	2.63	-1.50
5 µm	1.62	1.65	1.85	2.66	2.63	-1.13

Figs. 3 and 4 show the plots of change in the basic parameters of thermoelectric coolers. For all TEC lots a change in R and Z as compared to the initial values did not exceed 5 % of criterion. From the plots it is seen that the output parameters of thermoelectric coolers with parylene coatings are more stable than parameters of modules without coating. Therefore, poly-dichloro-para-xyllylene coating contributes to stabilization of module parameters in the process of high-temperature storage. Probably it is due to protection of thermoelectric materials and contact coatings from thermal oxidation.

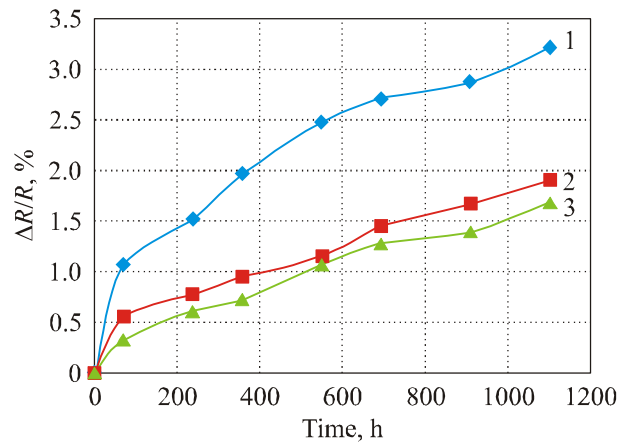


Fig. 3. Relative change in electric resistance with time.
Coating thickness: 1 – without coating; 2 – 3 μm ; 3 – 5 μm .

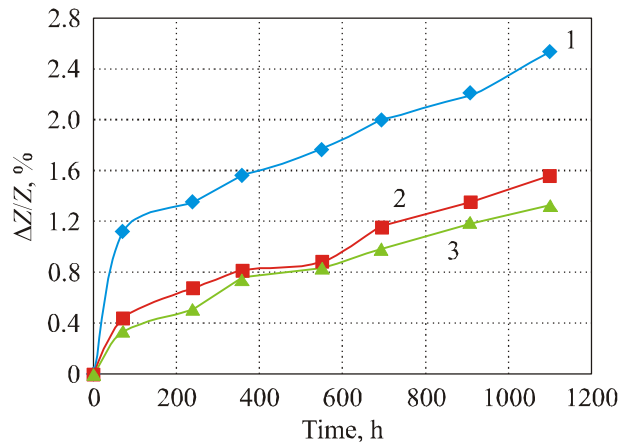


Fig. 4. Relative change in thermoelectric figure of merit with time.
Coating thickness: 1 – without coating; 2 – 3 μm ; 3 – 5 μm .

Exposure to chemical environment. Testing of TEC in chemically active environment was performed according to MIL-STD-883F, method 1009.8. To determine the efficiency of using poly-dichloro-para-xyllylene coatings of various thicknesses for TEC protection, we used more severe conditions than in MIL-STD-883F: 10 % aqueous solution of NaOH instead of 3 %, test duration was increased from 240 to 336 hours. After testing, the samples were subject to visual inspection and parameter measurement by the criteria described above.

Testing was performed on TEC samples 1MD04-012-07 coated with vacuum films *Parylen D* 3 and 5 μm thick by holding in 10 % solution of sodium hydroxide (NaOH) for 336 hours.

The appearance of TEC after testing is represented in Fig. 5. It is seen that the legs of thermoelectric coolers without parylene were destroyed in NaOH solution. At the same time, the legs of modules with 5 μm vacuum coating had no defects.

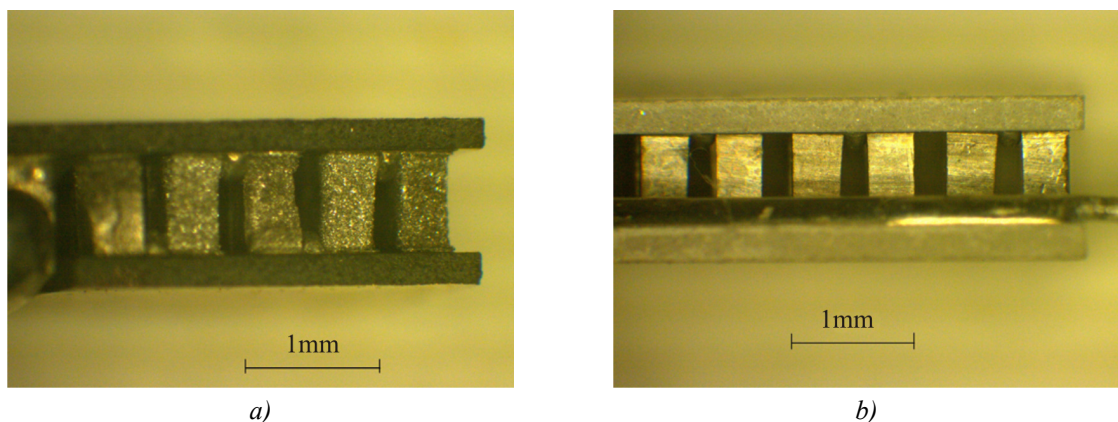


Fig. 5. Appearance of TEC series 1MD04-012 on exposure to 10 % solution of sodium hydroxide (NaOH) for 336 hours: a) without coating, b) with Parylen D vacuum sealing coating 5 μm thick.

Results of measuring TEC parameters are represented in Table 4.

Table 4

Results of measuring parameters of 1MD04-012-07 modules prior to and after holding in 10 % NaOH solution

Coating thickness	Electric resistance R , Ω		Relative change, %	Thermoelectric figure of merit $Z \times 1000$ 1/K		Relative change, %
	Prior to test (R_1)	After test (R_2)		Prior to test (Z_1)	After test (Z_2)	
Without coating	1.11	2.97	167.57	2.53	0.96	-62.01
3 μm	1.17	1.75	49.57	2.52	2.10	-16.40
5 μm	1.11	1.17	4.98	2.49	2.38	-4.42

Figs. 6 and 7 represent plots of change in electric resistance and thermoelectric figure of merit of TEC in the course of holding in 10 % NaOH solution.

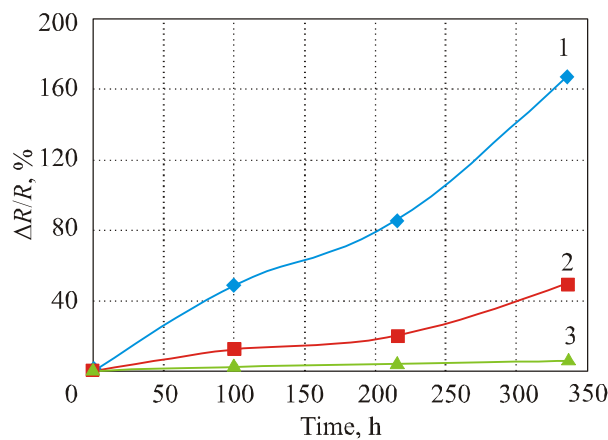


Fig. 6. Dependences of relative change in electric resistance R of thermoelectric coolers on the time of storage in 10 % NaOH solution. Coating thickness: 1 – without coating; 2 – 3 μm ; 3 – 5 μm .

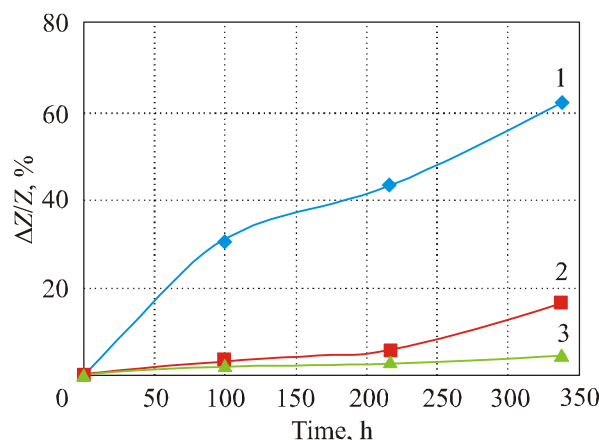


Fig. 7. Dependences of relative change in thermoelectric figure of merit Z of 1MD04-012-07 modules on the time of storage in 10 % NaOH solution.

Coating thickness: 1 – without coating; 2 – 3 μm; 3 – 5 μm.

Results of visual inspection and electrical measurement show that TECs without parylene coating did not withstand this test. Parameters of thermoelectric coolers with *Parylen D* coating proved to be more stable, and changes in both parameters (R and Z) of TECs with 3 μm *Parylen D* coating exceeded 5 % criterion, and with 5 μm did not go beyond the limits of criterion.

During the second part of testing for resistance to chemical environment we estimated the influence of 10% NaC aqueous solution on TEC under electric load. Testing was performed on TEC samples MC06-060-10 without coating and with *Parylen D* coating. The samples were placed into a vessel with a salt solution, and voltage 3.7 V ($\frac{1}{2} U_{\max}$) was applied for 336 hours. The results of testing are represented in Table 5.

In the course of testing the legs of modules without coating were destroyed completely. Parameters of thermoelectric coolers with vacuum polymer coating 3 μm thick went beyond the limits of 5 % criterion, while those with coating 5 μm thick remained within 5 %.

Table 5

Results of testing IMC06-060-10 modules for resistance to 10 % NaCl solution at 3.7 V

Coating thickness	Electric resistance R , Ω		Relative change, %	Thermoelectric figure of merit $Z \times 1000$, 1/K		Relative change, %
	Prior to test (R_1)	After test (R_2)		Prior to test (Z_1)	After test (Z_2)	
Without coating	1.15	–	–	2.56	–	–
3 μm	1.14	1.23	7.89	2.58	2.40	-7.16
5 μm	1.15	1.20	4.34	2.55	2.43	-4.71

Humidity test. This test was performed in conformity with MIL-STD-883F, method 1004.7, with a view to determine the efficiency of TEC humidity protection with *Parylen D*. For testing, as before, we selected 3 lots of samples 1MD04-012-07, with *Parylen D* coating 3 μm , 5 μm and without coating. Graphic representation of humidity resistance test is shown in Fig. 8.

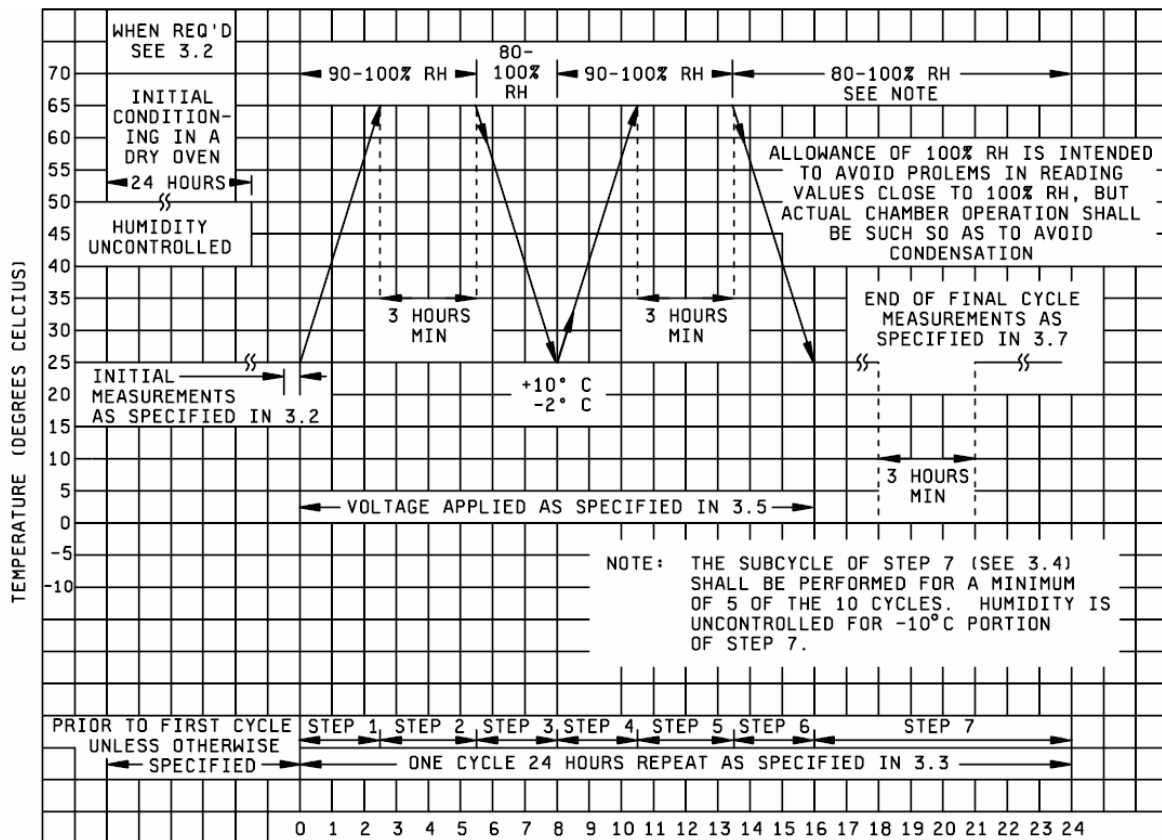


Fig. 8. Graphic representation of humidity test.

Results of TEC humidity test are represented in Table 6.

Table 6
Results of humidity test of IMD04-12-07 modules

Coating thickness	Electric resistance R, Ω		Relative change, %	Thermoelectric figure of merit $Z \times 1000, 1/K$		Relative change, %
	Prior to test (R_1)	After test (R_2)		$(R_2 - R_1)/R_1 \cdot 100$	Prior to test (Z_1)	
Without coating	1.12	1.14	1.79	2.58	2.54	-1.62
3 μm	1.15	1.16	0.79	2.52	2.49	-1.15
5 μm	1.15	1.157	0.61	2.59	2.57	-0.74

From the test results it follows that all the modules have passed the test and their parameters have remained within 5 %. It should be noted that TECs with *Parylen D* coating have more stable parameters as compared to modules without coating.

Conclusions

The durability of TECs with *Parylen D* coating under high-temperature storage in the air has been investigated. It has been shown that, unlike TECs without coating, the basic parameters of

thermoelectric coolers with poly-dichloro-paraxylylene remain more stable under long (over 1000 hours) high-temperature storage (125 °C).

It has been established that thermoelectric coolers without protective coatings undergo strong destruction on exposure to aggressive media (10 % $NaCl$, 10 % $NaOH$). It has been noted that poly-dichloro-paraxylylene coating can protect TECs from chemical attack with coating thickness 5 μm .

TECs have been tested for reliability under humidity conditions, and it has been noted that parameter divergence of all the coolers does not exceed 5 %. In so doing, the greatest stability of properties is shown by coolers with a coating 5 μm thick.

Parylen D coating has no essential effect on the thermophysical properties of TECs, in particular, the value of maximum temperature difference ΔT_{max} of a single-stage TEC is reduced by 0.3 °C.

Based on the results of the research it can be concluded that for the efficient protection and stabilization of TEC parameters the thickness of *Parylen D* coating must be 5 μm .

References

1. L.I. Anatychuk, *Thermoelements and Thermoelectric Devices. Handbook*. (Kyiv: Naukova Dumka, 1979), 768 p.
2. A.L. Vainer, *Multistage Thermoelectric Cold Sources* (Moscow: Soviet Radio, 1976), 136 p.
3. V.I. Urazayev, *Moisture Protection of Printed Circuit Board Assemblies* (Tekhnosphera, 2006), 167 p.
4. Yu.I. Shtern, Thermoelectric Modules Encapsulation Technology, *Materialy Elektronnoi Tekhniki* **4** (2008).
5. A.N. Lantsev, P.A. Luchnikov, A.A. Nazarenko, Research on Structural and Electrical Properties of Polymer Composite Films Using Electret-Thermal Analysis Methoda, *Siberian J. of Science* **4** (5), 34-41 (2012).
6. I.E. Kardash, A.V. Pebalk, A.N. Pravednikov, Chemistry and Application of Poly-p-xlenes, *Itogi Nauki i Tekhniki. Series: Chemistry and Technology of High-Molecular Compounds* (Moscow, VINITI, 1984), Vol.19, pp.66-150.

Submitted 15.05.2013.

A.V. Simkin, A.V. Biryukov, N.I. Repnikov.,O.N. Ivanov

Belgorod State National Research University,
85, Pobedy Str., Belgorod, 308015, Russia

RELIABILITY TEST OF GENERATOR THERMOPILES MADE WITH THE USE OF ARC PLASMA SPRAYING METHOD

Long term test of generator thermopile samples for temperature cycling on their heat spreaders was performed. Depending on the number of cycles, changes in the basic technical characteristics of modules were traced and analyzed: electric power under optimal load, internal resistance and electromotive force (EMF) of thermopiles on achievement of design temperature difference. According to test results, amendments were introduced into thermopile manufacturing technique.

Key words: generator thermopiles, reliability, temperature cycling, characteristics of thermopile, mechanical destruction.

Introduction

Performance reliability of a thermoelectric generator (TEG) is defined as the probability of failure-free operation of installation for a specified time, for instance, its service life. In assessing the suitability and prospects, especially of self-contained thermoelectric installation, reliability is a prime consideration, as long as failure of independent marine or space power generation system can have grave consequences [1].

The basic structural unit of any TEG defining service life, time to failure and to a great degree the cost of the entire device is a thermoelectric module consisting of generator thermopiles. TEGs generally comprise tens and hundreds of generator thermopiles and even a greater number of junctions and connections each of which can cause TEG malfunction.

Heating and cooling of thermoelements can create large temperature gradients on contact layers of legs, hence, mechanical stresses causing formation of cracks, lamination and other thermoelectric material damages. It can drastically increase contact electric resistance and, thus, reduce the power and efficiency of thermoelements [1].

The purpose of this work was to study the reliability of a generator thermopile, where connection of basic elements, i.e. semiconductor legs, was done by arc plasma spraying method. Reliability was determined by carrying out long term test of generator thermopile samples for temperature cycling on heat spreaders. All samples under study were made by a unified technique. In so doing, the design employed semiconductor legs of bismuth telluride obtained by zone recrystallization and powder metallurgy methods. The reasons for a change in the basic technical characteristics of a generator thermopile in the course of the test were investigated.

Experimental procedure and samples

To perform the experiment, small lots of samples (4 – 5 pcs of each type) of generator thermopiles of the type TGB-P-NT-6 were made with extruded legs and TGB-P-NT-8 with the legs obtained by zone melting and hot pressing methods.

Design of generator thermopile samples is similar to that of thermopiles 7.5/2.5, described in [2], but has a variety of improvements (see Fig. 1).

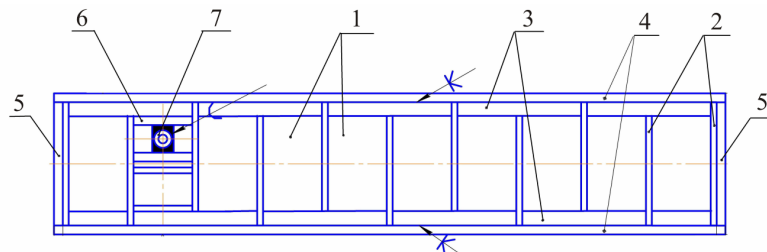


Fig. 1. Schematic of TGB-P-NT in section: 1 – thermoelement; 2 – glass fiber laminate cartridge; 3 – metal coating (subconnecting and connecting layers); 4 – ceramic heat spreaders; 5 – insulation coating; 6 – electric contact; 7 – electric wire.

Averaged values of technical characteristics of samples as compared to thermopile prototype 7.5/2.5 [2] are represented in Table 1.

Table 1
Technical characteristics of a generator thermopile

Thermopile designation	–	№ 1	№ 2	№ 3
Thermopile marking by manufacturer	Thermopile 7.5/2.5 according to [2]	TGB-P-NT-6 legs extrusion	TGB-P-NT-8 legs zone melting	TGB-P-NT-8 legs pressing
Dimensions of thermopile, mm	67 × 78.5 × 8.5	57 × 78 × 9	57 × 78 × 11	57 × 78 × 11
Number of thermocouples	83	68	68	68
Dimensions of legs, mm	5 × 5 × 6	5 × 5 × 6	5 × 5 × 8	5 × 5 × 8
Electric power, W	7.5	8.0	6.0	7.0
Optimal load voltage, V	2.5	2.0	2.05	2.3
Hot side operating temperature, °C	305	300	300	300
Cold side operating temperature, °C	100	100	100	100
Internal resistance, Ω	≤ 0.35	0.26	0.34	0.37

Temperature fields in a generator thermopile are directly related to the emergence of mechanical stresses due to the difference in thermal expansion coefficients of elements forming the thermopile rigid structure. Such thermal stresses lead to the appearance of cracks, violation of contacts and, as a consequence, destruction of thermoelectric device. These effects depend to a large extent on the properties of thermoelectric materials [1].

In a generator thermopile, a thermoelement is not a mechanically free system, being almost always related to other structural elements (base, heat-exchanger, etc). The thermoelement cannot freely change its shape with temperature variation, and this deformation constraint is the reason for origination of internal stresses, so if special measures are not taken, the value of these stresses can exceed permissible values and lead to thermoelement destruction. The less is thermoelement height, the stronger the leg semiconductor is bent (the radius of curvature is smaller) [3], the larger are the

arising mechanical stresses, hence, the higher the probability of thermoelement destruction and generator thermopile failure.

Such assertions are confirmed by practical test results: [2] describes drastic increase in the internal resistance (in fact, failure) of thermopile 7.5/2.5 (leg height 6 mm) after performing 40 – 70 cyclic temperature variations on the heat spreaders of this type of a generator thermopile.

The authors also obtained rather modest results when performing cycling tests on thermopiles of the type TGB-P-NT-6 (leg height 6 mm) with the legs made by zone melting and pressing methods: the thermopiles lost more than 5 % of generated electric power at the end of no more than 100 cycles.

To perform cyclic life test, installation shown in Fig. 2 was made.



Fig. 2. Picture of installation for life test of plane-type generator thermopile.

The installation enables test to be performed on three generator thermopiles independently. Each of three thermopiles is clamped between the heater which allows creating and maintaining the hot side temperature of up to 450 °C and the cooler which allows maintaining the cold side temperature of a generator thermopile from 30 °C to 100 °C. The accuracy of temperature control on the cooler and heater is nor worse than ± 2 °C, temperature spread on the area of the cooler and heater is no more than 1 °C. The temperature is controlled by three thermocouples located at different points on the cold side and two thermocouples on the hot side. The thermocouples caulked in the heater and cooler are adjacent directly to thermopile heat spreaders. Control of heater power and electromagnetic valves of coolers is done after a program from personal computer connected to the installation. According to experimental procedure, temperature on thermopile heat spreaders was varied in conformity with a cyclogram shown in Fig. 3.

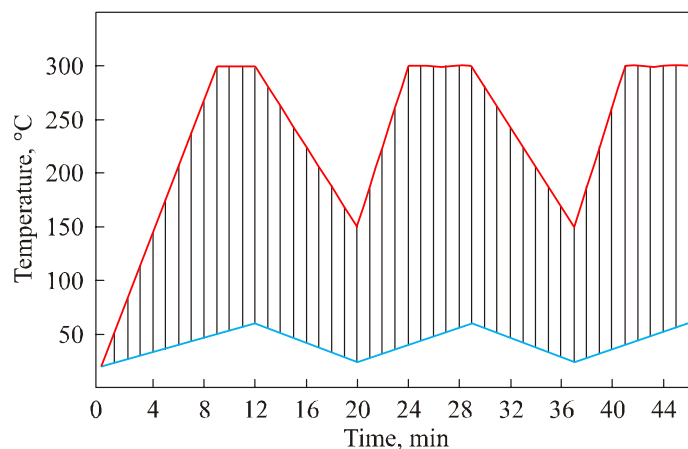


Fig. 3. Plot of temperature change on the thermopile heat spreaders when performing the tests: red colour shows temperature variation on the hot side, and blue colour – on the cold side.

When fixing a generator thermopile between the heater and cooler, the thermopile electric wires are connected to installation “Load unit”. On switching test performance program, the generator thermopile hot side is heated to a temperature of $T_h = 300 \pm 2$ °C. When this temperature is reached, it is maintained until the cold side temperature rise and equalization to $T_c = 60 \pm 2$ °C. Upon reaching said temperatures, the “Load unit”, in conformity with a program, measures current-voltage characteristic of the generator thermopile at $\Delta T = 240$ °C. The resulting current-voltage characteristic data with a serial number of cycle performed are written into a file.

On completion of current-voltage characteristic measurement, the heater is switched off and cooling half-cycle is carried out to the hot side temperature 150 ± 2 °C. In so doing, the cold side temperature drops to 25...30 °C. In the course of heating and cooling processes, there is current flow through the thermopile. For this period the “Load unit” sets the resistance corresponding to optimal load value at given ΔT . When setting test parameters, the optimal load value is set by the operator. The range of current-voltage characteristic measurement and the number of points in it is also assigned by the program. The entire temperature cycle of heating and cooling does not exceed 17 minutes for thermopile of the type TGB-P-NT-6. Fig. 4 shows a typical volt-ampere characteristic obtained on the generator thermopile life test installation upon reaching the assigned ΔT .

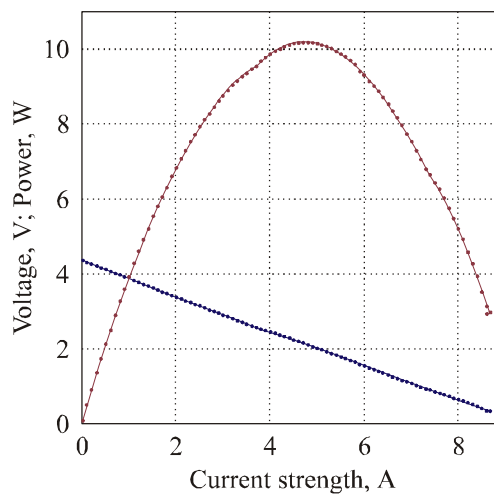


Fig. 4. Current-voltage characteristic of thermopile № 2 obtained on life test installation: $T_h = 300$ °C, $\Delta T = 240$ °C, red colour shows a change in power, blue – a change in voltage versus current value.

Results and discussion

By the results of preliminary test of TGB-P-NT-6 made with the legs produced by zone melting and pressing, it was decided to use these materials for making thermopiles of the type TGB-P-NT-8 with the leg height 8 mm. Potentially, thermopiles with higher legs are more reliable [3]. From the beginning, stable characteristics in the course of long duration test (over 600 cycles) were exhibited by thermopile №1 with extruded legs.

Fig. 5 shows a plot of power versus the number of thermocycles for generator thermopile samples under study.

Each point on the plot in Fig. 6 corresponds to EMF value (maximum value of voltage in the absence of current see in Fig. 4) measured at cyclogram point, when the hot side temperature $T_h = 300$ °C, $\Delta T = 240$ °C.

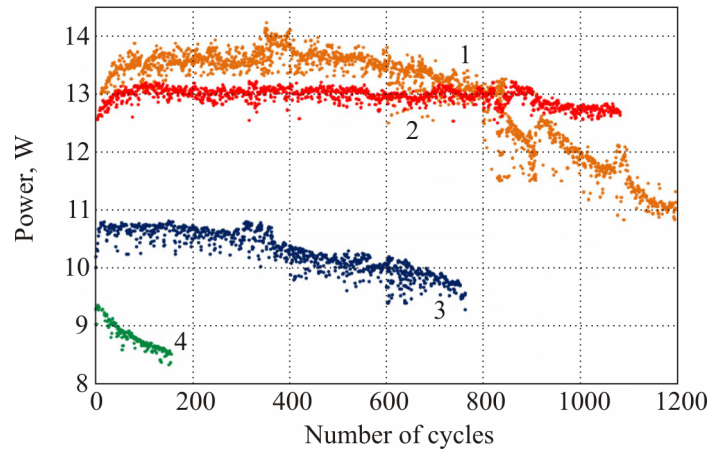


Fig. 5. Plot of change in maximum power at $T_h = 300 \text{ } ^\circ\text{C}$, $\Delta T = 240 \text{ } ^\circ\text{C}$ generated by TGB-P-NT samples in the course of test for temperature cycling on heat spreaders. Thermopile: 1 – № 1 extrusion; 2 – № 1-M extrusion; 3 – № 2 zone melting; 4 – № 3 pressing.

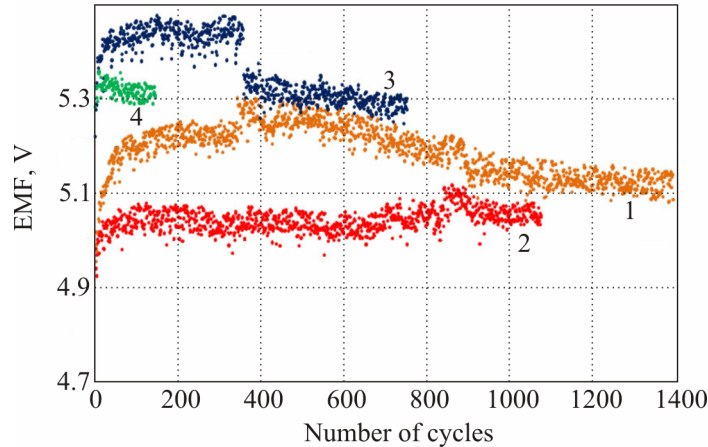


Fig. 6. Plot of change in the EMF of generator thermopile samples at $T_h = 300 \text{ } ^\circ\text{C}$, $\Delta T = 240 \text{ } ^\circ\text{C}$ in the course of test for temperature cycling on heat spreaders. Thermopile: 1 – № 1 extrusion; 2 – № 1-M extrusion; 3 – № 2 zone melting; 4 – № 3 pressing.

It is known [1, 4, 5] that the electric power of a generator thermopile:

$$W = E_{II} \cdot I = \frac{E^2 \cdot R}{(R + r)^2}, \quad (1)$$

where

$$E_{II} = (T_h - T_c) \cdot \alpha_a - I \cdot r = \Delta T \cdot \alpha_a - I \cdot r \quad (2)$$

– on-load voltage output;

$$E = (T_h - T_c) \cdot \alpha_a \quad (3)$$

– voltage between the electric wires of open generator thermopile, i.e. EMF; R – electric resistance of net load; r – internal resistance of a generator thermopile proper with the assigned

$$\Delta T = T_h - T_c; \quad (4)$$

T_h, T_c – the generator thermopile hot and cold side temperatures, respectively;

$$\alpha_a = \frac{1}{T_h - T_c} \cdot \int_{T_c}^{T_h} \alpha_{1,2}(T) dT; \quad (5)$$

where $\alpha_{1,2}(T)$ is the Seebeck coefficient function of temperature characterizing the properties of leg material [1, 4, 5].

Each point of the plot shown in Fig. 5 was obtained on condition of maximum power, i.e. when $R = r$ [1]. Thus, maximum power of a generator thermopile given to net load can reach

$$W = \frac{E^2}{4r}. \quad (6)$$

From (6) it is seen that the main characteristic which is of concern to generator thermopile end users and TEG designers, namely maximum power (Fig. 5) given to net load, is a function of EMF (Fig. 6) and the internal resistance of a generator thermopile.

Scatter of points with close values of cycle number on the plots depicted in Figs. 5 and 6 is related to the error in maintenance and reproduction of ΔT and the error proper in measuring voltage and current in the circuit.

Analyzing the plots, one can make the following conclusions: for thermopiles № 1 and № 1-M with extruded legs and № 2 during the initial stage of testing (the first 50 – 70 cycles) there is growth of maximum power due to growth of EMF of thermopiles, which in turn from (3) can be due to growth of “real” temperature difference ΔT on the junctions of thermoelectric elements, i.e. due to a decrease in thermal resistance on the generator thermopile heat spreaders. Besides, EMF increase during this stage can be related to growth of the Seebeck coefficient α of legs material due to cycling-caused temperature annealing of semiconductor material as part of operating thermopile.

Temperature variation along thermoelement leg creates thermal stresses in material. Thermal stresses are also caused by nonuniform temperature fields at points of heat supply and removal that can bring about large losses of heat flow which in the general case must pass in heat pipeline, through electrical insulation, connecting buses between thermoelectric element legs and numerous junctions and contacts between them. Temperature gradient losses in this case can reach considerable values and have a pronounced effect on the efficiency of thermoelectric element [1].

For thermopile № 3 there was no considerable growth of maximum power in cycling. On the contrary, as in the case of TGB-P-NT-6 with the legs of this material and zone melted legs, there was a smooth reduction of maximum power without considerable change in EMF. Power drop is related to considerable growth of thermopile internal resistance: prior to testing the internal resistance of thermopile, measured at room temperature was 0.37Ω , and after performing 160 temperature cycles – 0.45Ω .

Characteristics of thermopile № 2 were relatively stable up to 366 thermal cycle, following which EMF was drastically reduced by 0.1 V. Analysis of generator thermopile after removal from testing showed cracking and lamination of ceramic heat spreader in one of the angles on the hot side of the thermopile. In this angle, heat flow through thermoelements was violated with local overheat of connections on the hot side. The situation was worsened by local overheat of this area due to increased Joule heat release. All this accelerated the process of generator thermopile destruction (internal resistance growth) in the course of subsequent thermal cycles. Prior to testing, the internal resistance of thermopile measured at room temperature was 0.361Ω , and after performing 765 temperature cycles – 0.407Ω .

Temperature difference on the generator thermopile heat spreaders leads to origination of static and dynamic mechanical stresses on its structural members. In so doing, cyclic thermal, hence mechanical

effects on module structural members, namely compression, expansion and bending, can result in mechanical stresses exceeding the ultimate strength of materials forming part of a generator thermopile. Fatigue of materials during cyclic mechanical effects is the reason for thermopiles destruction [6].

Evident destruction of thermopile № 1 with the legs of extruded material began after 830 thermal cycles. Maximum power started falling relatively drastically, though EMF was reduced rather slowly. From (6) it follows that power drop is due to internal resistance increase. Prior to testing, the internal resistance of thermopile measured at room temperature was 0.26Ω . After performing 830 temperature cycles – 0.31Ω . By the end of generator thermopile testing (after 1620 cycles) the internal resistance of thermopile was 0.47Ω and it continued generating 10.4 W of maximum power. Thermopile № 1 was removed from testing, and from its legs arranged along the perimeter a thermoelement was withdrawn for thorough analysis of changes that occurred. This thermoelement was used to make a lateral microsection. The resistance of this sample prior to and after mechanical exposure did not change.

The lateral microsection of thermoelement was investigated with the use of optical microscope OLYMPUS GX51 with 1000 x magnification. Scanning electron microscope (SEM) Quanta 200 3D was used to study sample morphology (see Fig. 7) in secondary electrons mode (SE) and back-scattered electrons mode (BSE). Elemental analysis carried out by X-ray spectral microanalysis with the use of energy-dispersive spectrometer EDAX has shown that defects 4 and 5 in Fig. 7 are gas-filled cavities.

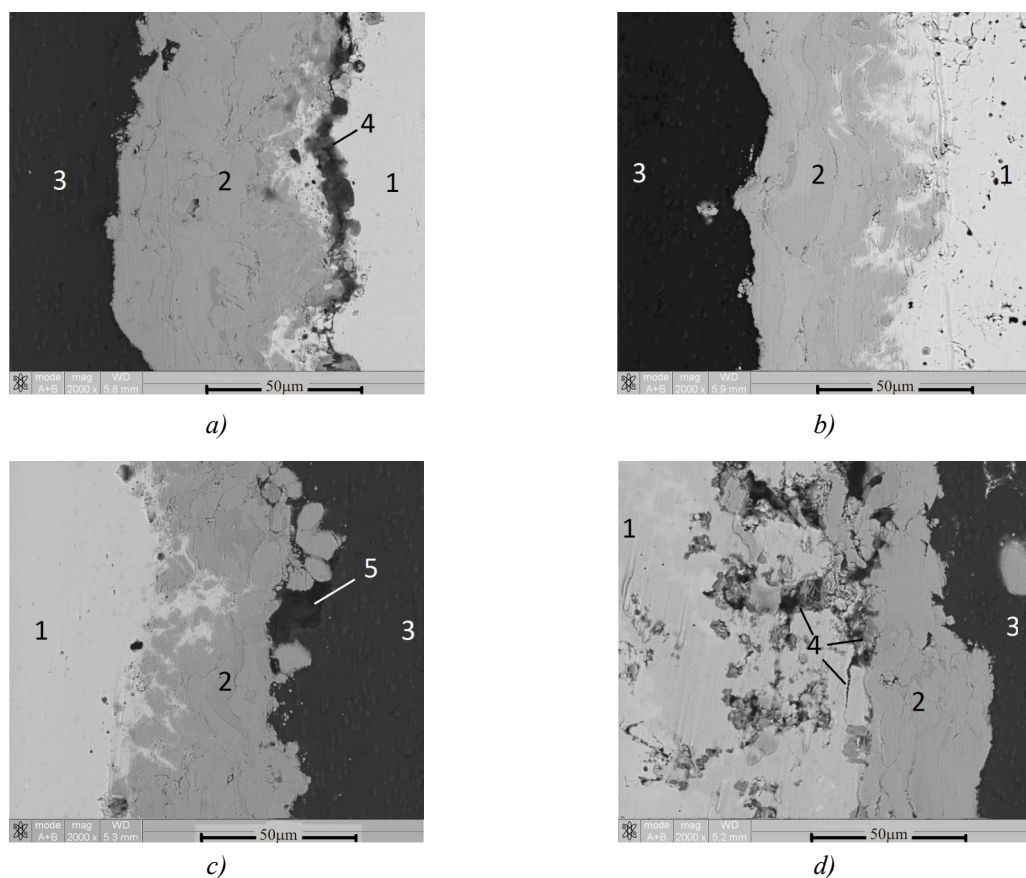


Fig. 7. SEM-image of transient layers of near-contact region of legs on the cold (a and b) and hot (c and d) side of thermoelement sample: n-type leg (a and b) and p-type leg (c and d): 1 – semiconductor leg of bismuth telluride (extrusion), 2 – barrier layer of subconnection, 3 – connection layer of aluminium alloy, 4 – destructions (cracks, laminations, etc), 5 – pores in connection layer of aluminium alloy created at spraying.

The obtained results of generator thermopile testing allowed amending the technique of arc-plasma spraying of barrier and connection layers of thermopile thermoelements. According to amended technology, a sample of thermopile № 1-M with extruded legs was made. The sample was tested for temperature cycling on heat spreaders by the same procedure. Test results are also shown in Figs. 5 and 6. Prior to testing, the thermopile internal resistance measured at room temperature was 0.26Ω , and after performing 1085 temperature cycles – 0.275Ω .

Based on the results of [6], it can be supposed that, while under temperature difference, the thermopile acquires the shape of elliptical paraboloid, which leads to growth of mechanical shear stresses in thermoelement junctions with increase in element coordinate with respect to the geometric centre of thermopile. Displacement of elements at the corners of module is the greatest [6]. Dependence of deformation value of thermopile surfaces is a linear function of temperature difference.

Earlier, in [7], the authors carried out a series of mechanical tests of semiconductor bismuth telluride legs prepared by different methods. Maximum values of breaking load under shear load were obtained exactly on the legs produced by extrusion and zone melting (thermopiles № 1 and № 2). As long as destruction caused by mechanical stresses occurs mainly in semiconductor material in the immediate vicinity of connecting layers and in semiconductor-barrier layer junction, the resistance of leg material to shear mechanical loads is not the least of the factors. Of crucial importance is also the presence and depth of damaged layers on the surface of leg connecting planes [7-11].

Conclusions

1. It is established that generator thermopiles with semiconductor legs of low-temperature material bismuth telluride, connected by arc plasma spraying technique, are resistant to temperature cycling on heat spreaders and are capable of withstanding over 1000 temperature cycles from 300°C to 150°C on the hot side and from 60°C to 20°C on the cold side of thermopile with heating and cooling cycle duration not more than 17 minutes. In so doing, the basic technical characteristics of thermopile, namely electric power, internal resistance and EMF are not reduced more than by 5 %.
2. Thermopiles made by arc plasma connection technique, with higher legs, are potentially more resistant to temperature cycling on heat spreaders than thermopiles with the same legs, but of lower height.
3. Under the conditions of temperature difference, mechanical shear stresses are originated in the thermopile, leading to destructions mainly in semiconductor material in the immediate vicinity of connecting layers and in semiconductor-barrier layer junction. Destructions appear both on the cold side and the hot side. Maximum destructions are originated in thermoelements located in a series of legs along the perimeter of thermopile, with maximum mechanical stresses created in the corners of the thermopile.

The work was performed under the financial support of Foundation for Promotion of the Development of Small Forms of Enterprises in Science and Technology, Government contract №8095p / 12669 of 18.06.2010, the financial support of Ministry of Education and Science of Russian Federation, with the use of instrument base of Centre for Collective Use of Scientific Equipment “Diagnostics of structure and properties of nanomaterials” at Belgorod State National Research University.

References

1. A.S. Okhotin, *Thermoelectric Generators*, Ed. by A.P. Regel (Moscow: Atomizdat, 1971), 288 p.
2. A.A. Pustovalov, V.V. Gusev, L.P. Nebera et al., ATEG Based Power Sources for Autonomous

- Automated Systems and Technical Facilities Controlling the State of Gas Mains and the Work of Gas Wells, *J. Thermoelectricity* 4, 65 – 71 (1998).
3. E.G. Pokorny, A.G. Scherbina, *Calculation of Semiconductor Cooling Devices* (Leningrad, Nauka Publishers Leningrad Division., 1969), 206 p.
 4. A.I. Burstein, *The Physics of Calculation of Semiconductor Thermoelectric Devices* (Moscow: State Publishing House of Physics and Mathematics Literature, 1962), 135 p.
 5. O.V. Marchenko, A.P. Kashin, V.I. Lozbin, and M.Z. Maksimov, *Methods for Calculation of Thermoelectric Generators* (Novosibirsk: Nauka. RAS Siberian Publishing Company, 1995), 222 p.
 6. A.V. Solovyova, S.V. Bobzhenko, and P.S. Krokhin, Thermoelectric Module Strains Under Electric Current Flow, *J. Thermoelectricity* 1, 71 – 74 (2009).
 7. A.V. Simkin, A.V. Biryukov, N.I. Repnikov et al., Reliability Enhancement of Generator Thermopiles Assembled Through Use of Interconnects by Arc Plasma Spraying Method, *Proceedings of XIII Interstate Workshop “Thermoelectrics and their Application”* (Saint-Petersburg, 2012), 540 p.
 8. A.V. Biryukov, N.I. Repnikov, O.N. Ivanov, et al., Advantages of Using the Electric Erosion Cutting and Flame Spraying at Connection of Thermoelements Based on Extruded Bismuth Telluride, *J. Thermoelectricity* 3, 36 – 42 (2011).
 9. A.V. Simkin, A.V. Biryukov, N.I. Repnikov et al., Effect of Contact Surface Condition on the Adhesion Strength of Interconnect Layers of Thermoelements Based on Extruded Bismuth Telluride, *J. Thermoelectricity* 2, 13 – 19 (2012).
 10. V.B. Osvensky, V.V. Karatayev, N.V. Mal'kova et al., Diffractometric Study of Structural Mechanisms of Adhesion Failure of Anti-Diffusion Nickel Coating on Bi-Te-Se Thermoelectric Materials, *J. Surface Investigation. X-ray, Synchrotron and Neutron Techniques* 3, 95 – 98 (2001).
 11. V.B. Osvensky, V.V. Karatayev, N.V. Mal'kova et al., Study of Structural Mechanisms of Adhesion Failure of Anti-Diffusion Nickel Coating on Bi-Sb-Te Thermoelectric Materials, *Materials of Electronic Technics*, 70-73 (2002).

Submitted 11.04.2013.

NEWS

XV INTERNATIONAL FORUM ON THERMOELECTRICITY

XV International Forum on Thermoelectricity dedicated to outstanding scientist Thomas Johann Seebeck was held in his home city Tallinn (Estonia) on May 21 – 24, 2013. The Forum was organized by the International Thermoelectric Academy (ITA), Thomas Johann Seebeck Department of Electronics of Tallinn University of Technology and Institute of Thermoelectricity NAS and MES of Ukraine.



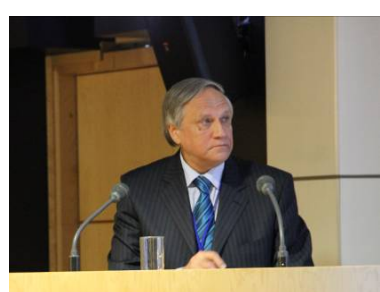
XV International Forum on Thermoelectricity

The Forum International Organizing Committee was formed by: chairman – L. Anatychuk (Ukraine), members– S. Ašmontas (Lithuania), H.J. Goldsmid (Australia), Yu. Gurevich (Mexico), T. Kajikawa (Japan), S. Sidorenko (Ukraine), T. Caillat (USA), J. Stockholm (France), T. Tritt (USA), M. Fedorov (Russia) and L. Chen (China). Chairman of local organizing committee was M. Min (Estonia).

The Forum was attended by key specialists from 22 countries of the world.

There were 92 presentations at the Forum, among them – 4 reports on the history of thermoelectricity, 8 invited lectures of leading scientists on the achievements in thermoelectricity in various countries of the world, 35 oral and 45 poster papers.

The Forum was opened by L. Anatychuk, President of



E. Velmre (Estonia)

the International Thermoelectric Academy, academician of the National Academy of Sciences of Ukraine.



ITA President Dr. L. Anatychuk (Ukraine)

The Forum participants held a moment of silence to honour the memory of ITA members who passed away in 2011-2013.

Particular attention was focused on Thomas Johann Seebeck. A report “Thomas Johann Seebeck – man and scientist” was delivered by Dr. E. Velmre (Estonia), professor of T.J. Seebeck Department of Electronics of Tallinn University of Technology.



L. Vikhor (Ukraine)

ITA President Dr. Anatychuk (Ukraine) presented a film about the role of T.J. Seebeck in thermoelectricity.

In her report, ITA corresponding member Dr. L. Vikhor (ITE, Ukraine) dwelt on the history of discovery of the bulk Seebeck effect.

Invited report on recent research and developments in the field of thermoelectric power generation technologies in Japan was presented by ITA academician, Dr. T. Kajikawa (Shonan Institute of Technology, Japan). In his report, he emphasized that fundamentals of research and development in

technology of thermoelectric power generation in Japan have changed considerably after the accident at the Fukushima nuclear power station in March 2011. Dr. Kajikawa also noted that thermoelectric generators based on waste heat recovery that have proved their high efficiency and long service life due to the use of improved *Bi-Te* modules change over to commercial exploitation stage in Japan.

Dr. L. Chen (Shanghai Institute of Ceramics, China) reported on the progress of thermoelectricity in China during the recent two years.



T. Kajikawa (Japan)



L. Chen (China)

ITA academician Dr. L. Bulat (National Research University ITMO, Russia) made a report on the development of thermoelectricity in Russia in 2010 – 2012. He told about the results of basic and applied research performed at the universities, institutes and enterprises of Russian Federation.



L. Bulat (Russia)



V. Jovovich (USA)

A report on thermoelectricity applications in vehicles, their comfort and fuel efficiency was delivered by Dr. V. Jovovich from a group of authors of Gentherm company USA). He emphasized that thermoelectric devices developed by Gentherm company are successfully employed in automobiles assuring additional comfort for passengers.

ITA corresponding member Y. Shinohara (National Institute of Material Science, Japan) presented his report on the development of thermoelectricity in South-East Asia.

The work of the Forum was accompanied by interesting discussions that continued during informal socializing of the participants.



Yu. Gurevich (Mexico)



V. Grabov (Russia)



S. Ašmontas (Lithuania)



J. Gradauskas (Lithuania)

Invited scientific reports on physics of thermoelectricity were delivered by: ITA academician Dr. Yu. Gurevich (Mexico) "The role of nonequilibrium current carriers in thermoelectric cooling", ITA academician Dr. L. Vikhor (Ukraine) "Optimal functions in thermoelectricity", ITA academician Dr. J. Snyder (USA) "Thomson cooler obtained with application of compatibility factor to the analysis of thermoelectric devices", ITA academician Dr. V. Grabov (Russia) "Thermoelectrokinetic effects as a promising direction in thermoelectricity", ITA academician Dr. S. Ašmontas (Lithuania) "Thermoelectricity of hot carriers", Dr. J. Tobola (Poland) "Study of electron transport properties from basic calculations to search for efficient thermoelectrics", ITA corresponding member Dr. J. Gradauskas (Lithuania) "Thermoelectricity of hot carriers caused by infrared laser radiation in semiconductor structures".



Y. Shinohara (Japan)



J. Snyder (USA)



J. Tobola (Poland)



A. Casian (Moldova)



J.-C. Tedenac (France)



E. Rogacheva (Ukraine)



W. Xie (China)



O. Uryupin (Russia)

Reports on thermoelectric material science were presented by: ITA academician Dr. A. Casian (Moldova “Organic thermoelectric materials: new opportunities”, ITA academician Dr. M. Fedorov (Russia) “Modern thermoelectric materials,” ITA corresponding member Dr. J.-C. Tedenac (France), Dr. A. Cantarero (Spain) “Thermal conductivity of silicon nanowires”, ITA corresponding member Dr. E. Rogacheva (Ukraine) “Concentration anomalies of thermoelectric properties in solid solutions”, Dr. Y. Nishino (Japan) “Development of thermoelectric Heusler compounds for use in energy accumulation field”, Dr. W. Xie (China) “On the achievements in the Laboratory of Advanced Technology for Materials Synthesis and Processing (Wuhan University of Technology), Dr. Yu. Grin (Germany) “What do chemists think about thermoelectricity. Thermoelectric investigations at Max Planck Institute for Chemical Physics of Solids”, Dr. O. Uryupin (Russia) “Thermoelectric properties of nanowires in asbestos channels and porous glasses”, ITA corresponding member Dr. V. Schennikov (Russia) “Effect of physical and geometric factors on the properties of thermoelectric materials”, Dr. F. Gaskoin (France) “Thermoelectric properties of intermetallic hollandite”, Dr. A. Udal (Estonia) “Can SiC and phonon drag effect change thermoEMF paradigm at low temperatures?”.



M. Fedorov (Russia)



A. Cantarero (Spain)



Y. Nishino (Japan)



Yu. Grin (Germany)



F. Gascoin (France)



S. Yatsyshin (Ukraine)



G. Arakelov (Russia)



G. Min (United Kingdom)



J. Takai (Japan)

Thermoelectric applications were covered in the reports presented by: Dr. S. Yatsyshin (Ukraine) "Thermoelectric temperature sensors under extreme operation conditions", ITA academician Dr. S. Filin (Poland) "Application of thermoelectricity in domestic appliances: yesterday, today, tomorrow", ITA corresponding member Dr. G. Arakelov "Photoelectric sensors with thermoelectric cooling. State of the art, problems and prospects", ITA corresponding member Dr. A. Terekov (Russia) "Industrial-purpose thermoelectric generators on renewable fuel", Dr. G. Min (United Kingdom) "Theory of thermoelectric devices for operation at given thermal power", Dr. K. Wojciechowski (Poland) "Characterization of high-performance segmented $Bi_2Te_3/CoSb_3$ thermocouples for vehicular applications", Dr. A. Nazarenko "Reliability enhancement of thermoelectric coolers using polymer vacuum coatings", A. Ivanov (Russia) "On the activity of "RIF" company", J. Takai (Japan) "Presentation of Z-max company". In his report "Global projects in thermoelectricity and the ways of their implementation", ITA President Dr. L. Anatychuk (Ukraine) dwelt on some new lines of thermoelectricity applications based on the use of the Seebeck effect.



V. Schennikov (Russia)



A. Udal (Estonia)



S. Filin (Poland)



A. Terekov (Russia)



K. Wojciechowski (Poland)



ITA President Dr. L. Anatychuk



*Awarding the ITA Golden Prize
to Yu. Gurevich*

Dr. Oleg Uryupin, A. F. Ioffe Physical-Technical Institute, Russia; Dr. Vladimir Jovovich, Gentherm company, USA.

ITA Golden Prize in the nomination "For the fundamental contribution to development of thermoelectricity" was awarded to ITA academician Dr. Gurevich; in the nomination "For technology and quality of thermoelectric products" – to Open JSC "Corporation NPO "RIF" and "ERA-SFTI" LTD.

However, the main event during the Forum was unveiling a monument to Seebeck.

On May 24, 2013 during the operational period of the Forum the General Meeting of the International Thermoelectric Academy took place where as a result of competitive selection, by secret voting, the following ITA academicians were elected: Dr. Mikhail Fedorov, A.F. Ioffe Physical-Technical Institute, Russia; Dr. Yoshi Nishino, Nagoya Institute of Technology, Japan; Dr. Xinfeng Tang, China. ITA corresponding members were elected: Dr. Yuri Grin, Max Planck Institute, Germany; Dr. Krzysztof Wojciechowski, AGH University of Science and Technology, Poland; Dr. Svyatolsav Yatsyshin, National University "Lvivska Politehnika", Ukraine;



*Awarding the ITA Golden Prize to A. Ivanov,
Director of Open JSC "Corporation
NPO "RIF".*



Monument to T.J. Seebeck



Unveiling the monument to T.J. Seebeck



Outside view of the monument to T.J. Seebeck



Working model of Seebeck's experiment

The monument has been created with the support of 42 members of the International Thermoelectric Academy from 15 countries of the world. Their names have been engraved on the monument. 16 thermoelectric companies from various countries have also become the monument sponsors.

The idea of the monument belongs to Dr. Anatychuk, the sculptress is Mrs. Kuulbusch. The monument symbolizes the short-circuited Seebeck's thermocouple. Laser technologies create a 3-D image of Seebeck.

Installed on the monument is a working model of Seebeck's experiment. The monument was unveiled in solemn atmosphere on May, 2013. In this way the grateful supporters of thermoelectricity have honoured the memory of outstanding scientist Thomas Johann Seebeck.



**THOMAS JOHANN
SEEBECK**

1770–1831



ARTICLE PREPARATION RULES

The article shall conform to the journal profile. The article content shall be legible, concise and have no repetitions.

The article shall be submitted to the editorial board in electronic version.

The text shall be typed in text editor not lower than MS Word 6.0/7.0.

Page setup: “mirror margins”- top margin – 2.5 cm, bottom margin – 2.0 cm, inside – 2.0 cm, outside– 3.0 cm, from the edge to page header – 1.27 cm, page footer – 1.27 cm.

Graphic materials, pictures shall be submitted in color or, as an exception, black and white, in .ojp or .cdr formats, .jpg or .tif formats being also permissible. According to author’s choice, the tables and partially the text can be also in color.

The article shall be submitted in English on A4 paper sheets; the number of pages shall not exceed 12. By agreement with the editorial board, the number of pages can be increased.

To accelerate publication of the article, please adhere to the following rules:

- the authors’ initials and names are arranged in the centre of the first page at the distance of 1 cm from the page header, font Times New Roman, size 12 pt, line spacing 1.2;
- the name of organization, address (street, city, postal code, country) – indent 1 cm below the authors’ initials and names, font Times New Roman, size 11 pt, line spacing 1.2, center alignment;
- the title of the article is arranged 1 cm below the name of organization, in capital letters, semi-bold, font New Roman, size 12 pt, line spacing 1.2, center alignment. The title of the article shall be concrete and possibly concise;
- the abstract is arranged 1 cm below the title of the article, font Times New Roman, size 10 pt, in italics, line spacing 1.2 ,center alignment;
- key words are arranged below the abstract, font Times New Roman, size 10 pt, line spacing 1.2, justified alignment. The title “Key words” – font Times New Roman, size 10 pt, semi-bold;
- the main text of the article is arranged 1 cm below the abstract, indent 1 cm, font Times New Roman. size 11 pt, line spacing 1.2, justified alignment;
- formulae are typed in formula editor, fonts Symbol, Times New Roman. Font size is “normal” – 12 pt, “large index” – 7 pt, “small index” – 5 pt, “large symbol” – 18 pt, “small symbol” – 12 pt. The formula is arranged in the text, centre aligned and shall not occupy more than 5/6 of the line width, formulae are numbered in round brackets right;
- dimensions of all quantities used in the article are represented in the International System of Units (SI) with the explication of the symbols employed;
- figures are arranged in the text. The figures and pictures shall be clear and contrast; the plot axes – parallel to sheet edges, thus eliminating possible displacement of angles in scaling;
- tables are arranged in the text. The width of the table shall be 1 cm less than the line width. Above the table its ordinary number is indicated, right alignment. Continuous table numbering throughout the text. The title of the table is arranged below its number, center alignment;
- references should appear at the end of the manuscript. References within the text should be enclosed in square brackets. References should be numbered in order of first appearance in the text. Examples of various reference types are given below.

- L.I. Anatychuk, *Thermoelements and Thermoelectric Devices: Handbook* (Kyiv: Naukova Dumka, 1979), p.766. (Book)
- T.M. Tritt, Thermoelectric Phenomena, Materials, and Applications, *Annual Review of Materials Research* **41**, 433 (2011). (Journal paper)
- U. Ghoshal, *Proceedings of the XXI International Conference on Thermoelectrics* (N.Y., USA, 2002), p. 540. (Proceedings Conference)

The article should be supplemented by:

- letter from the organization where the work was performed or from the authors of the work applying for the publication of the article;
- information on the author (authors): last name and initials; full name and postal address of the institution where the author works; academic degree; position; telephone number; E-mail;
- author's (authors') photo in color or, as an exception, in black and white. With the number of authors more than two their photos are not given;
- author's application to the following effect:

We, the undersigned authors, ... transfer to the founders and editors of "Journal of Thermoelectricity" the right to publish the article...in Ukrainian, Russian and English. This is to confirm that the present publication does not violate the copyright of other persons or organizations.

Date

Signatures

Below is given an example of article preparation.

A.I. Casian¹, B.M. Gorelov²

Author's
photo
 3×4 cm

¹Technical University of Moldova,
168, Stefan cel Mare Ave.,
Chisinau, MD-2004, Moldova;
²Institute of Surface Chemistry of National Academy
of Sciences of Ukraine, 17, Gen. Naumov Str.,
Kyiv, 03164, Ukraine

Author's
photo
 3×4 cm

STATE OF THE ART AND PROSPECTS OF THERMOELECTRICITY ON ORGANIC MATERIALS

The aim of the paper is to analyze the expected thermoelectric opportunities of organic materials, including some highly conducting quasi-one-dimensional crystals. It is shown that interest of investigators in these materials has been growing recently. Quasi-one-dimensional organic crystals have high prospects for thermoelectric applications. These materials combine the properties of multi-component systems with more diverse internal interactions and of quasi-one-dimensional quantum wires with increased density of electronic states. It is shown that the values of the thermoelectric figure of merit $ZT \sim 1.3 - 1.6$ at room temperature are expected in really existing organic crystals of tetrathiotetracene-iodide, TTT_2I_3 , if the crystal parameters are approaching the optimal ones.

Key words: thermoelectricity, tetrathiotetracene-iodide, polarizability.

Introduction

It is known that conducting organic materials usually have much lower thermal conductivity than the inorganic materials. Moreover, the organic materials can be fabricated by simpler chemical methods, and it is expected that such materials will be less expensive in comparison with the inorganic ones. Exactly these properties attracted attention to such materials for the use in thermoelectric (TE) applications long time ago [1, 2]. In spite of relatively high value of the thermoelectric figure of merit $ZT = 0.15$ at room temperature observed in polycopper phthalocyanine [2] as early as 1980, the thermoelectric properties of organic materials are still weakly investigated. This situation has the only explanation that thermoelectricians are still weakly interested in organic materials, and organic chemists are also weakly interested in thermoelectric materials. Moreover, in order to seek good organic thermoelectrics, it is necessary to organize multidisciplinary consortiums of physicists, organic chemists and engineers in the field of thermoelectricity.

The aim of this paper is to present briefly the state-of-the-art of investigations in the area of new organic thermoelectric materials and to describe the nearest expected results for really existing quasi-one-dimensional organic crystals of tetrathiotetracene-iodide, TTT_2I_3 .

Quasi-one-dimensional organic crystals of TTT_2I_3

The structure of quasi-one-dimensional organic crystals of tetrathiotetracene-iodide, TTT_2I_3 , has been briefly described in [34]. These needle-like crystals are formed of segregate chains or stacks of planar molecules of tetrathiotetracene TTT , and iodine ions. The chemical compound TTT_2I_3 is of mixed-valence: two molecules of TTT give one electron to the iodine chain which is formed from I_3^- ions. The

conductivity of iodine chains is negligibly small, so that only *TTT* chains are electrically conductive and holes serve as carriers. The electrical conductivity σ along *TTT* chains at room temperature varies between 10^3 and $10^4 \Omega^{-1}\text{cm}^{-1}$ for crystals grown by gas phase method [35], and between 800 and $1800 \Omega^{-1}\text{cm}^{-1}$ for crystals grown from solution [36]. Thus, the conductivity is very sensitive to crystal impurity and perfection which depends on growth method. In the direction perpendicular to chains σ is by three orders of magnitude smaller than in the longitudinal direction and is neglected.

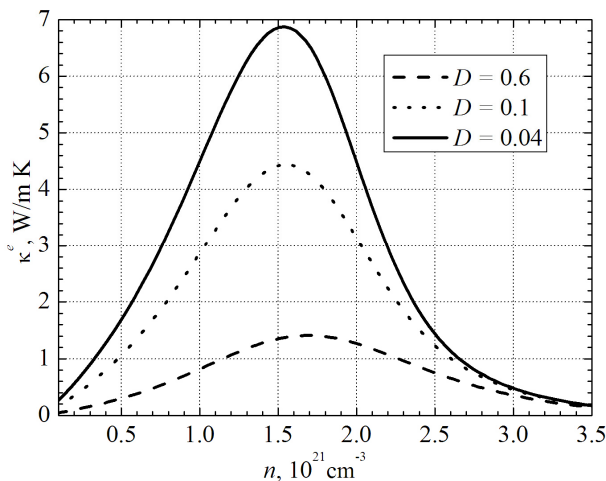


Fig. 1. Dependences of electron thermal conductivity κ^e on n .

$$\sigma = R_0, S = R_1 / eTR_0, \kappa^e = (e^2 T)^{-1} \left(R_2 - R_1^2 / R_0 \right), \quad (1)$$

Thermoelectric properties

Expressions (2) – (3) have been calculated in order to determine the thermoelectric properties of quasi-one-dimensional organic crystals of TTT_2I_3 with different degrees of purity....

Conclusions

The state-of-the-art of research on new organic materials for thermoelectric applications is analyzed. It is shown that the interest of investigators in these materials has been growing in recent years. The highest value of $ZT \sim 0.38$ at room temperature has been measured in doped acetylene, with the only problem that this material is not stable. Accurate control of the oxidation level in poly (3, 4-ethylenedioxythiophene) (PEDOT) gave the power factor $324 \mu\text{W}\cdot\text{m}^{-1}\text{K}^{-2}$ and in combination with its low intrinsic thermal conductivity ($\kappa = 0.37 \text{ W}\cdot\text{m}^{-1}\text{K}^{-1}$) yielded $ZT = 0.25$ at room temperature, and this material is air-stable....

References

- Ali Shakouri, Recent Developments in Semiconductor Thermoelectric Physics and Materials, *Annu.Rev.Mater.Res.* **41**, 399–431 (2011).
- L.I. Anatychuk, *Thermoelectricity, Vol.2, Thermoelectric Power Converters* (Kyiv, Chernivtsi: Institute of Thermoelectricity, 2003), 376p.
- M.E. Bengen, *German Patent Appl. OZ 123, 438, 1940; German Patent 869,070, 1953, Tech. Oil Mission Reel, 143,135, 1946.*